Studies on NO_X purification catalysts under excess oxygen conditions

TOSHIYUKI TANAKA

2013

- Table of Contents -

Chapter 1

General Introduction

1. Background

Since its introduction at the end of the 19th century, the automobile has become essential to daily life and has greatly contributed to the cultural and economic progress of developed countries. In addition, the use of automobiles continues to spread rapidly throughout the world, especially in developing countries. The immense popularity of the car, however, has a number of negative impacts on the global environment and ecosystems. Automobile exhaust is a major cause of air pollution which degrades various ecosystems and, since the mid-1980s, has been known to contribute to global warming. As a result, a significant amount of work has been performed in order to find solutions to these problems.

The hazards of air pollution resulting from exhaust gases have been known ever since the mechanisms which generate photochemical smog were elucidated in the United States at the beginning of the 1950s, at which point the need to control automobile exhaust was recognized. The American Clean Air Act (also called the Muskie Act) was passed in 1970, and even stricter emissions control legislation has followed. In Japan, emissions regulations regarding carbon monoxide in car exhaust were first passed in 1966, while

regulations similar to the Muskie Act were put in place in 1973 and achieved the targeted emissions levels in 1978. At the time, these regulations were said to be the most severe in the world. In Europe, the ECE15 regulations were established in 1970 and further strengthened in 1981. Since 1990, the regulations of various countries and their sub-regions have become increasingly strict, such as in California, which requires automobile manufacturers to produce a certain percentage of low emission vehicles (LEV) and zero emission vehicles (ZEV) for sale in that state. Fig. 1 summarizes the changes in NO_X regulations (defined as the total amount of NO and NO_2) between 1995 and 2020. In the developed countries of Japan, the United States and Europe, increasingly severe emission regulations have been enforced.

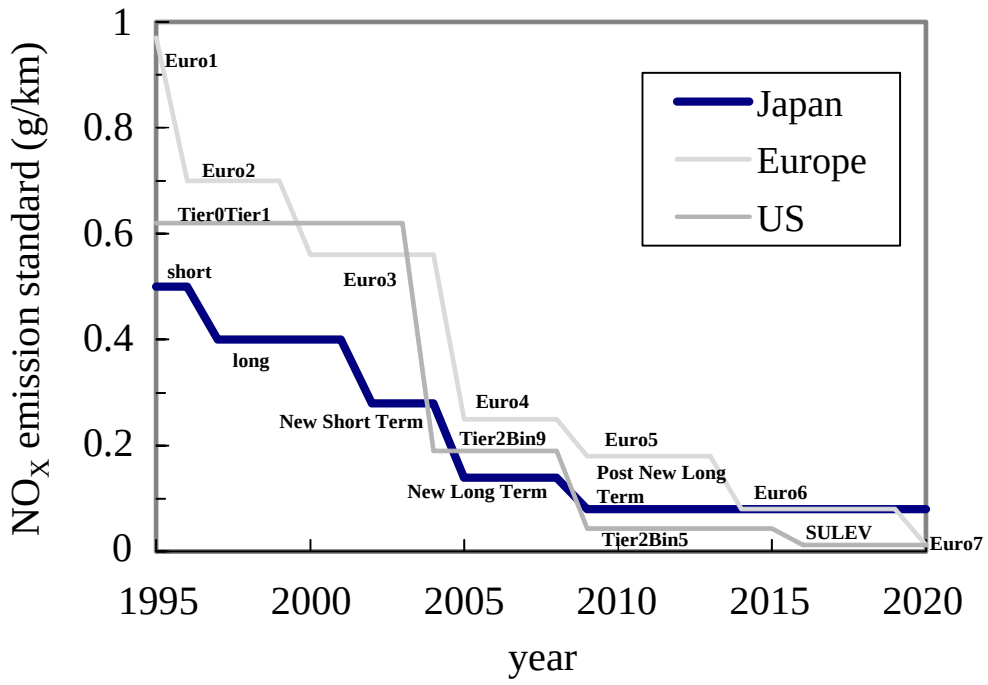

Fig. 1. Transition of NO_X regulation in Japan, US and Europe.

CO_2 emission from automobiles has contributed significantly to global warming since approximately 1980. Statistics from the Japanese Ministry of Environment show that the transportation section accounted for 19.6% of CO_2 emissions in 2011 and this value

continues to increase yearly [1]. In recent years, engines with increased fuel economy have been seen as a way to reduce CO_2 emissions from automobiles and remarkable progress has been made in the development of batteries for use in electric vehicles (EVs) and hybrid vehicles (HVs). HVs have been considered the next-generation of energy efficient vehicles ever since the Toyota Motor Corporation began selling the world's first mass production hybrid car in 1997. However, technical improvements in the combustion engine itself, such as lean combustion for improved fuel efficiency, have also developed in parallel with the promotion of such HVs.

A diesel engin**e** is an internal combustion engine that uses the heat of compression to ignite the fuel which has been injected into the combustion chamber. This is in contrast to spark-ignition engines, such as a gasoline or gas engines, which use a spark plug to ignite an air-fuel mixture. The diesel engine has the highest thermal efficiency of any regular internal or external combustion engine due to its very high compression ratio and various techniques have recently been developed to further improve its performance. These include the common rail type fuel injection system, the variable geometry (VG) turbo charger with inter-cooler, cooled exhaust gas recirculation (EGR) and high-speed, large-capacity electronic control units. Further combustion improvement may be realized by refining existing techniques such as the high pressure jet, turbo supercharges and EGR.

In the case of the direct-injection, lean-burning gasoline engine, lean combustion caused by stratified charge combustion and pumping loss reduction results in reduced fuel consumption compared to that of a stoichiometric gasoline engine incorporating a three-way catalyst (TWC). Further improvements in fuel efficiency are possible by employing an automatic continuously variable transmission (CVT) and variable valve timing (VVT) combined with an idling stop device. These fuel efficiency innovations are typically bundled with systems intended to reduce the release of toxic gases such as NO_X. Improvements in automotive fuel efficiency are still ongoing and further technological advances are continuously being researched by the leading automobile companies.

2. The problem of NO_X emission and the solution strategy

One subject of the present research is the problem of NO_X emissions, which has been an issue for a long time. It is well known that NO_X as a component of air pollution induces various health complaints, including allergies, asthma and atopic dermatitis. In addition, NO_X exposed to UV light from the sun undergo photochemical reactions to produce smog chemicals which may pose a serious health hazard to humans when present in high concentrations.

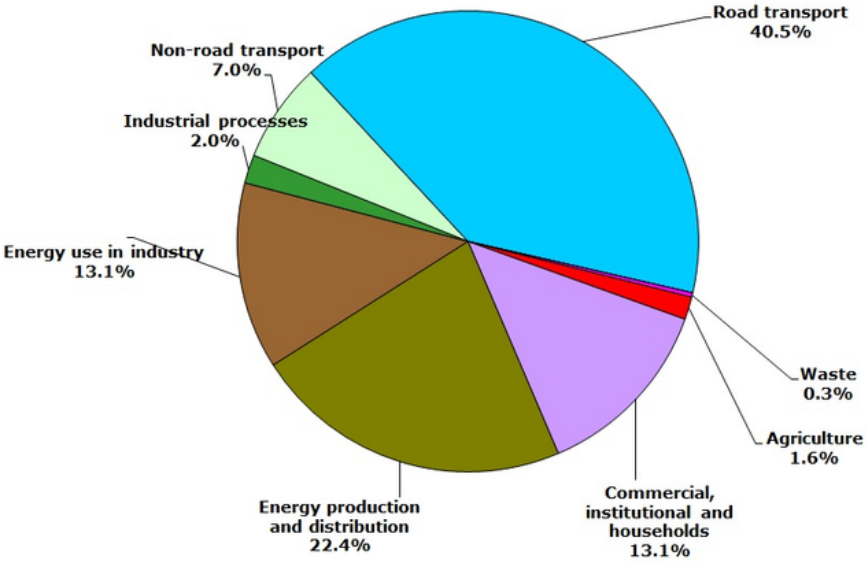

Fig. 2. Sector share of nitrogen oxides emissions (EEA member countries) in 2010.

NO_X is produced from a number of anthropogenic sources, including boilers, automobile engines, incinerators and oil stoves, although it may also be generated from natural phenomena such as thunderstorms. Among the anthropogenic emission sources, the proportion which arise from automobile exhaust account for more than 40%, as indicated in Fig. 2 [2]. It has been reported that the emission from diesel fuel engines accounts for the majority of automotive emission [3] and, in general, the NO_X emissions from

lean-burning exhaust is less than that from stoichiometric gasoline engines. It indicates that the removal of NO_X from lean-burning exhaust has not been improved during this period. Recently, a number of techniques have been adopted for the removal of NO_X from exhaust, and so NO_X emissions are gradually decreasing in the developed countries, as indicated in Fig. 3 [4]. Further decreases in automobile NO_X emissions, however, will require advanced technological innovations in both the engine control and the after-treatment of exhaust gases.

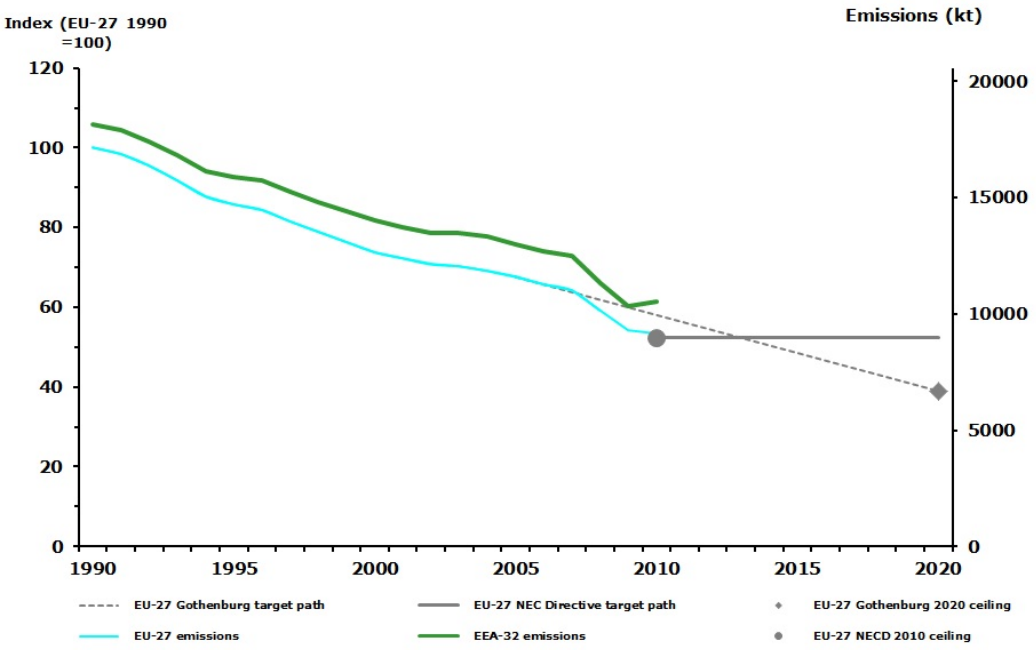

Fig. 3. Emission trends of nitrogen oxides (EEA member countries, EU-27 Member States).

One of the most innovative techniques for the control of toxic exhaust gases such as NO_X resulting from gasoline engines is the three-way catalyst (TWC). The development of TWCs played a significant role in allowing vehicles to meet the original emissions regulation in the 1970s. Fig. 4 shows the relationship between the air/fuel (A/F) ratio and the concentrations of NO_X, hydrocarbons (HC) and carbon monoxide (CO) exhausted from

a gasoline engine, in which it is seen that each component is affected independently by the A/F ratio [5]. An A/F ratio of 14.6 provides the perfect stoichiometric mixture for complete combustion. Under rich combustion conditions (A/F < 14.6), the exhaust contains elevated concentrations of HC and CO produced by partial oxidation of the fuel, while, under lean combustion conditions, NO_X emissions reach a maximum at A/F = 16 before decreasing at very lean combustion ratios. In addition, the exhaust O_2 concentration increases gradually with increases in the A/F ratio.

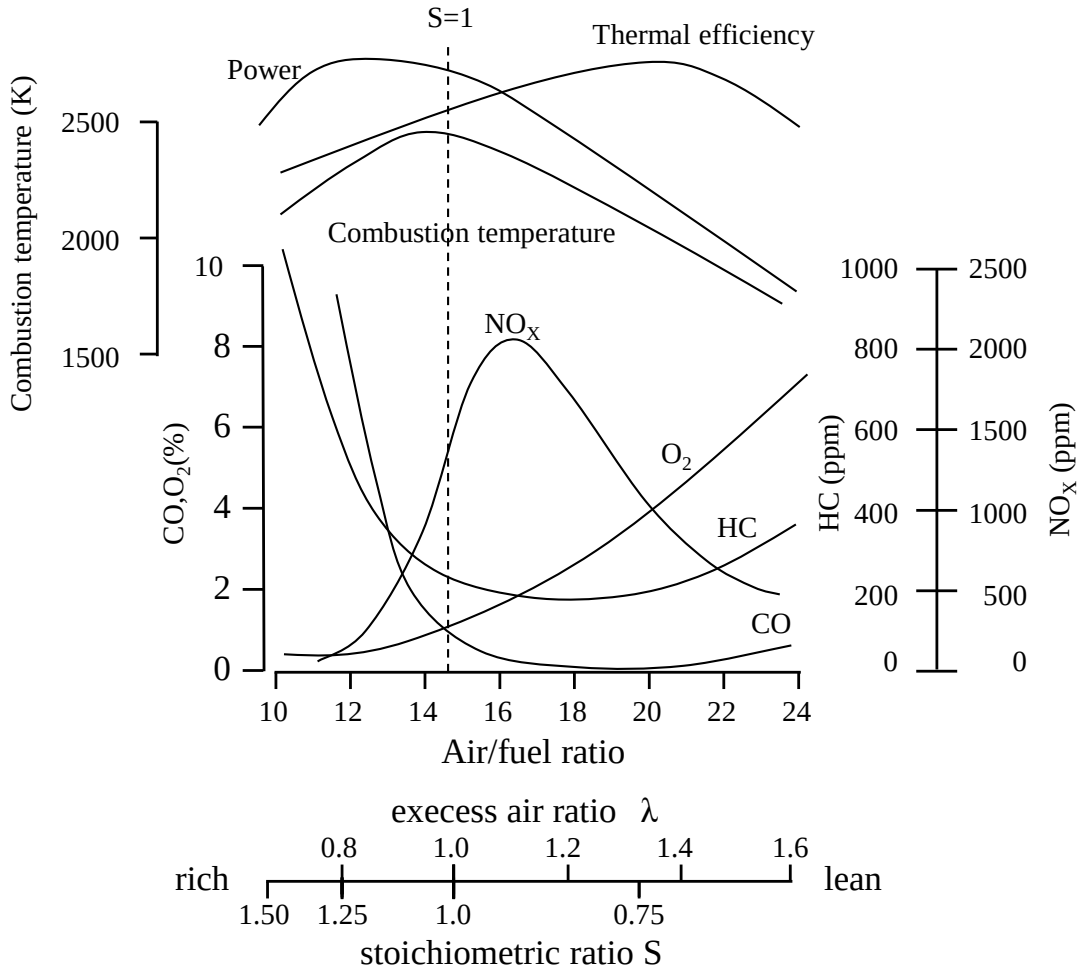

Fig. 4. The influence of air/fuel ratio on the engine performance and the exhaust gases

TWC systems purify exhaust gases using a noble metal catalyst at the stoichiometric point where HC and CO act as reducing gases and react with NO_X and O_2 as oxidizing gases. Accordingly, high catalytic activity can be obtained by controlling the A/F ratio during engine combustion as indicated in Fig. 5 [6]. To date, many researchers have attempted to improve the TWC system by modifying the catalyst as well as by using oxygen storage materials and supports with higher thermal resistance.

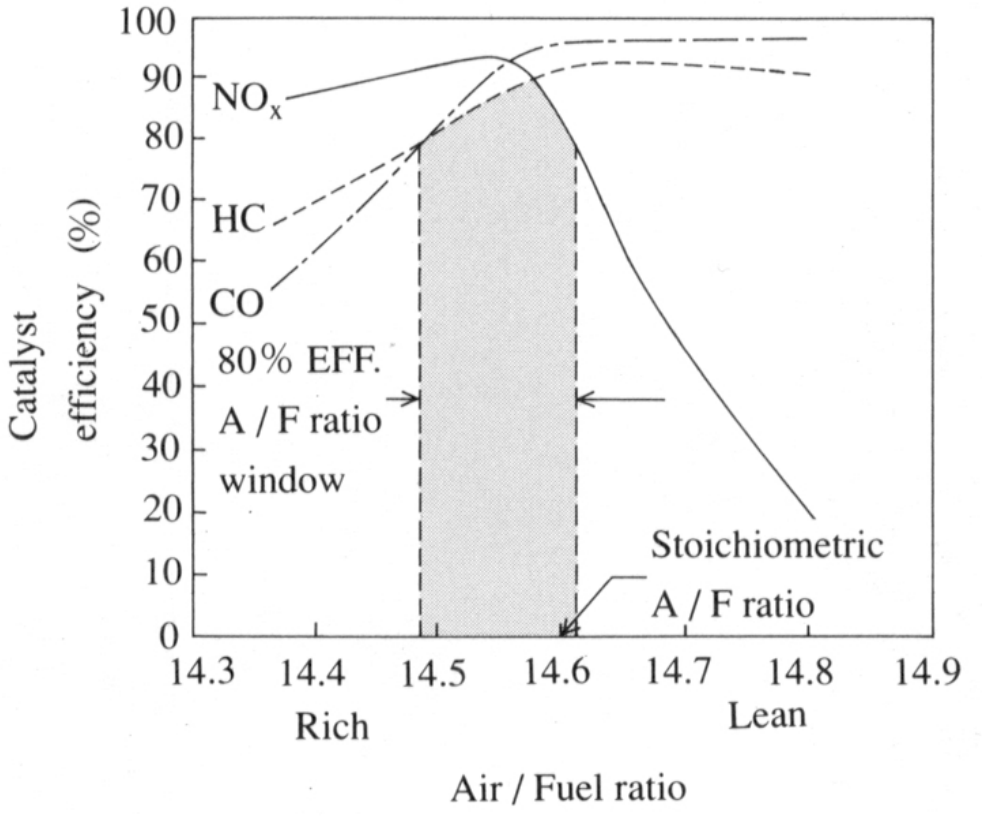

Fig. 5. The relation of three way (CO, NO_X and HC) efficiency vs. the ratio of air/fuel (A/F).

Lean-burning combustion can product an improvement in fuel efficiency and also reduce the generation of CO_2 and NO_X, but cannot readily proceed by the reactive inhibition of co-exiting O_2, even though NO_X emissions decrease in the lean region as

indicated in Fig. 4. It terms of NO_X purification, TWCs are known to exhibit non-selective catalytic reduction and hence cannot achieve high activity in the lean combustion region. Accordingly, the removal of NO_X under excess oxygen conditions is a significant problem which remains unsolved, although significant research work has resulted in numerous technical improvements with practical applications to NO_X removal.

While lean combustion engines produce less CO_2, they also emit elevated levels of NO_X under excess oxygen conditions. As described above, significant effort has been directed towards improving lean burn and diesel engine systems to reduce NO_X emissions. However, to achieve further reductions, advanced catalytic technologies need to be adopted and therefore various catalyst systems, as discussed in this paper, are currently undergoing research and development to allow their practical application.

NO_X selective catalytic reduction (SCR) materials have been the subject of many studies, ever since the discovery of NO direct decomposition over Cu-ZSM-5 by Iwamoto *et al*. [7]. Since the early 1990s, various materials have been researched as components of SCR systems using HC [8-11] as a reducing gas. These are composed of various metals, including the noble metals, in conjunction with support oxides such as alumina or zeolites. The results of studies using H_2 [12, 13], CO [12, 13] and NH_3 [14, 15] as reducing gases are provided in Fig. 6 [12, 13].

In this type of system, the reducing gas used to remove NO_X is supplied from gases normally present in the engine exhaust. SCR catalysts coupled with reducing agent dosing systems such as fuel injection and urea addition have also been developed to allow for variable NO_X emissions. Although SCR systems using co-existing HC gases have an advantage in terms of space utilization, there are some problems associated with this approach, including the low temperature activity of base metal catalysts such as Cu and by-production of nitrous oxide (N_2O) when using noble metal catalysts such as Pt. These problems tend to make SCR systems without dosing of the reducing agent inferior to SCR with a dosing system or NO_X storage reduction (NSR) systems (described below) and

therefore further improvements are required before such systems have practical applications.

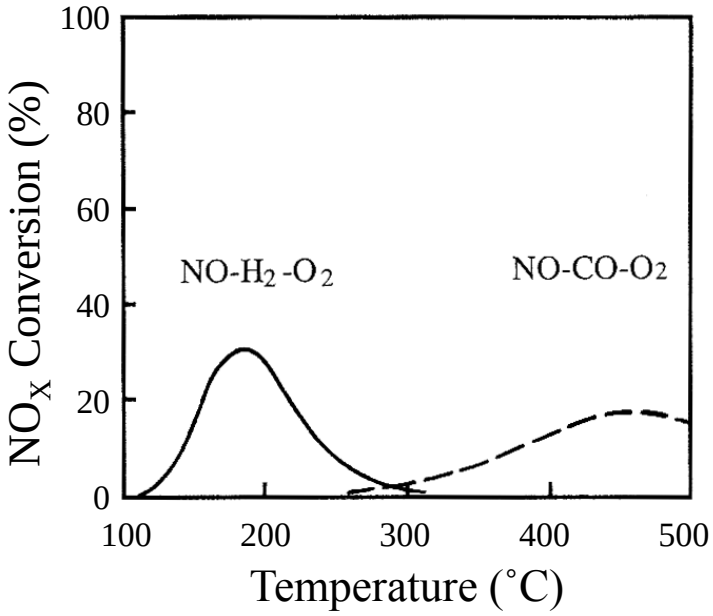

Fig. 6. NO_X conversion efficiency as a function of temperature of $NO-H_2-O_2$ and $NO-CO-O_2$ systems for $Pt-Mo-Na/SiO_2$ catalyst. SV=200000h^{-1}.

Currently, the primary technology associated with SCR is the urea-dosing SCR process applied primarily to large vehicles. In this system, ammonia produced by the decomposition of urea is added in front of a catalyst such as Cu-zeolite and used as a reducing agent for NO_X. This method is based on the ammonia SCR system commonly used as a denitrification device in boilers within thermal power stations and first put into practical use in the 1970s. The urea SCR system is able to respond to changing NO_X emissions by controlling the dosing of urea to maintain the optimal NH_3 to NO_X ratio. Some aspects of the system which need to be improved including optimizing the space required for the onboard urea tank and urea dosing unit, refilling of the urea tank by users, improving activity at low temperatures at which urea cannot be decomposed, improving

thermal durability and suppression of NH_3 passing unreacted through the catalyst. To improve the low temperature NO_X removal abilities of NH_3-based SCR systems, it is necessary to explore ways to increase the decomposition rate of urea to NH_3, to improve the catalytic activity for the oxidation of NO to NO_2 and to increase the decomposition rates of intermediates such as NH_4NO_3.

The NO_X storage and reduction (NSR) system is another practical method for NO_X removal under excess oxygen conditions. Many studies have been conducted for the purpose of improving this technology since it was put into use by Toyota in 1994 [16, 17]. In the NSR system, as indicated in Fig. 7, NO is oxidized to NO_2 over precious metals within the catalyst and all NO_2 is then chemically combined with NO_X storage materials and stored as nitrate ions. In the subsequent reduction stage, under a stoichiometric or reducing atmosphere, the stored nitrate ions are released from the storage materials as NO_X (NO or NO_2) and then reduced to nitrogen.

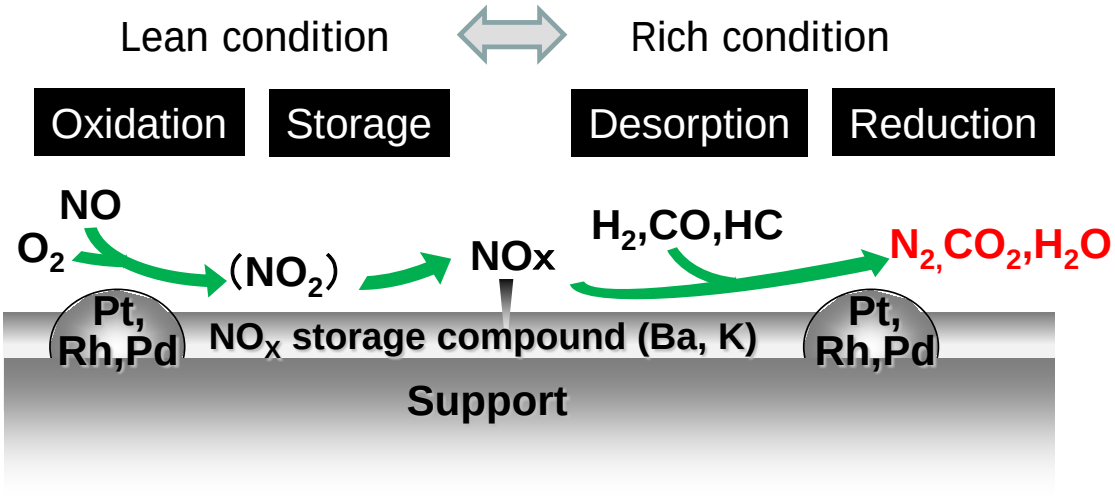

Fig. 7. The reaction mechanism of NO_X storage and reduction catalyst.

The NSR catalyst system has the advantages of high performance in removing NO_X compared with other methods. Unfortunately, NSR catalysts are deactivated by sulfur poisoning and/or thermal deterioration. Another problem to be solved is the limited active temperature ranges at both low and high temperatures, which need to be expanded. Fig. 8 indicates the performances of NSR and SCR catalysts during the ECE (Economic Commission for Europe) mode. NSR catalyst as well as SCR catalyst does not exhibit high activity in both the low temperature region (< 200 °C), and so it is extremely important to expand the active temperature region of these materials.

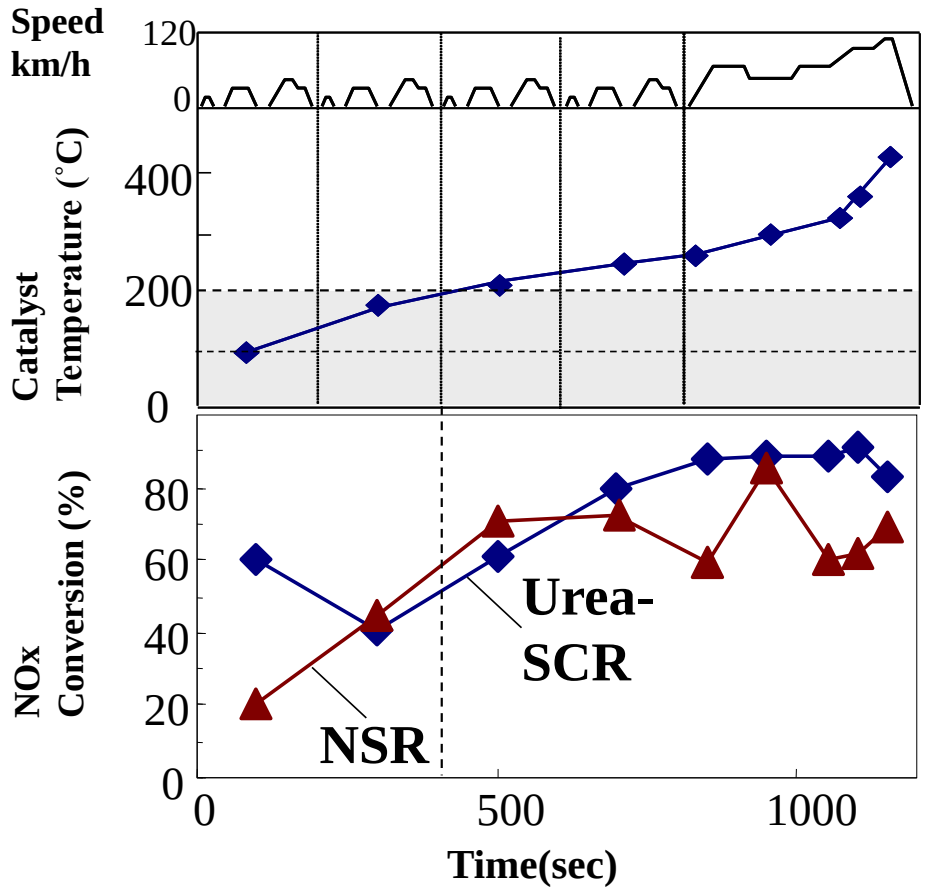

Fig. 8. Catalyst temperature and NO_X conversion during the ECE mode.

Sulfur poisoning is caused by sulfur dioxide (SO_2) that is derived from the combustion of sulfur compounds in fuel. Sulfur content of fuel that strongly affects such a sulfur deactivation is decreasing in developed countries by the recent regulations for both gasoline and diesel fuel [18]. For example, in EU countries, USA and Japan, low level sulfur content under 10 ppm has already achieved since 2009. However, sulfur content in developing countries is still higher level, which is beyond 600 ppm.

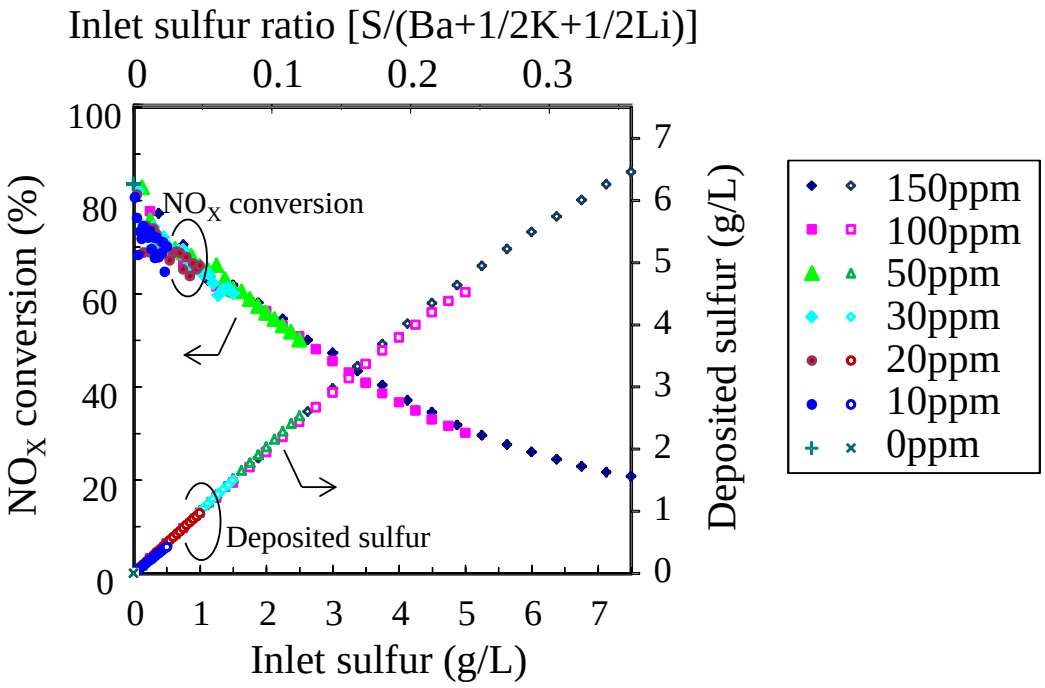

Fig. 9. NO_X conversion and deposited sulfur amount on a NSR catalyst during the sulfur adsorption procedure at 400℃ under cycling of lean (120 s) and rich (3 s) conditions.

Sulfur deactivation is known to occur by poisoning of precious metals, supports and NO_X storage materials, and strongly influences the NO_X storage ability of the system, as indicated in Fig. 9 [19]. Although NSR activity can be recovered by a regeneration

treatment for sulfur desorption [20], the regeneration procedure gives rise to thermal deactivation as well as a fuel penalty in cases where it is carried out at high temperature for long time periods. Accordingly, a method for the efficient regeneration of sulfur-poisoned catalysts is needed to improve the performance of NSR materials. In addition, since thermal deterioration is believed to be due to sintering of the precious metals which act as redox sites and the alkali compounds which serve as NO_X storage sites, the inhibition of sintering is also required to improve NSR activity.

There are two causes of the decreasing activity of these catalysts at low temperature (under 250 °C). One is that NO is not oxidized to NO_2, which is a requirement of the NO_X storage reaction, and the other is that the adsorption of NO_X is inhibited in the presence of other emission gases such as H_2O, CO_2, CO, HC and SO_X. It is important to exclude these other gases such that NO_X, and especially NO, are selectively adsorbed. Further, in the case of higher temperatures (over 500 °C), the stability of adsorbed NO_X should be improved. Several research projects have recently examined these issues.

In recent years, in addition to the catalyst improvements noted above, further performance improvements in the NO_X removal process have been associated with new catalyst systems and new system controls. Various combinations of different technologies have been reported in the literature, including a diesel particulate filter (DPF) with an NSR catalyst [21], an NSR catalyst with an SCR catalyst [22], a HC trap and an NSR catalyst [23] and a DPF with an NSR [24]. In addition, NO_X reduction techniques incorporating high speed fuel injection for high temperature NO_X removal [25] or a combination of low temperature NO_X trapping and a reduction catalyst for low temperature NO_X removal [26, 27] are reported to be under development.

As noted above, various techniques to date have been developed to produce practical systems of NO_X removal under excess oxygen conditions and Fig. 3 suggests that the evolution of these techniques has significantly contributed to reducing the NO_X concentration in the atmospheric environment. Many researchers continue to work in this

field and additional future progress is expected to produce even more efficient NO_X removal systems.

3. Objectives and Abstract

This thesis is composed of three sections, all of which are focused on research concerning the removal of NO_X from automobile exhaust under excess oxygen conditions and improvement of the associated catalytic performance. Based on the background of the transition of NO_X removal technologies described above, analysis of reaction and deterioration mechanisms of NO_X purification catalysts are conducted and improvements related to the active catalytic centers are executed with the aim of the progress for NO_X removal performance.

In Part 1, the results of prior investigations of NO_X selective reduction catalysts are described, while in Chapter 2, data obtained through the *in situ* FTIR analysis of the reaction mechanism of an SCR catalyst using HC gas are presented. Here, the author suggests SCR over a Pt catalyst involves a N-containing hydrocarbon as the reaction intermediate and demonstrates that generation of this intermediate and its subsequent reaction with O_2 or NO_2 allow the SCR reaction to proceed. It is further concluded that enhancement of the oxidation-reduction performance of the catalyst by the activation of a noble metal is necessary to improve the SCR activity.

Chapter 3 summarizes attempts to improve catalytic performance by expanding both the temperature and A/F regions over which the catalyst is active. This chapter also addresses the usage of various reducing agents for SCR catalysis based on the reaction mechanisms discussed above. It was found that control of the oxidation state of Pt at active sites by the addition of Mo and Na enabled an expansion of the temperature region, which

in turn resulted in higher activity for NO_X removal. This is an important finding since it demonstrates the possibility of controlling the specific properties of the Pt catalyst via the incorporation of additives. This study also determined that a combination of Mo and alkali metals such as Na is effective in improving catalysis.

Chapter 4 further examines the reaction mechanisms of a Pt catalyst combined with Mo and Na, as introduced in the previous section. The addition of Mo and Na produce remarkably improved reaction selectivity for NO under lean conditions by controlling the oxidation state of Pt at active sites. It was also observed that the SCR reaction proceeds effectively using not only HC but also CO and H_2 as reducing agents. The author concludes that the most important factor involved in improving the catalyst is the effect of the interactions with the Mo and Na, which maintain the Pt particles in a metallic state even under lean conditions. These results indicate that control of the surface active species by interactions with additives is an effective means of improving both reactivity and selectivity during lean NO_X purification.

Part 2 focuses on methods of improving the sulfur tolerance of NSR catalysts, which is a significant problem, using NO_X storage materials. In Chapter 5, the author discusses the usage of TiO_2 to form a composite oxide with Ba as an NO_X storage compound intended to improve sulfur desorption and inhibit sulfur adsorption. NSR catalysts using a Ba-Ti composite oxide dispersed on the support surface were prepared and examined as to their structures and catalytic performance. It was found that the dispersion of Ba compounds in NO_X storage materials using a Ba-Ti complex solution is an efficient means of improving the durability of NSR catalysts. It was assumed that the existence of nano-scale Ba compounds combined with Ti inhibited the sintering of barium sulfate and its facile decomposition.

Chapter 6 analyzes the characteristics of the catalyst incorporating Ba-Ti composite oxide as an NO_X storage compound. The adsorption and desorption properties of sulfur on NSR catalysts containing Ba and K as storage materials and Al_2O_3 and TiO_2 as

supports are examined in order to confirm that the combination of Ba and Ti is effective at improving NSR activity with respect to sulfur poisoning. Further, an attempt is also made to understand the primary factors involved in generating the high performance of the BaTi catalyst using a Ba-Ti composite oxide. It is concluded that the nm-scale distribution of Ba and Ti on the BaTi catalyst is the principal factor contributing to the high performance of the catalyst in terms of its sulfur desorption rate and its ability to inhibit repetitive adsorption during rich treatment for sulfur desorption.

Finally, Part 3 discusses the effects and mechanism of a low temperature NO_X trapping catalyst in combination with a reduction catalyst, a system intended to improve NO_X removal at low temperatures. Chapter 7 summarizes the results of our investigation into the NO_X removal performance of a TiO_2-modified Ag-alumina ($AgTi/Al_2O_3$), and discusses the NO_X trapping mechanism based on its characterization. $AgTi/Al_2O_3$ improved the NO_X trapping performance of the catalyst by enhancing NO adsorption in the presence of other gases, including CO, hydrocarbons, CO_2 and H_2O. It was also determined that Ag supported on octahedral TiO_2 formed active sites at which the redox reaction between Ag^0 and Ag^+ proceeded, and that NO was effectively oxidized and adsorbed as nitro and nitrite species on the active surface composed of the dispersed Ag and TiO_2.

References

[1] National Greenhouse Gas Inventory Report of JAPAN, Ministry of the Environment, Japan (2012).

[2] National emissions reported to the Convention on Long-range Transboundary Air Pollution (LRTAP Convention) provided by The United Nations Economic Commission for Europe (Environment and Human Settlements Division).

[3] Future trends of Countermeasures to reduce the exhaust from automobile, Central Environment Council, Ministry of the Environment, Japan (2005).

[4] National emissions reported to the Convention on Long-range Transboundary Air Pollution (LRTAP Convention) provided by The United Nations Economic Commission for Europe (Environment and Human Settlements Division).

[5] T. Inoue, ISBN978-4-254-23771-9 C3353, Japanese Automotive Standards Organization, p23.

[6] M. Ozawa, M. Kimura, H. Sobukawa, K. Yokota, *Toyota Central R&D Review of Toyota CRDL* 27 (1992) 43-53.

[7] M. Iwamoto, H. Yahiro, Y. Yu-u, S. Shundo and N. Mizuno, *Shokubai (Catalyst)* 32 (1990) 430-433.

[8] S. Sato, Y. Yu-u, H.Yahiro, N. Mizuno and M. Iwamoto, *Appl. Catal.* 70 (1991) L1-L5.

[9] M. Misono and K. Kondo, *Chem. Lett.* (1991) 1001-1002.

[10] M. Sasaki, H. Hamada, Y. Kintaichi and T. Ito, *Catal. Lett.* 15 (1992) 297-304.

[11] T. Tanaka, T. Okuhara, M. Misono, *Appl. Catal. B* 4 (1994) L1-L9.

[12] T. Tanaka, K.Yokota, Japanese Unexamined Patent Application Publication No. Hei 8-10575.

[13] K. Yokota, M. Fukui T. Tanaka, *Appl. Surf. Sci.* 121 (1997) 273-277.

[14] F. Nakajima, I. Hamada, *Catal. Today* 29 (1996) 109-115.

[15] R. M. Heck, *Catal. Today* 53 (1999) 519-523.

[16] N. Miyoshi, S. Matsumoto, K. Katoh, T. Tanaka, J. Harada, N. Takahashi, K. Yokota, M. Sugiura, K. Kasahara, *SAE Tech. Paper* 950809 (1995).

[17] N. Takahashi, H. Shinjoh, T. Iijima, T. Suzuki, K. Yamazaki, K. Yokota, H. Suzuki, N. Miyoshi, S. Matsumoto, T. Tanizawa, T. Tanaka, S. Tateishi, K. Kasahara, *Catal. Today* 27 (1996) 63-69.

[18] Japan Automobile Manufacturers Association, Inc., eco_report2012, http://www.jama.or.o/wrestle/eco_report/pdf/eco_report2012_01.pdf; International Fuel

Quality Center, www.IFQC.org.

[19] T. Tanaka, I. Tajima, Y. Kato, Y. Nishihara, H. Shinjoh, *Applied Catalysis B: Environmental* 102 (2011) 620-626.

[20] T. Tanaka, K. Amano, K. Dohmae, N. Takahashi, H. Shinjoh, *Applied Catalysis A General* 455 (2013) 16-24.

[21] S. Hirota, K. Nakatani, S. Takeshima, K. Ito, T. Tanaka, K. Dohmae, Papers of Japanese Automotive Standards Organization, 34 (2003) 83-88.

[22] H. Shinjoh, N. Takahashi and K. Yokota, *Top. in Cat.* 42/43 (2007) 215-219.

[23] H. Onodera, M. Nakamura, M. Takaya, H. Akama, H. Itoyama, and S. Kimura, *SAE Paper* 2008-01-0449 (2008).

[24] K. Hirata, N. Masaki, M. Yano, H. Akagawa, J. Kusaka, K. Takada, T. Mori, Proceedings of COMODIA (2008) 65-72.

[25] Y. Bisaiji, K. Yoshida, M. Inoue, K. Umemoto, T. Fukuma, *SAE Int. J. Fuels Lubr.* 5(1) (2012) 380-388.

[26] T. Tanaka, H. Hamaguchi, T. Murasaki, M. Watanabe, D. Imai, Japanese Patent No.05290062.

[27] Y. Tsukamoto, H. Nishioka, D.i Imai, Y.i Sobue, N. Takagi, T. Tanaka, T. Hamaguchi, SAE 2012 World Congress & Exhibition 2012-01-0370.

Part 1

Improvement of NO_X selective reduction catalyst

Chapter 2

Intermediacy of organic nitro and nitrite surface species in selective reduction of nitrogen monoxide by propene in the presence of excess oxygen over silica-supported platinum.

Abstract

The role of surface species in the selective reduction of nitrogen oxides by propene in the presence of excess oxygen over Pt/SiO_2 has been studied at 393 K mainly with IR spectroscopy. Organic nitro, nitrite and carbonyl species were detected during the reaction. The reactions of those three species with nitrogen dioxide and oxygen took place rapidly, producing N_2, N_2O and CO_2, while the reactivities of those species with nitric oxide and propene were low. Hence, a mechanism is proposed, in which the nitro, nitrite and carbonyl surface species are key reaction intermediates. Similarity in the products between the selective reduction and the oxidation of nitro (nitromethane) or nitrite (n-butylnitrite) compound supported the proposed reaction scheme.

1. Introduction

Catalytic removal of dilute nitrogen oxides from the emission of diesel and lean-bum gasoline engines is now a very urgent problem. For the selective reduction of nitric oxide by hydrocarbons in oxygen-rich atmospheres, zeolite-based catalysts such as Cu-ZSM-5 [1, 2], Ce-ZSM-5 [3, 4], Ga-ZSM-5 [5] and Co-ZSM-5 [6] are reported to be efficient. Solid acids like Al_2O_3 and H-ZSM-5 are also found to be active [7]. It is well known that supported noble metal catalysts are active for the reaction of nitric oxide with H_2, CO or NH_3 [8, 9]. A three way catalyst system which consists of noble metals (Pt-Pd-Rh) has been used in catalytic control of automotive emissions. Such a catalyst works efficiently for an exhaust gas of nearly stoichiometric air to fuel ratio (about 14.7), but does not work for NO_X under lean-burn conditions [10]. Recently, it was reported, in addition to early patent literature [11], that supported platinum catalysts were active for the selective reduction of nitric oxide by propene in the presence of excess oxygen [12 - 14], while the main product was nitrous oxide.

Several reaction mechanisms have been proposed for the selective reduction of nitric oxide with hydrocarbons. It has been deduced that oxygen reacts with hydrocarbon to form partially oxidized hydrocarbons which are reactive to nitric oxide over Cu-ZSM-5 [15, 16]. On the other hand, it was reported that the reaction between nitrogen dioxide and hydrocarbon was crucial over Al_2O_3 [17] and Ce-ZSM-5 [18, 19]. Recently, Ukisu et al. [20] and Yahiro et al. [21] claimed that isocyanate (NCO) species were the reaction intermediate for Cu-Cs/Al_2O_3 and Cu-ZSM-5 catalysts. However, very little is known about the early steps of this reaction. For the development of efficient catalysts, a more profound understanding of the mechanism of this reaction is indispensable.

In the present study, we wish to report that organic nitro, nitrite and carbonyl compounds are formed on the surface of Pt/SiO_2 during the reaction of $NO + C_3H_6 + O_2$ and that they are the key surface species for the early stages of this reaction [22].

2. Experimental

5.5 wt% Pt/SiO_2 was prepared by impregnating SiO_2 (Reference Catalyst of Catalysis Society of Japan, JRC-SIO-4; 347 m^2g^{-1}) with an aqueous solution of $Pt(NH_3)_4(OH)_2$ (Yokozawa Kagaku Co.) followed by drying at 373 K for 24 h in air and calcination at 773 K for 5 h in air. Then the sample was pretreated in a hydrogen flow (100 $ml \cdot min^{-1}$) at 723 K for 5 h. The platinum dispersion was determined to be 15 % by carbon monoxide adsorption (based on the irreversible amount at room temperature), assuming that carbon monoxide was adsorbed on platinum atoms on the surface of the platinum particle at a 1:1 stoichiometry.

IR measurement was performed by using an in situ Pyrex IR cell (volume: 500 ml) with a NaCl window [23]. The cell was directly connected to a closed circulation system (about 500 ml) equipped with a gas chromatograph (Shimadzu 8A, thermoconductivity detector). A self-supporting disk of Pt/SiO_2 (about 50 mg) was placed in a sample holder made of Pyrex. In addition, Pt/SiO_2 (about 200 mg) was also placed in a basket (Quartz) in the IR cell. Both samples in the cel1 were again pretreated concurrently with hydrogen (30 Torr, 4 kPa) at 673 K for 0.5 h. After the samples had been cooled to the desired temperature in vacuum, they were exposed to a mixture of NO (3 Torr) + C_3H_6 (3 Torr) + O_2 (30 Torr).

The IR spectra were recorded with an FT-IR spectrometer (Shimadzu IR8500). The composition of the gas phase was analyzed with a gas chromatograph (Shimadzu GC 8A) with molecular sieve 5A (for O_2, N_2 and CO) and Porapak Q (for N_2O and CO_2) columns. In a separate experiment, the selective reduction of nitric oxide was carried out in a conventional flow reactor (Pyrex tube; 10 mm in diameter) with a mixture of NO 1000 ppm, C_3H_6 500 ppm, and O_2 10 % under W/F = $3.3 \cdot 10^{-3}$ $g \cdot min \cdot cm^{-3}$. Oxidation of nitromethane or n-butylnitrite was also performed in the same flow reactor. The feeds consisted of 1 % nitromethane or n-butylnitrite, O_2 10 % and He balance under W/F =

$5 \cdot 10^{-3}$ g·min·cm^{-3}.

3. Results and discussion

3.1. Surface species on Pt/SiO_2

Fig. 1 shows the infrared spectra of the adsorbed species on Pt/SiO_2 which was exposed to the mixture of NO + C_3H_6 + O_2. Before the introduction into the IR cell, part of the nitric oxide was converted to nitrogen dioxide by the reaction with oxygen. So, the reaction gas mixture actually consisted of NO + NO_2 + C_3H_6 + O_2. As shown in Fig. 1 a, two main peaks appeared at 1565 and 1655 cm^{-1} after the addition of the above mixture at room temperature, and their intensities became constant after 0.5 h at room temperature.

Evacuation at 393 K for 0.5 h changed the spectrum of Fig. 1 a into the spectrum shown in Fig. 1 b. With the decreases in the peak intensities of 1565 and 1655 cm^{-1}, a new peak at 1740 cm^{-1} appeared. In order to identify these peaks, ^{15}NO was used instead of ^{14}NO. The spectrum obtained is shown in Fig. 1 c, where the spectrum were recorded also after the sample was evacuated at 393 K for 0.5 h. It was found that the peaks at 1565 and 1655 cm^{-1} shifted to 1530 and 1615 cm^{-1}, respectively, but the peak position of the 1740 cm^{-1} band changed hardly, showing that the former species (1565 and 1655 cm^{-1}) contain nitrogen, but the latter does not. The small peak at about 1730 cm^{-1} in Fig. 1 a is probably due to nitric oxide or nitrogen dioxide adsorbed, since this peak shifted to 1692 cm^{-1} when ^{15}NO was used instead of ^{14}NO.

When NO_2 (3 Torr) or NO (3 Torr) alone was introduced to Pt/SiO_2 at room temperature, several broad peaks with similar intensities were observed at 1935, 1820, 1750, 1655 and 1565 cm^{-1} for nitrogen dioxide addition and 1780, 1710 and 1630 cm^{-1} for nitric oxide addition, respectively, while the peak intensities were one-third or less than those of Fig. 1 a. These band positions are consistent with the data in the literature and

assignable to adsorbed NO_X on platinum [24 - 27].

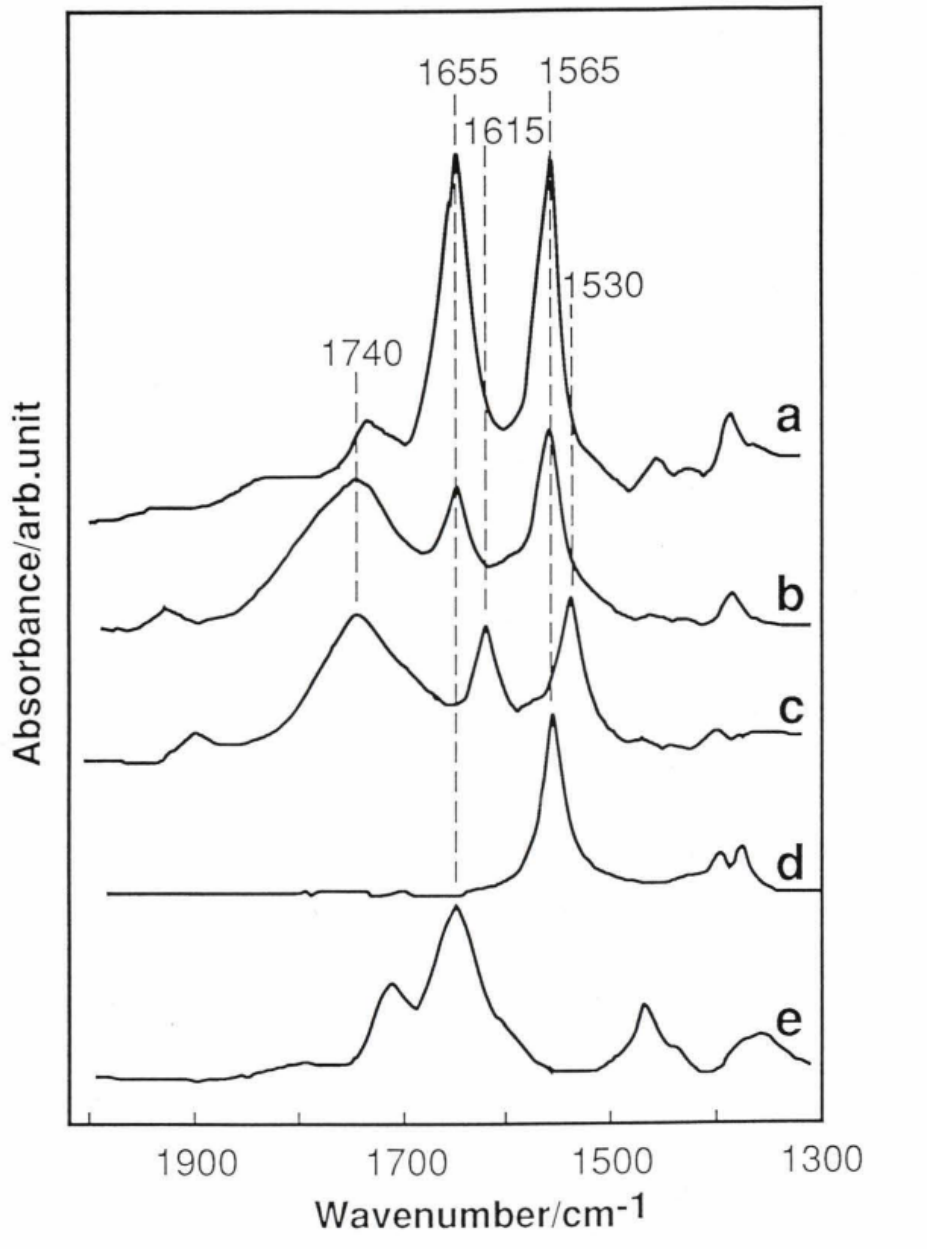

Fig. 1. Infrared spectra of adsorbed species on Pt/SiO_2. (a) 30 min after the addition of NO (3 Torr) + C_3H_6 (3 Torr) + O_2 (30 Torr) at room temperature, (b) evacuation for 30 min at 393 K after (a), (c) 30 min 15 after the addition of ^{15}NO (3 Torr) + C_3H_6 (3 Torr) + O_2 (30 Torr) followed by the evacuation (30 min) at 393 K, (d) after the addition of CH_3NO_2 (3 Torr) for 30 min, (e) after the addition of n-C_4H_9ONO (3 Torr) at room temperature.

Figs. 1 d and 1 e show the spectra of CH_3NO_2 (nitromethane) and n-C_4H_9ONO (n-butylnitrite) adsorbed on Pt/SiO_2 at room temperature. The adsorbed nitro methane and n-butylnitrite gave strong peaks at 1561 cm^{-1} and 1658 cm^{-1}, respectively, indicating that the bands at 1565 cm^{-1} and 1655 cm^{-1} in Fig. 1 a can be assigned to $\nu(NO_2)$ and $\nu(ONO)$ of organic nitro and nitrite compounds, respectively. These peak positions are in agreement with those reported in the literature [28].

When either the mixture of NO + C_3H_6 + O_2 or NO_2 + C_3H_6 was introduced to SiO_2 (without Pt) at 393 K, a spectrum similar to that for Pt/SiO_2 shown in Fig. l a was obtained, while the peak at 1730 cm^{-1} was very small. It is known that nitrogen dioxide is so reactive to alkenes that even in the gas phase the reaction takes place to form nitro and nitrite compounds [29, 30]. Therefore, the formation of organic nitro and nitrite species not only on Pt/SiO_2 or but also on SiO_2 is understandable.

As described above, the band at 1740 cm^{-1} did not show the isotopic shift upon the substitution of ^{14}NO by ^{15}NO. Hence, the peak is assignable to ν (CO) of organic carbonyl species from the peak position. This peak was not detected after the addition of C_3H_6 (3 Torr) + O_2 (30 Torr) or C_3H_6 (3 Torr) + NO (3 Torr) to Pt/SiO_2 at 393 K. Since the evacuation at 393 K of the nitro and nitrite species on SiO_2 did not give a peak at 1740 cm^{-1} (the carbonyl species), it is likely that platinum is necessary for the transformation of the nitro and nitrite species to the carbonyl species.

3.2. Reactivities of the surface species

The reactivities of these three surface species toward NO, NO_2, O_2, or C_3H_6 were examined by combining IR spectroscopy and the gas phase analysis. Fig. 2 shows the responses of the IR peaks of these species and of the pressures of nitrogen and nitrous oxide upon the addition of nitrogen dioxide at 393 K. Prior to the nitrogen dioxide addition, these species were produced on Pt/SiO_2 by the reaction with NO + C_3H_6 + O_2. The

decrease of the nitro and nitrite species was slow at 393 K in vacuum. When nitrogen dioxide was introduced instantaneously at 393 K, the band at 1740 cm^{-1} decreased rapidly and became constant, and at the same time nitrous oxide and nitrogen were produced in the gas phase. Carbon dioxide was also formed, of which the amount was about three times that of N_2 + N_2O. On the other hand, although changes of the nitro (1565 cm^{-1}) and nitrite peaks (1655 cm^{-1}) took place also, they were relatively small. After the addition of nitrogen dioxide, a weak peak at 1829 cm^{-1}, which is due to adsorbed nitrogen dioxide, appeared. Since adsorbed nitrogen dioxide also gave peaks at about 1655 and 1565 cm^{-1}, as described above, the bands due to adsorbed nitrogen dioxide may overlap with the bands of the nitro and nitrite species. As this may be a reason for the small changes of the nitro and nitrite peaks, reactions between nitrogen dioxide and the N-containing species are undeniable. However, the small changes of the peaks of N-containing species (Fig. 2) suggest that the contribution of the reactions is not significant. From the result of Fig. 2, it can be concluded that the reaction took place between carbonyl species and nitrogen dioxide, resulting in the formation of nitrogen and nitrous oxide.

The changes observed upon the oxygen addition are shown in Fig. 3. The three peaks decreased rapidly, accompanied by the formation of nitrogen and nitrous oxide (also carbon dioxide), while the total amount of nitrogen and nitrous oxide was slightly lower than that in the case of the nitrogen dioxide addition. On the other hand, the addition of nitric oxide or propene produced only small amounts of nitrogen and nitrous oxide; the amounts of N_2O + N_2 were less than 1/5 and 1/10 those in Fig. 2, respectively. The decreases in the IR peak intensities of nitro and nitrite species were also small. It was confirmed that the introduction of nitric oxide or nitrogen dioxide alone to Pt/SiO_2 did not produce any nitrogen and nitrous oxide at 393 K.

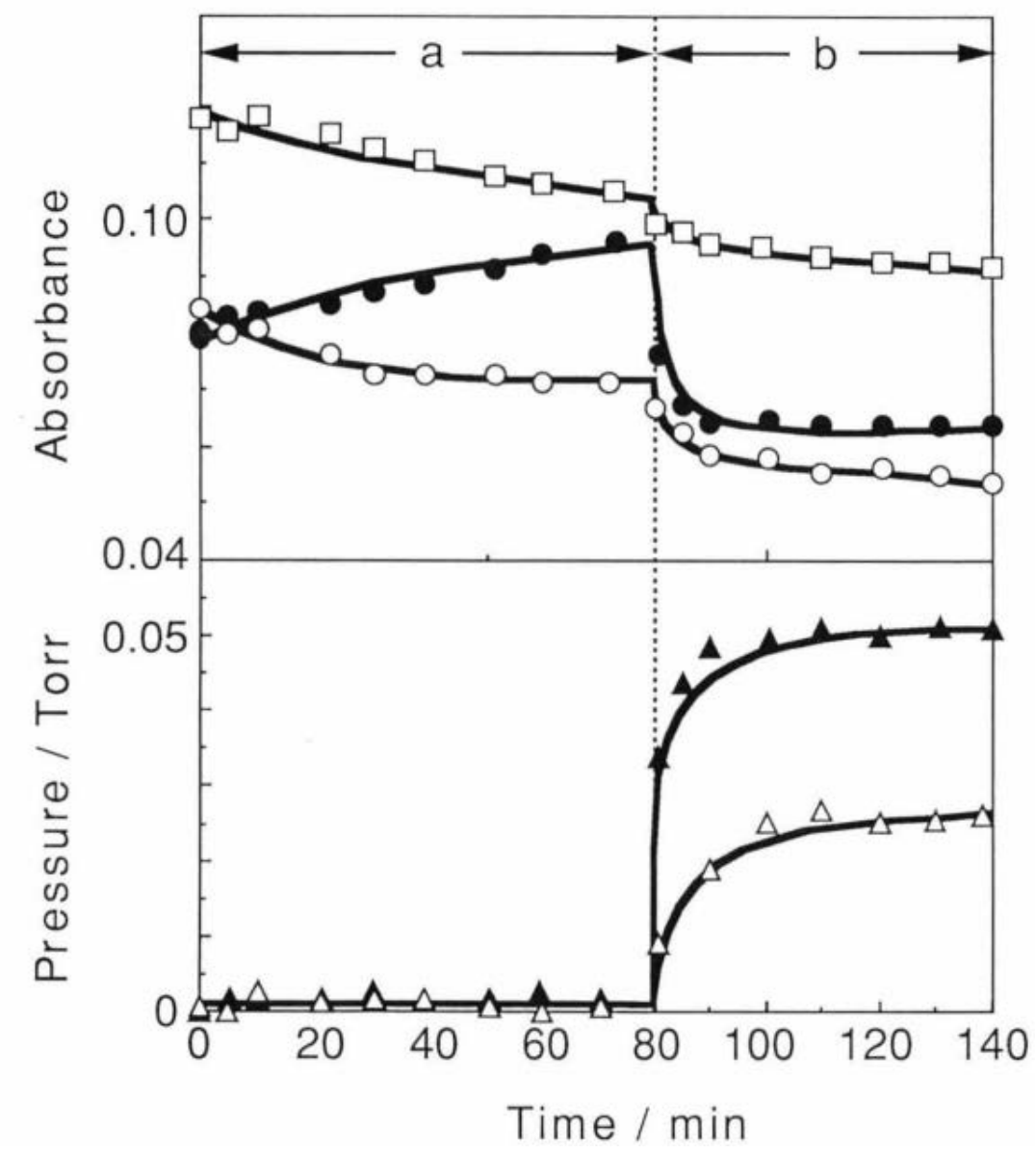

Fig. 2. Responses in the intensities of the IR bands and the partial pressures of N_2 and N_2O in the gas phase upon the addition of NO_2 to the surface species on Pt/SiO_2. Pt/SiO_2 was exposed to the mixture of NO (3 Torr) + C_3H_6 (3 Torr) + O_2 (30 Torr) at 393 K for 30 min and was evacuated at 393 K for 80 min (region a). Then NO_2 (3 Torr) was added at 393K (region b). □:1565 cm^{-1}, ○: 1655 cm^{-1}, ●: 1740 cm^{-1}, △:N_2, ▲:N_2O.

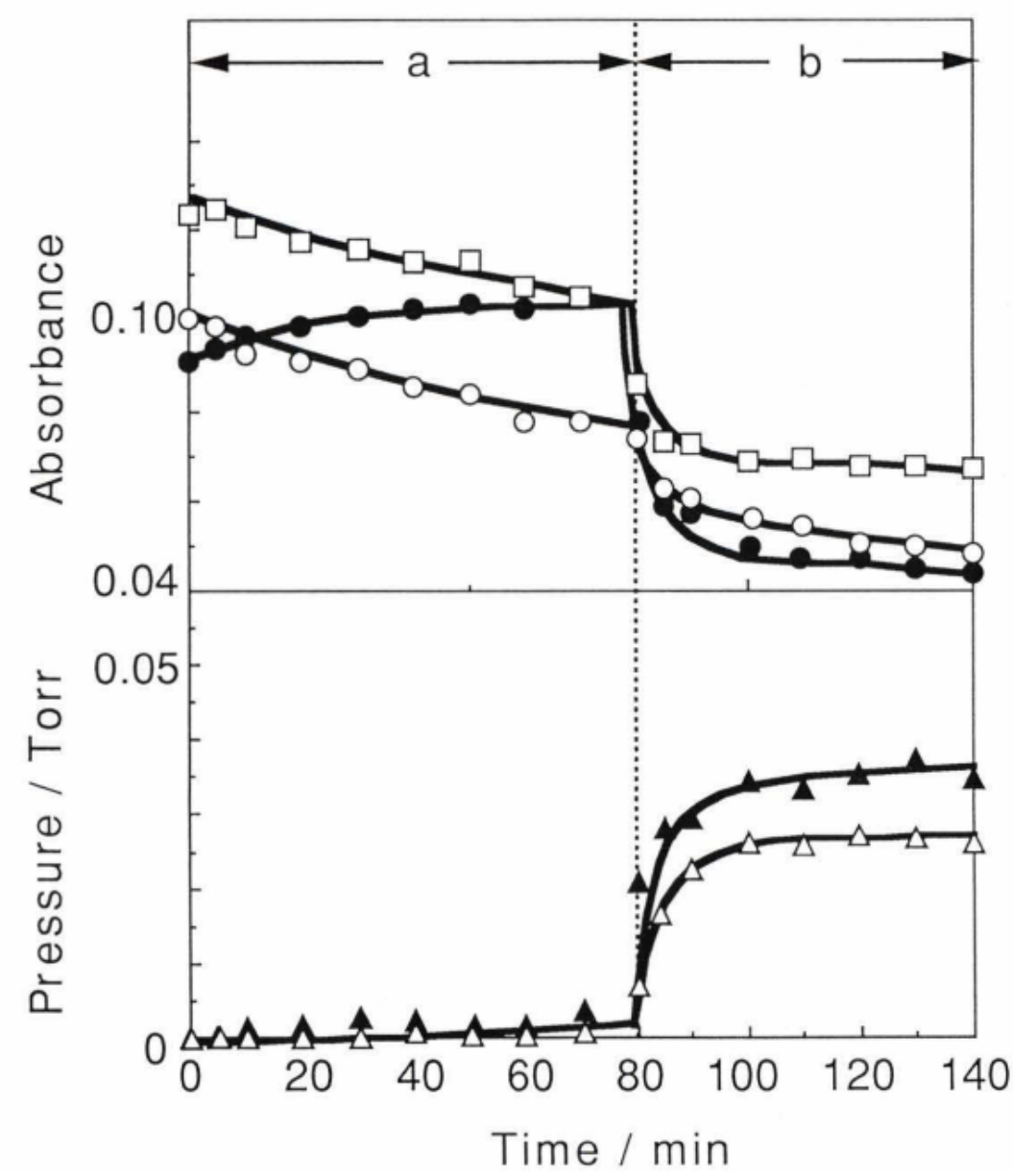

Fig. 3. Responses in the intensities of the IR bands and the partial pressures of N_2 and N_2O in the gas phase upon the addition of O_2 to the surface species on Pt/SiO_2. Pt/SiO_2 was exposed to the mixture of NO (3 Torr) + C_3H_6 (3 Torr) + O_2 (30 Torr) at 393 K for 30 min and was evacuated at 393 K for 80 min (region a). Then O_2 (30 Torr) was added at 393 K (region b). □:1565 cm^{-1}, ○: 1655 cm^{-1}, ●: 1740 cm^{-1}, △:N_2, ▲:N_2O.

From these results, we presume that the main reactions for the formation of nitrogen and nitrous oxide are the one between carbonyl species and nitrogen dioxide and those between N-containing species (nitro and nitrite) and oxygen. So we propose a reaction scheme as illustrated in Scheme 1 for the selective reduction nitric oxide. First, propene reacts with nitrogen dioxide which is formed from nitric oxide, resulting in the formation of nitro and nitrite, where oxidation of nitric oxide to nitrogen dioxide is accelerated by platinum. Then the nitro and nitrite partly change to carbonyl species at elevated temperatures. Nitrogen and nitrous oxide as well as carbon dioxide are formed mainly from the reactions between nitrogen dioxide and carbonyl species and between oxygen and the N-containing species. It was reported that acetone readily reacted with nitrogen dioxide (or N_2O_4) to diacetylfuroxane at 323 K [31].

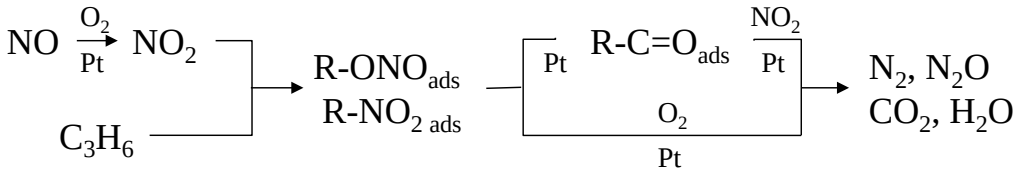

Scheme 1. A proposed reaction scheme for the selective reduction of NO in the presence of excess oxygen over Pt/SiO_2.

Note that parts of these species were inactive (see Figs. 2 and 3). Probably, the species adsorbed on the SiO_2 surface in Pt/SiO_2 did not react and changed hardly upon the addition of nitrogen dioxide or oxygen. In fact, nitro and nitrite species formed on SiO_2 alone changed little by the addition of oxygen.

3.3. Catalytic activity and selectivity

In order to confirm the above reaction scheme, the oxidation of model compounds as well as the selective reduction of nitric oxide by propene were performed using a flow reactor. As shown in Table 1, for the selective reduction, Pt/SiO_2 showed a maximum conversion to nitrogen and nitrous oxide at 473 K and the main component of the product of N-containing molecules is nitrous oxide, of which the selectivity was 62 - 74 % in the temperature range 423 - 573 K. This result is consistent with those in the literature [12].

Table 1.
Selective reduction of nitric oxide by propene in the presence of oxygen and oxidations of nitro and nitrite compounds

Catalysts	Reaction[a]	Temp./K	Conversion to		Selctivity[b] to N_2O /%
			N_2/%	N_2O/%	
Pt/SiO_2	$NO+C_3H_6+O_2$	423	10.8	25.3	70.1
		473	10.6	30.6	74.4
		523	5.6	13.3	70.4
		573	7.2	19.2	62.3
	$CH_3NO_2+O_2$	573	12.1	26.1	68.3
	$n\text{-}C_4H_9ONO+O_2$	473	14.1	39.2	73.1
SiO_2	$NO+C_3H_6+O_2$	673	<0.5	<0.5	-
	$CH_3NO_2+O_2$	573	1.2	0.6	32.8
	$n\text{-}C_4H_9ONO+O_2$	473	3.2	3.1	49.2

[a] NO (1000 ppm) + C_3H_6 (500 ppm) + O_2 (10 %); W/F = $3.3\cdot10^{-3}$ g·min·cm^{-3},
CH_3NO_2 (1 %) + O_2 (10 %); W/F = $5\cdot10^{-3}$g·min·cm^{-3},
$n\text{-}C_4H_9ONO$ (1 %) + O_2 (10%); W/F = $5\cdot10^{-3}$ g·min·cm^{-3}
[b] Selectivity = N_2O / (N_2 + N_2O) × 100 (on the basis of mol).

Oxidation of nitromethane over Pt/SiO_2 gave products similar to that of the selective reduction as far as the N-containing inorganic products are concerned; the selectivity to nitrous oxide was about 68 % at 573 K. Furthermore, n-butylnitrite was also oxidized to nitrogen and nitrous oxide with 73 % selectivity to nitrous oxide at 473 K. SiO_2 was much less active for both reactions. These catalytic results support the importance of the oxidation path via organic nitro and nitrite species as shown in Scheme 1.

Some researchers have inferred that the reaction proceeds through an isocyanate intermediate. Although it is possible that a part of the intermediates discussed here is transformed to nitrogen or nitrous oxide via isocyanate, no peak due to the isocyanate species was detected on Pt/SiO_2 in the present study. The important roles of the nitro species have also been claimed for the selective reduction over Ce-ZSM-5 [18, 19].

4. Conclusions

During the reaction of NO (NO_2) + C_3H_6 + O_2 at 393 K over Pt/SiO_2, organic nitro, nitrite and carbonyl species were detected on the surface by means of IR spectroscopy. It was found that these three species reacted rapidly with nitrogen dioxide and oxygen to form N_2, N_2O and CO_2, while these species were inactive to propene and nitric oxide. From the responses in the intensities of these IR bands upon the addition of nitrogen dioxide, we conclude that the main reactions for the formation of nitrogen and nitrous oxide are the one between carbonyl species and nitrogen dioxide and those between N-containing species (nitro and nitrite) and oxygen. The results of catalytic oxidations of nitromethane and n-butylnitrite on Pt/SiO_2 support the above conc1usion.

References

[1] M. Iwamoto, H. Yahiro, Y. Yu-u, S. Shundo and N. Mizuno, *Shokubai (Catalyst)* 32 (1990) 430-433.

[2] S. Sato, Y. Yu-u, H. Yahiro, N. Mizuno and M. Iwamoto, *Appl. Catal.* 70 (1991) L1-L5.

[3] M. Misono and K. Kondo, *Chem. Lett.* (1991) 1001-1002.

[4] C. Yokoyama and M. Misono, *Chem. Lett.* (1992) 1669-1672.

[5] K. Yogo, M. Ihara, I. Terasakì and E. Kikuchi, *Chem. Lett.* (1993) 229-232.

[6] Y. Li and J. N, Armor, *Appl. Catal. B* 1(1992) L31-L40.

[7] M. Sasaki, H. Hamada, Y. Kintaichi and T. Ito, *Catal. Lett.* 15 (1992) 297-304.

[8] E. Echigoya, *J. Jpn. petrol. Inst.* 23 (1980) 223-232.

[9] J. H. Jones, T. K. Kummer, K. Otto, M. Shelef and W. Weaver, *Environm. Sci. Tech.* 5 (1971) 790-798.

[10] K. Yokota, H. Mukai and Y. Fujitani, SAE850129 (1985).

[11] S. Kondoh, S. Matsumoto, K. Ishibashi and T. Utsumi, Jpn. Patent Publ. (Kokai) 3-232533 (1991).

[12] G. Zhang, T. Yamazaki, H. Kawakami and T. Suzuki, *Appl. Catal. B* 1 (1992) L15-L20.

[13] H. Hirabayashi, H. Yahiro, N. Mizuno and M. Iwamoto, *Chem. Lett.* (1992) 2235 -2236.

[14] A. Obuchi, A. Ohi, M. Nakamura, A. Ogata, K. Mizuno and H. Ohuchi, *Appl. Catal. B* 2 (1993) 71-80.

[15] Y. Yu, Y. Torikai, S. Sato, H. Hirose, H. Yahiro, N. Mizuno and M. Iwamoto, *Shokubai(Catalyst)* 33 (1991) 61-64.

[16] C. N. Montreuil and M. Shelef, *Appl. Catal. B* 1 (1992) L1-L8.

[17] M. Sasaki, H. Hamada, Y. Kintaichi and T. Ito, *Catal. Lett.* 15 (1992) 297-304.

[18] C. Yokoyama, H. Yasuda and M. Misono, *Shokubai (Catalyst)* 35 (1993) 122-124.

[19] H. Yasuda, T. Miyamoto, C. Yokoyama and M. Misono, *Shokubai (Catalyst)* 35 (1993) 386-389.

[20] Y. Ukisu, S. Sato, G. Muramatsu and K. Yoshida, *Catal. Lett.* 11 (1991) 177-181.

[21] H. Yahiro, Y. Yu-u, H. Takeda, N. Mizuno and M. Iwamoto, *Shokubai (Catalyst)* 35 (1993) 130-133.

[22] T. Tanaka, T. Okuhara and M. Misono, The 70th Meeting of Catalysis Society of Japan, Niigata, 3E204, 1992.

[23] K. Mizuno, M. Ikeda, T. Imokawa, J. Take and Y. Yoneda, *Bull. Chem. Soc. Jpn.* 49 (1976) 1788-1793.

[24] K. P. De Jong, G. R. Meiwas and J. W. Geus, *Appl. Surf. Sci.* 14 (1982) 73-84.

[25] J. Sarkany, M. Bortok and R. D. Gonzalez, *J. Phys. Chem.* 91 (1987) 4301-4305.

[26] B. A. Morrow, J. P. Chevrier and L. E. Moran. *J. Catal.* 91 (1985) 208-215.

[27] D. S. Dunn, M. W. Severson, J. L. Hylden and J. Overand, *J. Catal.* 78 (1982) 225-237.

[28] W. W. Simons (Editor), The Sadtler Handbook of Infrared Spectra, Sadtler Research Laboratories, Philadelphia, 1978.

[29] N. Levy and C. W. Scaife, *J. Chem. Soc.* (1946) 1093-1096.

[30] W. A. Pryor, J. W. Lightsey and D. F. Church, *J. Am. Chem. Soc.* 104 (1982) 6685-6692.

[31] L. I. Peterson, *Tetrahedron Lett.* (1966) 1727-1731.

Chapter 3

Selective catalytic reduction of NO over PtMo catalysts with alkaline or alkaline earth metal under lean static conditions

Abstract

The selective reduction of NO on various PtMoX-catalysts (X: Li, Na, K, Mg and Ca) loaded on metal oxides such as SiO_2, Al_2O_3, TiO_2, ZSM-5 and silicalite was studied in an oxygen-rich synthetic mixture simulated exhaust from an automotive lean-burn engine, and compared with that on $PtMo/SiO_2$, $PtNa/SiO_2$ and Pt/SiO_2 catalysts. The temperature window for the selective reduction of NO_X on the PtMoLi-, PtMoNa- and PtMoK-catalysts was found to be remarkably wider and to shift to a higher temperature than that on the other catalysts under lean static conditions.

1. Introduction

The selective catalytic reduction of NO_X by hydrocarbons and carbon monoxide under excess oxygen conditions has been an object of study for several years. A large amount of research has been carried out to attain a catalyst suitable for practical use. It has

been reported that copper ion-exchanged zeolites are efficient for the selective catalytic reduction of NO_X [1]. Some noble metal catalysts are found to be superior in the durability to the copper zeolite system under both the oxidizing and reducing conditions [1 - 4]. But the noble metal catalysts have a problem because the temperature window for the selective reduction of NO_X, which is from 200 ˚C to 350 ˚C, is too narrow for practical use. Bimetallic PtMo- and PdMo-catalysts have been demonstrated to create new catalytic properties [5, 6]. The modification of a noble metal catalyst with Mo provided catalysts with high selectivity for the NO_X to N_2 reaction near the stoichiometric point. The purpose of this study is to examine NO_X reduction on the PtMo-catalysts with various additives and supports under the excess oxygen conditions.

2. Experimental

Twelve catalysts composed of Pt, MoO_3, basic additives and various metal oxides were prepared by an impregnation method as summarized in Table 1. The $PtMoNa/SiO_2$ catalyst was prepared by the same method using SiO_2 powder (AEROSIL TT600, Nippon Aerosil Corp., 200 m^2/g), $CH_3COONa{\cdot}3H_2O$ (Wako Pure Chemical Industries), $(NH_4)_6Mo_7O_{27}{\cdot}4H_2O$ (Wako Pure Chemical Industries) and $Pt(NH_3)_2(NO_2)_2$ (Tanaka Precious Metal Co.), and calcined at 500 ˚C for 3 h in flowing 10 % H_2 / N_2. The Pt, MoO_3 and Na_2O loading amounts were 1.67 wt%, 12.3 wt% and 0.1 wt%, respectively. Other catalysts were prepared in the same way as described above starting from the corresponding additives and supports as shown in Table 1. The prepared catalysts were pressed into disks and pulverized to a 300 ~ 700 μm size.

The laboratory reactor system used in this experiment was similar to a previously described system [7]. The feed compositions and reaction conditions used in this study

were as follows: The simulated oxygen-rich synthetic mixture consisted of 4.3 % O_2, 0.12 % NO, 800 ppm C_3H_6, 0.12 % CO, 400 ppm H_2, 12.3 % CO_2, 3 % H_2O, and the balance N_2. This mixture simulated an air to fuel (A/F) ratio of 18 (lean mixture). For each light-off test, catalysts were exposed to the simulated exhaust at 3.3 l/min while the temperature was decreased from 600 ˚C to 100 ˚C at 5 ˚C /min and at 9.91×10^{-3} g·sec/cc W/F. The activity was determined by continuously measuring the concentration of NO_X ($NO + NO_2$) with a chemiluminescent NO_X analyzer (Horiba, MEXA-8120).

Table 1. Catalyst formulations

Catalyst	Pt loading (wt%)	MoO_3 loading (wt%)	additive	loading (wt%)	Support
$PtMoNa/SiO_2$	1.67	12.3	Na_2O	0.1	SiO_2
$PtMoLi/SiO_2$	1.67	12.3	Na_2O	0.1	SiO_2
$PtMoK/SiO_2$	1.67	12.3	Na_2O	0.1	SiO_2
$PtMoMg/SiO_2$	1.67	12.3	Na_2O	0.1	SiO_2
$PtMoCa/SiO_2$	1.67	12.3	Na_2O	0.1	SiO_2
$PtMoNa/Al_2O_3$	1.67	12.3	Na_2O	0.1	Al_2O_3
$PtMoNa/TiO_2$	1.67	12.3	Na_2O	0.1	TiO_2
PtMoNa/ZSM-5	1.67	12.3	Na_2O	0.1	ZSM-5
PtMoNa/silicalite	1.67	12.3	Na_2O	0.1	silicalite
$PtMo/SiO_2$	1.67	12.3	-	0	SiO_2
$PtNa/SiO_2$	1.67	0	Na_2O	0.1	SiO_2
Pt/SiO_2	1.67	0	-	0	SiO_2

3. Results and discussion

Fig. 1 shows the conversions of NO_X on the $PtMoNa/SiO_2$, $PtMo/SiO_2$, $PtNa/SiO_2$ and Pt/SiO_2 catalysts as a function of temperature.

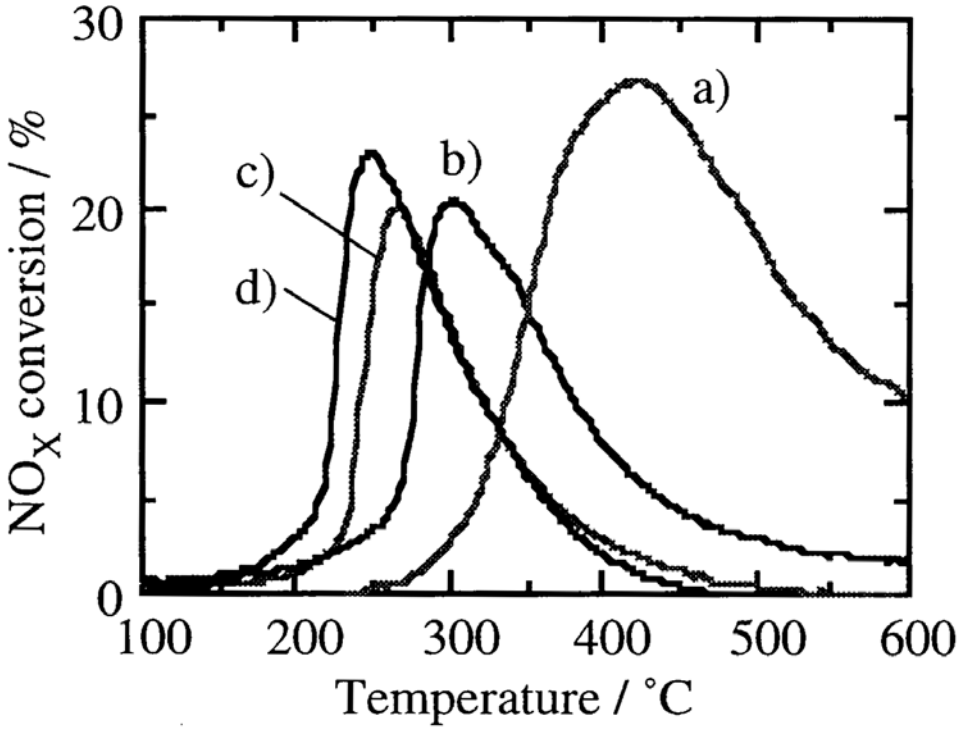

Fig. 1. NO_X conversion efficiency as a function of temperature in simulated oxygen-rich feed stream. The following catalysts are indicated: a) $PtMoNa/SiO_2$, b) $PtMo/SiO_2$, c) $PtNa/SiO_2$ and d) Pt/SiO_2. Calcination conditions: 500 ˚C, 10 % H_2/N_2, 3 h. The reactions were carried out on a 0.5 g of sample exposed to the simulated exhaust gas composed of 4.3 % O_2, 0.12 % NO, 800 ppm C_3H_6, 0.12 % CO, 400 ppm H_2, 12.3 % CO_2, 3 % H_2O and the balance N_2 at 3.3 l/min.

The Pt/SiO_2 and $PtNa/SiO_2$ catalysts had the maximum conversions of NO_X at temperatures from 250 to 260 ˚C. The conversions of NO_X by these catalysts rapidly decreased with increasing temperature above 260 ˚C. These temperature dependences of the NO_X selective reduction were the same as that of previously reported Pt catalysts [2, 3]. The temperature of the maximum NO_X conversion (300 ˚C) on the $PtMo/SiO_2$ catalyst was

about 50 ˚C higher than that on the Pt/SiO_2 catalyst. The conversion of NO_X gradually decreased with increasing temperature above 300 ˚C. On the other hand, the maximum NO_X conversion temperature (400 ~ 450 ˚C) on the $PtMoNa/SiO_2$ catalyst was about 150 to 250 ˚C higher than that on the Pt/SiO_2 catalyst. These results show that the addition of both Na_2O and MoO_3 plays a significant role in the reactivity of Pt on the $PtMoNa/SiO_2$ catalyst.

Fig. 2 shows the conversions of NO_X on the $PtMoLi/SiO_2$, $PtMoK/SiO_2$, $PtMoMg/SiO_2$ and $PtMoCa/SiO_2$ catalysts as a function of temperature.

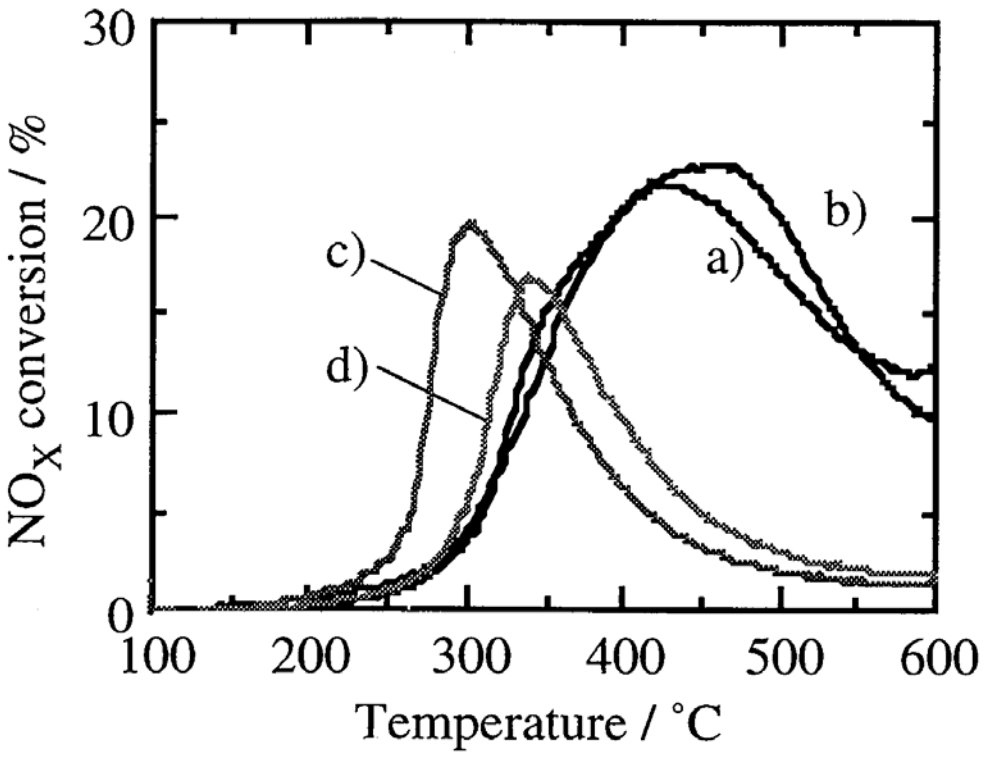

Fig. 2. NO_X conversion efficiency as a function of temperature in simulated oxygen-rich feed stream. a) $PtMoLi/SiO_2$, b) $PtMoK/SiO_2$, c) Pt $MoMg/SiO_2$ and d) $PtMoCa/SiO_2$. Calcination and the reaction conditions are shown in Fig. 1.

The $PtMoLi/SiO_2$ and $PtMoK/SiO_2$ catalysts had the maximum conversion of NO_X at temperatures from 400 to 500 ˚C. The temperature dependence of NO_X conversion of these catalysts had the features similar to the $PtMoNa/SiO_2$ catalyst in Fig. 1. On the other hand, the $PtMoMg/SiO_2$ and $PtMoCa/SiO_2$ catalysts had the maximum conversion of NO_X below 350 ˚C, and the features were similar to the $PtMo/SiO_2$ catalyst in Fig. 1. These results show that the addition of alkaline metals to the $PtMo/SiO_2$ catalyst had a significant effect on the shift in the temperature windows of the NO_X conversion on the PtMo catalysts.

Fig. 3 shows the conversions of NO_X on $PtMoNa/Al_2O_3$, $PtMoNa/TiO_2$, PtMoNa/ZSM-5 and PtMoNa/silicalite catalysts as a function of temperature.

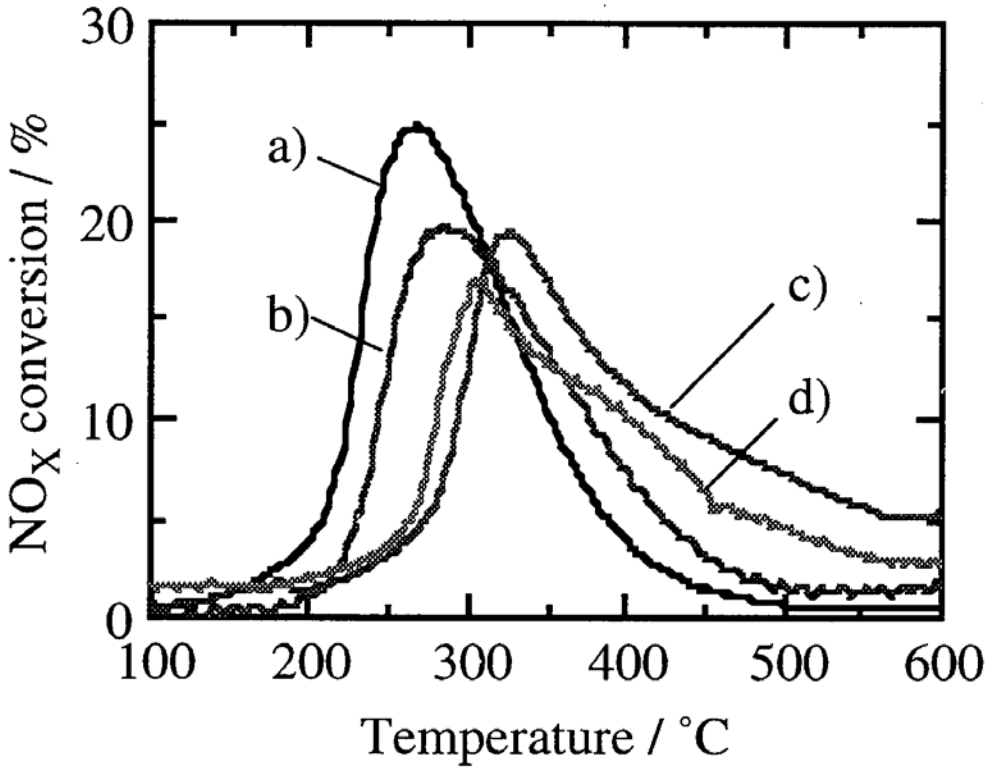

Fig. 3. NO_X conversion efficiency as a function of temperature in simulated oxygen-rich feed stream. a) $PtMoNa/Al_2O_3$, b) $PtMoNa/TiO_2$, c) PtMoNa/ZSM-5 and d) PtMoNa/silicalite. Calcination and the reaction conditions are shown in Fig. 1.

The $PtMoNa/Al_2O_3$ and $PtMoNa/TiO_2$ catalysts had the maximum conversions of NO_X below 300 ˚C, and had features similar to the $PtMo/SiO_2$ catalyst. The conversions of NO_X on PtMoNa/ZSM-5 and PtMoNa/silicalite catalysts were higher than those of the $PtMoNa/Al_2O_3$ and $PtMoNa/TiO_2$ catalysts at temperatures from 400 to 500 ˚C. But the NO_X conversion curves of these catalysts were not similar to that of the $PtMoNa/SiO_2$ catalyst. These results show that the support also affects the reaction characteristics of the PtMoNa catalysts.

A number of papers have already described that the temperature of the maximum NO_X conversion for the selective reduction of NO_X on Pt catalysts shifted as the Pt loadings [3], Pt precursor [3], and aging conditions changed. In these cases, the maximum NO_X conversion decreased with increasing temperature. On the other hand, for the selective reduction of NO_X on the $PtMo/SiO_2$ catalysts with alkaline metal additives, the maximum NO_X conversion increased as its temperature increased. Also, these catalysts had an upper temperature window of 350 ˚C for the selective NO_X reduction. These results are assumed to be due to the decrease in the affinity between oxygen and Pt by the addition of Mo and alkaline metals on the SiO_2 support.

References

[1] M. Iwamoto and N. Mizuno, *Shokubai (Catalyst)* 32 (1990) 462-468.

[2] G. Zhang, T. Yamazaki, H. Kawakami and T. Suzuki, *Appl. Catal., B: Environmental* 1 (1992) L15-L20.

[3] R. Burch, P. J. Millington and A.P. Walker, *Appl. Catal. B: Environmental* 4 (1994) 65-94.

[4] T. Tanaka, T. Okuhara and M. Misono, *Appl. Catal. B: Environmental* 4 (1994) L1-L9.

[5] H. S. Gandhi, H.C. Yao, and H. K. Stepien, in A. T. Bell and L. Hegedus (editors),

ACS Symp. Ser. No.178, Catalysis under Transient Conditions (1982) 143.

[6] T. E. Hoost, G.W. Graham, M. Shelef, O. Alexeev and B. C. Gates, *Catal. Lett.* 38 (1996) 57-81.

[7] H. Muraki, H. Shinjoh, H. Sobukawa, K. Yokota and Y. Fujitani, *Ind. Eng. Chem., Prod. Res. Dev.* 25 (1986) 202-208.

Chapter 4

Effect of the addition of Mo and Na to Pt catalysts on the selective reduction of NO.

Abstract

The selective reduction of NO_X by reductants such as C_3H_6 and CO in oxidizing feedstreams simulated exhaust from automobile engine and three-way behavior around the stoichiometric point have been investigated on trimetallic $PtMoNa/SiO_2$ catalysts, over a wide range of temperatures compared with bimetallic $PtMo/SiO_2$ catalyst and monometallic Pt/SiO_2 catalyst. The simultaneous addition of Mo and Na to Pt catalysts has been found to improve the following reaction characteristics on selective reduction of NO_X and three-way activity of conventional Pt catalyst. The temperature window on selective reduction of NO_X on trimetallic $PtMoNa/SiO_2$ catalysts was found to be wider and to shift at higher temperature than that on bimetallic $PtMo/SiO_2$ and monometallic Pt/SiO_2 catalysts under lean static conditions. The redox ratio window, in which three-way activity occurred on trimetallic $PtMoNa/SiO_2$ catalysts, was also found to be wider than that on bimetallic $PtMo/SiO_2$ catalysts and monometallic Pt/SiO_2 around stoichiometric point. On the other hand, XPS, IR and CO adsorption data indicated that the oxidation of Pt on

$PtMoNa/SiO_2$ catalysts was depressed by the added Mo and Na even under excess oxygen conditions, so that the reaction characteristics of trimetallic $PtMoNa/SiO_2$ catalysts was improved.

1. Introduction

Lean-burn gasoline and diesel engines achieve high fuel economy using higher air/fuel ratio (A/F). However, it is difficult to remove NO_X in exhaust gases from these engines under excess oxygen conditions. Selective catalytic reduction of NO_X under such excess oxygen conditions has been an object of study for several years. A large number of researches have been carried out to attain a catalyst enough to bear a practical use. It has been reported that ion-exchange zeolites such as Cu-ZSM-5 [1 - 4] are efficient for the reduction of NO by hydrocarbons in the presence of excess oxygen. Some noble metal catalysts [5 - 12] are also found to be more active and durable than Cu-ZSM-5.

It is well known that supported noble metal catalysts are active for the reaction of NO with H_2, CO or NH_3 [13, 14]. Three-way catalysts (TWCs) which consist of noble metals and several oxides have been used for the catalytic control of automotive emissions. Such catalysts work efficiently in engine exhaust oscillating just rich of the stoichiometric air-to-fuels (A/F) ratio in a narrow A/F window, so conversion of NO_X, CO and hydrocarbons (HC) occurs, but do not work in a lean static exhaust [15]. Recently, a new concept TWC, which removes NO_X, CO and HC under rich-lean dynamic conditions, has been developed and practically used [16, 17]. But the new concept TWC is not expected to remove NO_X under static lean conditions.

Bimetallic Pt-Mo and Pd-Mo catalysts have been demonstrated to modify the catalysis of each component and to create new catalytic properties such as hydrogenolysis

[18 - 20], hydrogenation [21], NO_X reduction [22 - 24], and unusual characterization [25 - 27]. So we investigated on trimetallic catalysts such as Pt-Mo-Na and Pt-Mo-Ca using several supports such as Al_2O_3, SiO_2, TiO_2, etc. in preparatory experiments [28].

The purpose of this study was to examine NO_X reduction and three-way activity of the $PtMoNa/SiO_2$ catalysts compared with those of PtMo, PtNa and Pt/SiO_2 catalysts. Another purpose was to present XPS, IR and CO adsorption results to clarify the state of Pt on these catalysts in the simulated model gases.

2. Experimental

2.1. Catalyst preparation

Eight catalyst formulations were prepared for use in this study as summarized in Table 1.

The $PtMoNa/SiO_2$ catalysts were prepared using the following method. SiO_2 powder (AEROSIL TT600, Nippon Aerosil, 200 m^2/g) was contacted with an aqueous solution of $CH_3COONa{\cdot}3H_2O$ (Wako Pure Chemical Industries), followed by drying at 80 ˚C for 12 h, and then calcined in air at 500 ˚C for 3 h. After cooling to 25 ˚C, the calcined powder was contacted with an aqueous solution containing $(NH_4)_6Mo_7O_{27}{\cdot}4H_2O$ (Wako Pure Chemical Industries), followed by drying at 80 ˚C for 12 h, and then calcined in air at 700 ˚C for 3 h. After cooling to 25 ˚C, the cooled powder was impregnated with the noble metal by contacting with an aqueous solution of $Pt(NH_3)_2(NO_2)_2$ (Tanaka Precious Metal). The obtained powder was dried at 80 ˚C for 12 h, preheated at 300 ˚C for 3 h in air, calcined at 500 ˚C for 3 h in 10 % H_2/N_2, and finally cooled to 25 ˚C. The Pt loading amount of 1.67 wt% was chosen as it was comparable to the Pt loading amount of ca. 1 - 2

wt% used in other studies [5, 7, 22]. The MoO_3 loading amount of 12.3 wt% was chosen because we have observed in our other preparatory experiment that the high conversion of NO_X has been observed when Mo-to-Pt ratio was nearly equal to 10 in the $PtMoNa/SiO_2$ catalysts. The Na_2O loading amounts of 0.05, 0.1 and 1.0 wt% were chosen to investigate the effect of Na addition to the $PtMoNa/SiO_2$ catalysts.

Table 1. Catalyst formulations

No.	Catalyst	Loading amount (wt%)			Support
		Pt	MoO_3	Na_2O	
1	PMNS1	1.67	12.3	0.05	SiO_2
2	PMNS2	1.67	12.3	0.1	SiO_2
3	PMNS3	1.67	12.3	1.00	SiO_2
4	PS	1.67	0	0	SiO_2
5	NS	0	0	0.1	SiO_2
6	MS	0	12.3	0	SiO_2
7	PNS	1.67	0	0.1	SiO_2
8	PMS	1.67	12.3	0	SiO_2

The $PtMo/SiO_2$, $PtNa/SiO_2$, and Pt/SiO_2 catalysts were prepared as it was comparable to $PtMoNa/SiO_2$ catalysts in the same way as described above except that aqueous solutions of $CH_3COONa{\cdot}3H_2O$, $(NH_4)_6Mo_7O_{27}{\cdot}4H_2O$ and both, respectively, were not used. The Mo/SiO_2 and Na/SiO_2 catalysts were prepared as they were comparable to the $PtMo/SiO_2$ and $PtNa/SiO_2$ catalysts in the same way as described above, respectively. 12.3 wt% MoO_3, 0.1 wt% Na_2O and 1.67 wt% Pt loading amounts were chosen for these catalysts. The prepared catalysts were pressed in disks and pulverized to 300 - 700 μm size.

2.2. Activity measurement

The laboratory reactor system used in this experiment is similar to the previously described system [29]. Catalytic activity data were obtained using a conventional fixed-bed flow reactor at atmospheric pressure. A quartz tube with an i.d. of 18 mm was chosen as the reactor tube. 0.5 g catalyst (~1 cm^3) was placed on a quartz filter at the middle part of the reactor. The upper part of the catalyst bed was packed with 7 cm^3 of inactive SiC spheres (3 mm o.d.) for preheating the feed gas. Furnace temperature was controlled with a maximum variation of 2 ˚C by an automatic temperature controller. The gas leaving the reactor was led to a condenser to remove the water vapor. The remaining components were continuously analyzed by nondispersive infrared (CO and CO_2), flame ionization (HC), magnetic susceptibility (O_2) and chemiluminescence (NO_X) equipped with gas analyzer (Horiba MEXA-8120).

We chose propene to simulate hydrocarbon in the feedstream in order to measure the activity of the prepared catalysts on hard conditions.

The redox ratio, S, is used to identify the redox characteristic of the model gas mixtures and is defined as in Scheme 1. When S < 1.0, S = 1.0 and S > 1.0, the composition of the feedstream is net reducing, stoichiometric, and net oxidizing, respectively.

$$S = \frac{[NO] + 2[O_2]}{[H_2] + [CO] + 9[C_3H_6]}$$ - Scheme 1

The feed compositions and reaction conditions used in this study were as follows:

1. Simulated oxidizing feed stream consisted of 4.3 % O_2, 0.12 % NO, 800 ppm C_3H_6, 0.12 % CO, 400 ppm H_2, 12.3 % CO_2, 3 % H_2O and a balance of N_2. This mixture

corresponded to S = 9.91 and simulated an A/F ratio of 18 (lean mixture). For each light-off test, catalysts were exposed to the simulated exhaust at 3.3 l/min while the temperature was decreased from 600 ˚C to 100 ˚C at 5 ˚C/ min and at 9.91×10^{-3} g s/cm^3 W/F.

2. Simulated exhaust gases for S-scan were composed of 0.40 - 1.21 % O_2, 0.12 % NO, 490 - 620 ppm C_3H_6, 0.45 - 1.50 % CO, 0.15 - 0.50 % H_2, 10.0 % CO_2, 3.0 % H_2O and a balance of N_2. Catalytic activities of the catalysts were expressed as percent conversion of NO_X, C_3H_6 and CO. Conversion data were measured at 300 ˚C, 400 ˚C and 450 ˚C and 9.91×10^{-3} g s/cm^3 W/F. The light-off temperature which is necessary to obtain a 50 % conversion was determined from the activity data. The activity measurements as a function of S are designated as S-scan. In these experiments, S is changed gradually from reducing to oxidizing conditions by adjusting the O_2, C_3H_6, CO and H_2 contents at the inlet of the reactor.

2.3. Infrared spectroscopy

IR spectra was recorded on a JASCO FTIR-8900 spectrometer equipped with an MCT detector and a diffuse reflectance IR cell. Catalyst sample placed in an in situ IR cell with a KBr window was pretreated at 400 ˚C for 1 h in flowing 7 % O_2/N_2 (O_2 pretreatment), and then cooled to 200 ˚C. CO was adsorbed at 200 ˚C in flowing 0.28 % CO/N_2 and IR spectra were measured. The IR spectra of CO adsorbed on the sample were obtained by subtracting the spectra before CO adsorption from those after that. In another IR measurement, other catalyst samples were pretreated in flowing N_2 (N_2 pretreatment) and 7 % H_2/N_2 (H_2 pretreatment) in the same procedure as mentioned above except pretreating in flowing 7 % O_2/N_2.

2.4. X-ray photoelectron spectroscopy (XPS)

In situ XPS measurements were performed on a V.G. SCIENTIFIC ESCALAB MK III with Mg Ka X-rays. Catalyst sample was placed on a grid, and preheated under 1×10^{-7} torr O_2 pressure at 400 ˚C for 1 h. The preheated sample was cooled down to room temperature under the same atmosphere, and then transferred into the XPS measurement stage. The binding energy was calibrated using the Si 2p (103.4 eV).

2.5. X-ray diffraction (XRD)

XRD measurement was recorded on a RIGAKU RU-3L equipped with a Co source (Co Ka radiation). Samples of catalyst powder were pressed into wafers and affixed to standard-sized microscope slides. Calculations for average crystallite size were made using Pt (111) line width in Scherrer's equation, with the Gaussian lineshape approximation.

2.6. Chemisorption of CO

Chemisorption measurement of CO was carried out by a pulse technique with chromatographic analysis. Catalyst samples placed in a flow reactor were pretreated at 400 ˚C for 15 min in flowing H_2 and cooled to 25 ˚C. After that several pulses of CO were introduced to the reactor until reaching equilibrium. The surface dispersion of Pt was calculated assuming that one molecule of CO adsorbs on an atom of Pt.

3. Results and discussion

3.1. Catalytic activity under excess oxygen conditions

In Fig. 1(A) - (C) are shown the conversions of NO_X, C_3H_6, and CO, respectively, on PS, PNS, PMS, PMNS1, PMNS2, and PMNS3 catalysts in simulated oxidizing feed stream as a function of temperature. As shown in Fig. 1(A), the NO_X conversion curves are classified into three groups: The first group is composed of the NO_X conversion curves on the catalysts without MoO_3 such as PS and PNS catalysts, the second group is of that on the catalyst with MoO_3 and without Na_2O such as PMS catalyst, and the third group is of those on the catalysts with MoO_3 and Na_2O such as PMNS1, PMNS2, and PMNS3 catalysts.

In the first group, the PS catalyst has the maximum conversion of NO_X at 250 ˚C. Below 250 ˚C, the curve of the conversion of NO_X on PS catalyst in Fig. 1(A) corresponds with that of C_3H_6 in Fig. 1(B). But that of CO on PS catalyst in Fig. 1(C) does not correspond with that of NO_X in Fig. 1(A) because CO reacts with oxygen exclusively and C_3H_6 reacts with NO_X on PS catalyst below 250 ˚C. The conversion of NO_X rapidly decreases with increasing temperature above 250 ˚C. This temperature dependence of NO_X selective reduction had been already described [5 - 7]. On the other hand, PNS catalyst has the maximum conversion of NO_X at 260 ˚C in Fig. 1(A) and has the analogous feature to PS catalyst in Fig. 1(A) - (C). This result indicates that the addition of Na_2O to PS catalyst does not play a significant role for the reactivity of Pt on the PNS catalyst.

In the second group, the maximum NO_X conversion temperature (300 ˚C) and light-off temperature of C_3H_6 and CO on the PMS catalyst are about 50 ˚C higher than those on PS catalyst. Below 300 ˚C, the curve of the conversion of NO_X on PMS catalyst in Fig. 1(A) corresponds with those of C_3H_6 and CO in Fig. 1(B) and (C). These results suggest that both C_3H_6 and CO react with NO_X on PMS catalyst below 300 ˚C. The

conversion of NO_X gradually decreases with increasing the temperature above 300 ˚C. These results indicate that the addition of MoO_3 to PS catalyst plays a significant role for the reactivity of Pt on PMS catalyst.

In the third group, the maximum NO_X conversion temperature (400 - 450 ˚C) and light-off temperature of CO (320 - 420 ˚C) on PMNS1, PMNS2 and PMNS3 catalysts are about 150 - 250 ˚C higher than those on PS catalyst as shown in Fig. 1(A) and (C). However, the light-off temperature of C_3H_6 (320 - 370 ˚C) on PMNS1, PMNS2 and PMNS3 catalysts is about 100 - 150 ˚C higher than that on PS catalyst as shown in Fig. 1(B). The maximum NO_X conversion and its temperature on PMNS1, PMNS2 and PMNS3 catalysts increase with increasing amount of Na_2O added to these catalysts as shown in Fig. 1(C). These results indicate that the addition of Na_2O plays a significant role for the reactivity of Pt on PMNS1, PMNS2 and PMNS3 catalysts. Increasing amount of Na_2O tends to increase reactivity of C_3H_6 with O_2 to form CO. In particular, the up-down curve of the conversion of CO on PMNS3 catalyst indicates that a partial oxidation of C_3H_6 occurs to form CO in the temperature range 350 - 400 ˚C.

A number of papers had already described that the temperature of the maximum NO_X conversion for selective reduction of NO_X on Pt catalysts changed as Pt loadings [6], Pt precursor [7] and aging conditions did. In these cases, the maximum NO_X conversion decreased with increasing temperature, which has been explained by the changing of the number of active sites on Pt. On the other hand, for selective reduction of NO_X on the $PtMoNa/SiO_2$ catalysts, the maximum NO_X conversion increases as its temperature increases. This result can be explained by the improvement of the reaction characteristics of Pt inherent in the addition of Mo and Na, as mentioned below.

MS and NS catalysts have not only the activity of NO_X reduction but also C_3H_6 and CO oxidation in simulated oxidizing feed stream in the temperature range under 600 ˚C.

A)

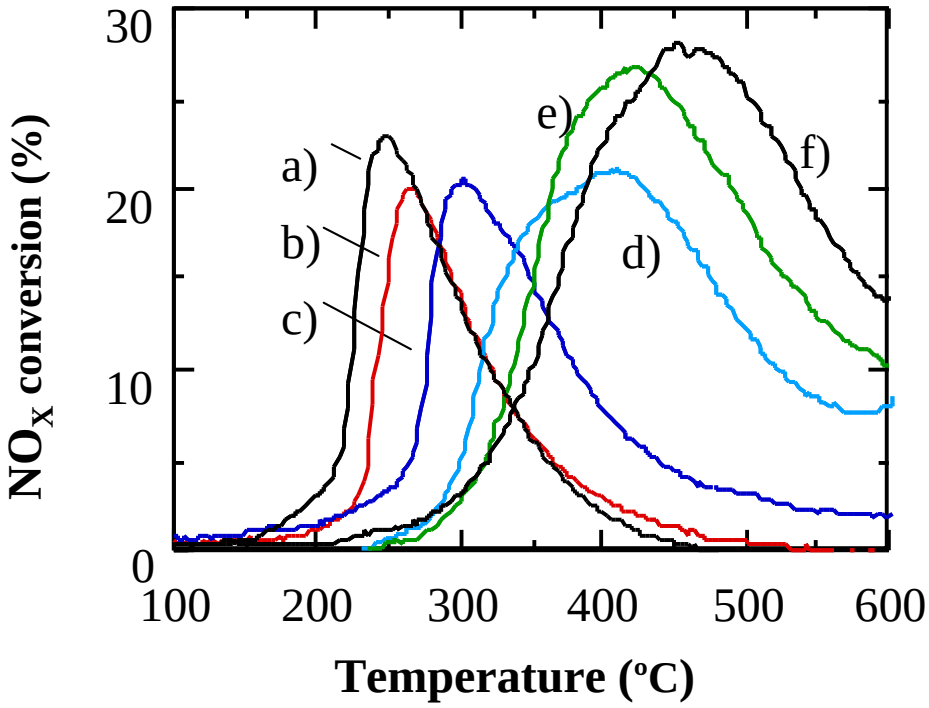
30
20
10
0
100
200
300
400
500
600
a)
b)
c)
d)
e)
f)
NOx conversion (%)
Temperature (°C)

B)

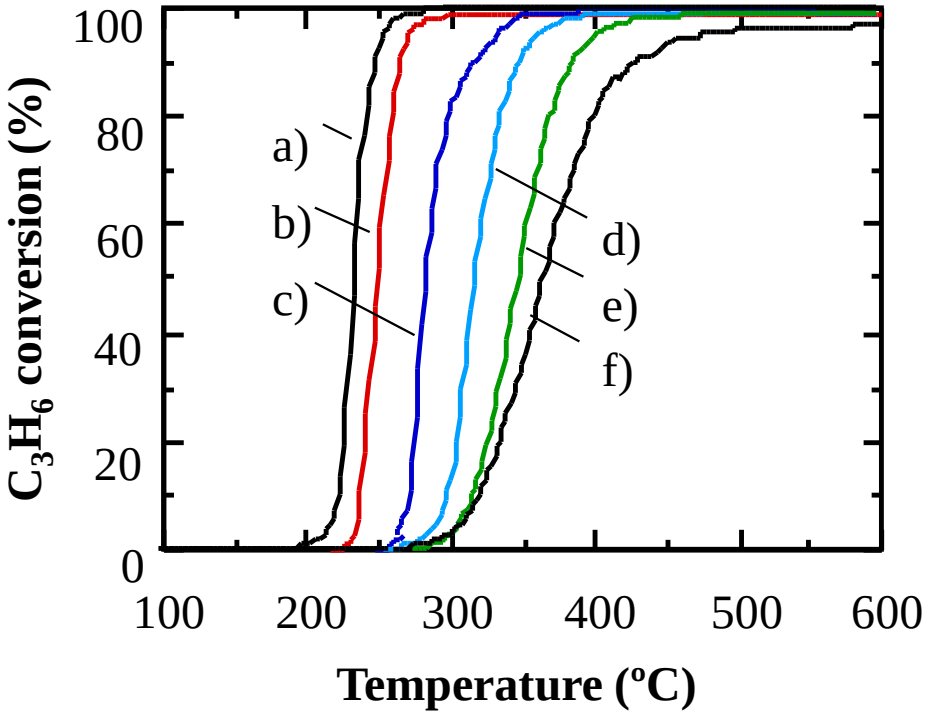
100
80
60
40
20
0
100
200
300
400
500
600
a)
b)
c)
d)
e)
f)
C3H6 conversion (%)
Temperature (°C)

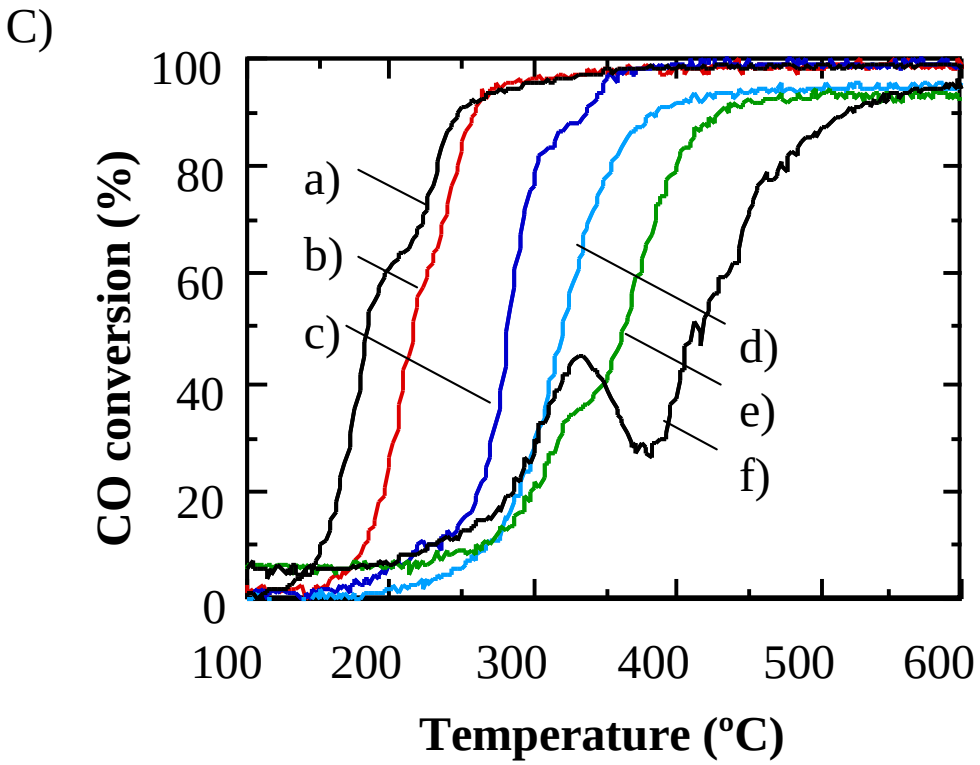

Fig. 1. (A) NO_X conversion efficiency as a function of temperature in simulated oxidizing feed stream. The following catalysts are indicated: (a) PS, (b) PNS, (c) PMS, (d) PMNS1, (e) PMNS2 and (f) PMNS3. (B) C_3H_6 conversion efficiency as a function of temperature in simulated oxidizing feed stream. The following catalysts are indicated: (a) PS, (b) PNS, (c) PMS, (d) PMNS1, (e) PMNS2 and (f) PMNS3. (C) CO conversion efficiency as a function of temperature in simulated oxidizing feed stream. The following catalysts are indicated: (a) PS, (b) PNS, (c) PMS, (d) PMNS1, (e) PMNS2 and (f) PMNS3.

3.2. Catalytic activity at nearby stoichiometric point

In Fig. 2(A) - (C), respectively, are shown the conversions of NO_X, C_3H_6 and CO at 450 ˚C on PS, PNS, PMS, PMNS1, PMNS2 and PMNS3 catalysts, when S changes from reducing to oxidizing conditions around stoichiometric point. Reaction temperature was chosen 450 ˚C at which the effect of the addition of Mo and Na appeared. All the catalysts have high conversion activity of NO_X, C_3H_6 and CO when S is nearly equal to 1. These results suggest that all the catalysts have enough ability for three-way activity. The NO_X conversion curves are also classified into three groups described above.

In the first group, PS and PNS catalysts show poor NO_X conversion activity except for around stoichiometric point (S = 1). This is the same characteristic feature as that of the supported Pt catalysts reported previously [22]. It is assumed that NO reduction is inhibited by O_2 and CO [30] adsorbed on Pt under lean and rich conditions, respectively. C_3H_6 conversion under rich conditions increases with increasing the addition of Na. But under lean conditions all the catalysts have high C_3H_6 conversion activity. As for CO conversion curves, the remarkable difference is not recognized among all the catalysts in every group.

In the second group, PMS catalyst has higher NO_X conversion activity than the catalysts of the first group. As shown in Fig. 2(A), the addition of Mo has an effect of enhancing the NO_X reduction activity under lean and rich conditions compared with PS and PNS catalysts. Gandhi et al. [22], and Shelf and coworkers [23, 24] have already described similar results that Mo in $PtMo/Al_2O_3$ and $PdMo/Al_2O_3$ catalysts improved NO_X reduction under slight lean conditions compared with Pt/Al_2O_3 and Pd/Al_2O_3 catalysts. Further, it proves that PMS catalyst has higher C_3H_6 conversion activity under rich conditions compared with PS catalyst, which indicates that Mo on Pt catalyst has also an effect of enhancing C_3H_6 oxidation.

In the third group, the $PtMoNa/SiO_2$ catalysts show much higher conversion in S

> 1, compared with the catalysts without Mo or Na in the first and second groups. As shown in Fig. 2(A), the conversion of NO_X on PtMoNa/SiO_2 catalysts under rich, lean and stoichiometric conditions increase with increasing the addition of Na. When 1 wt% Na_2O (PMNS3 catalyst) is added, the conversion of NO_X showed over 90 % in 0.36 < S< 2.45. This result indicates that Na and Mo on Pt catalyst improve the conversion of NO_X more significantly than Mo on Pt catalyst. The conversion of C_3H_6 under rich conditions is highest among all the catalysts when 0.1 wt% Na_2O is added. The conversion of C_3H_6 on PMNS3 catalyst is lower than that on PMNS1, PMNS2 and other catalysts under lean conditions (S > 1). The conversions of CO on PMNS2 and PMNS3 catalysts are lower than that on PMNS1 and other catalysts under lean conditions because of the formation of CO which is a product of incomplete oxidation of C_3H_6. It is suggested that the addition of Mo and Na to Pt catalysts has an effect of expanding the active S window in which three-way activity occurs, in particular, the window of the conversion of NO_X. This result would not be brought in by the temperature shift of light-off temperature on which the addition of Mo and Na affects.

In Fig. 3 is shown the conversion of NO_X on PS and PMNS2 catalysts as a function of redox ratio, S, in simulated exhaust for S-scan at 300 ˚C and 400 ˚C. As shown in Fig. 3, the conversion of NO_X on PS at 300 ˚C (~ 29 %) is higher than that at 400 ˚C (~ 18 %) under lean conditions (S = 2.45), while that at 300 ˚C (~ 8 %) is considerably lower than that at 400 ˚C (~ 83 %) at the stoichiometric point (S = 1). On the other hand, the conversion of NO_X on PMNS2 catalyst at 400 ˚C is considerably higher than that at 300 ˚C under rich, lean and stoichiometric conditions (0.36 < S < 2.45). These results show that the conversion of NO_X on Pt catalyst keeps high in the range of wide redox ratio by the addition of Mo and Na to Pt catalyst.

The MS and NS catalysts had not only activity of NO_X reduction but also that of HC and CO oxidation when S changes gradually from reducing to oxidizing conditions around stoichiometric point at 450 ˚C.

A)

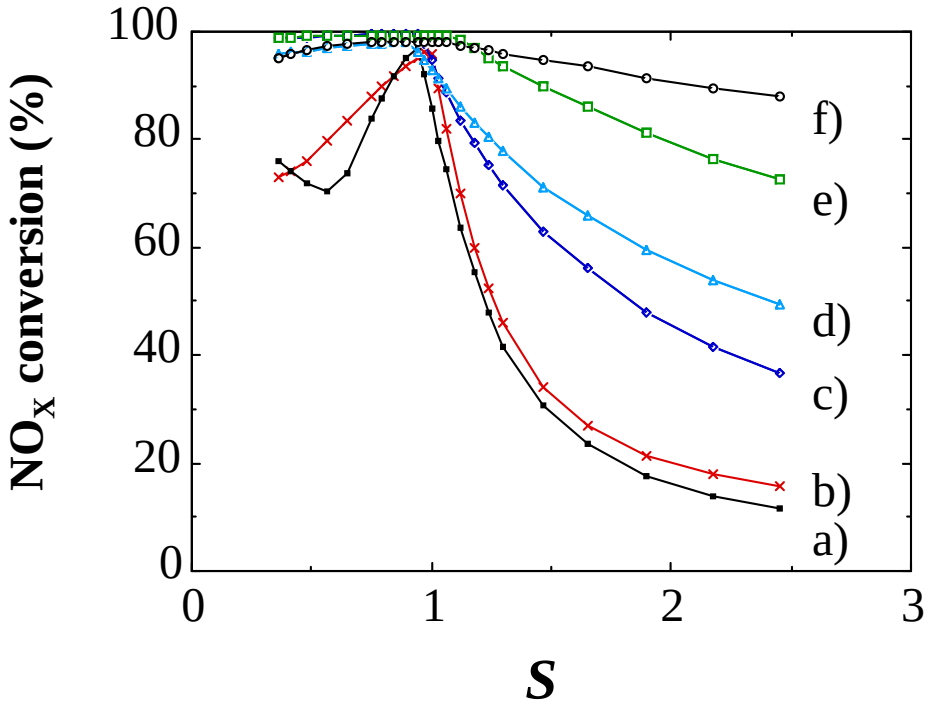
100
80
60
40
20
0
0
1
2
3
NO_X conversion (%)
S
f)
e)
d)
c)
b)
a)

B)

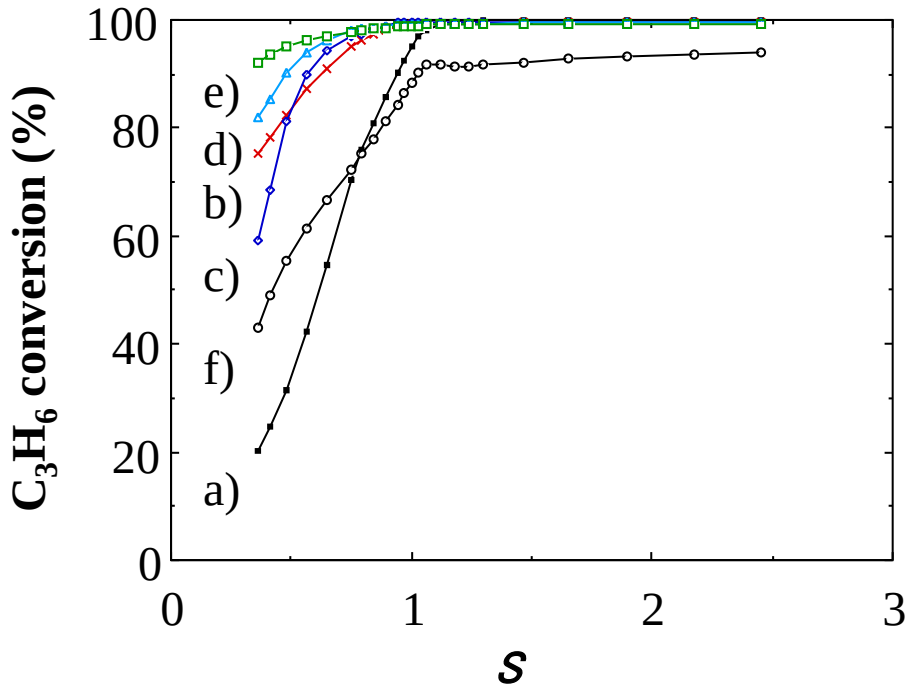
100
80
60
40
20
0
0
1
2
3
C_3H_6 conversion (%)
S
e)
d)
b)
c)
f)
a)

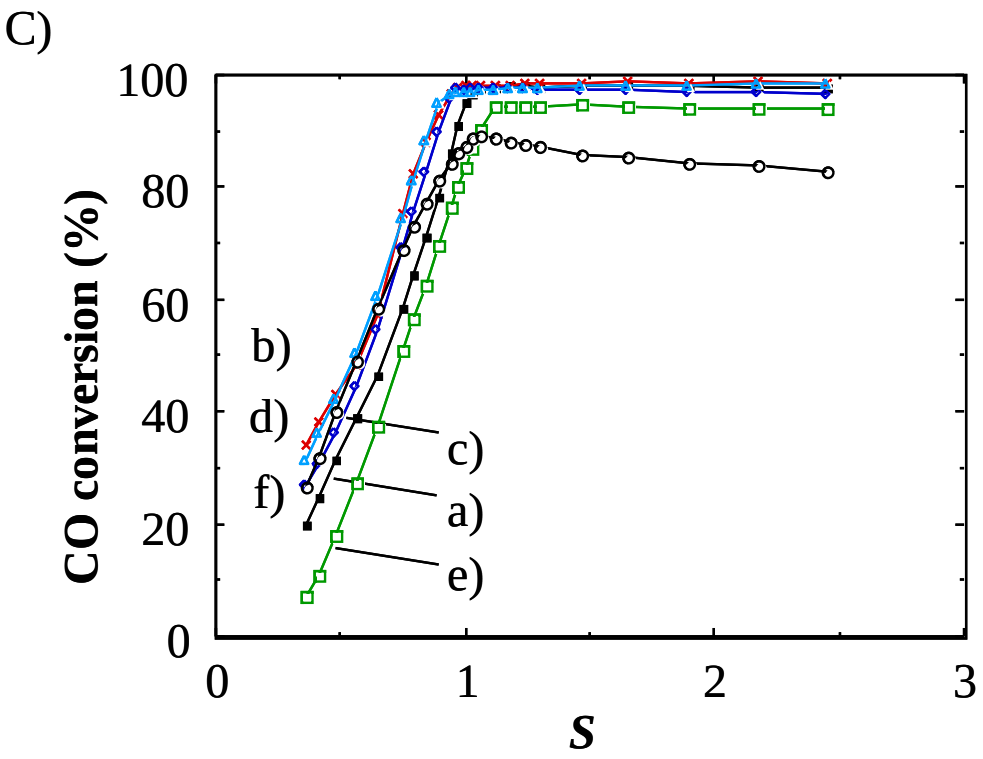

Fig. 2. (A) NO_X conversion efficiency as a function of redox ratio in simulated exhaust for S-scan at 450 ˚C. The following catalysts are indicated: (a) PS, (b) PNS, (c) PMS, (d) PMNS1, (e) PMNS2 and (f) PMNS3. (B) C_3H_6 conversion efficiency as a function of redox ratio in simulated exhaust for S-scan at 450 ˚C. The following catalysts are indicated: (a) PS, (b) PNS, (c) PMS, (d) PMNS1, (e) PMNS2 and (f) PMNS3. (C) CO conversion efficiency as a function of redox ratio in simulated exhaust for S-scan at 450 ˚C. The following catalysts are indicated: (a) PS, (b) PNS, (c) PMS, (d) PMNS1, (e) PMNS2 and (f) PMNS3.

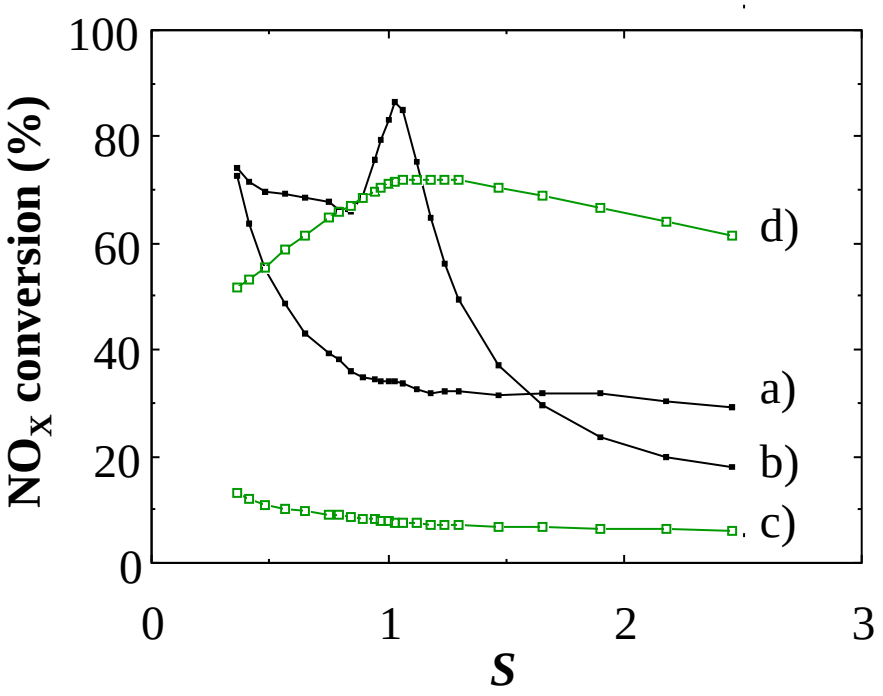

Fig. 3. NO_X conversion efficiency as a function of redox ratio in simulated exhaust for S-scan. The following catalysts and reaction temperatures are indicated: (a) PS at 300 ˚C, (b) PS at 400 ˚C, (c) PMNS2 at 300 ˚C and (d) PMNS2 at 400 ˚C.

3.3. Selectivity of NO

NO selectivity, for the selective reduction of NO_X in the presence of excess oxygen, is given by the expression shown in Scheme 2. Fig. 4 shows NO selectivity in the model gas reaction at 450 ˚C when S changes from 0.36 to 9.91.

In Fig. 4, no symbolic line indicates the partial pressure ratio of NO in inletted NO and O_2 gases. In $S < 1$, NO selectivity of both PS and PMNS3 is nearly same as the partial pressure ratio of NO in inletted NO and O_2 gases. This result indicates that NO works as oxidant as equally as oxygen in $S < 1$. In $S > 1$, NO selectivity of PS is less than the partial pressure ratio of NO. While NO selectivity of PMNS3 catalyst is higher than the partial

pressure ratio of NO in S > 1. In this way, PMNS3 catalyst has the feature that the reaction in which oxygen participates is inhibited by the excess oxygen, so that the reaction in which NO participates as oxidant proceeds preferentially. The effect of the inhibition of the reaction induced by O_2 is assumed to lead to the widening of S window of NO_X reduction activity around stoichiometric point and the enhancement of NO_X reduction activity under lean conditions.

$$NO\ selectivity = \frac{\text{NO consumption}}{\text{NO consumption} + O_2\ \text{consumption}} \times 100\ (\%)$$

-Scheme 2

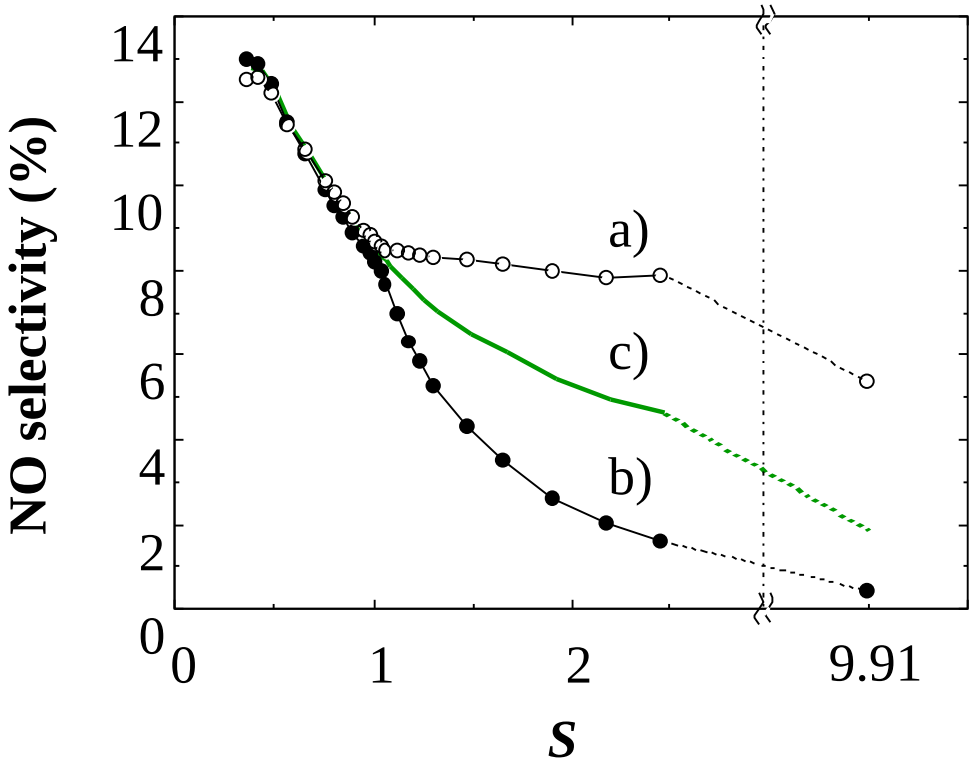

Fig. 4. NO selectivity for NO reduction as a function of redox ratio in simulated exhaust for S-scan at 600 ˚C. The following catalysts are indicated: (a) PMN3 and (b) PS. (c) indicates NO fraction of inlet the NO + O_2 gases.

3.4. Characterization of catalysts

We examined the oxidation state of Pt by IR study using CO as probe molecule. Table 2 shows the wave numbers of stretching vibration of CO adsorbed on Pt, ν (CO_{ads}), when the catalysts were pretreated in flowing 7 % O_2/N_2, 100 % N_2 and 7 % H_2/N_2, respectively, before IR measurement. In the measurement of Mo containing catalysts after H_2 pretreatment the intensity of diffuse reflectance IR was too weak to decide the position of wave numbers of ν (CO_{ads}). As for PS catalyst, the positive shift of wave numbers of ν (CO_{ads}) is large in the order of flow of 7 % O_2/N_2, 100 % N_2 and 7 % H_2/N_2.

Table 2. The wavenumbers of ν(COads)

Catalyst	wavenumbers (cm^{-1})		
	pretreatment (a balance of N_2)		
	O_2	N_2	H_2
PS	2087	2079	2074
PMS	2081	2078	-
PMNS2	2080	2075	-
PMNS3	2079	2075	-

These results indicate that Pt exists in high oxidation state under oxidizing conditions and exists in low oxidation state under reducing conditions. On the other hand, PMS, PMNS2 and PMNS3 catalysts have the negative shift compared with PS catalyst. The difference of wave numbers of ν (CO_{ads}) on $PtMoNa/SiO_2$ between after N_2 pretreatment and after O_2 pretreatment was less than that on PS catalyst, and wave numbers of ν (CO_{ads}) which is obtained on PMS, PMNS2 and PMNS3 catalysts after O_2 pretreatment is similar to that on

PS catalyst after N_2 pretreatment. These results suggest that the electron density of the Pt atoms of $PtMoNa/SiO_2$ is kept at high level even under oxidizing conditions, and that Pt is inhibited to be oxidized.

Fig. 5 shows the relation between the wave numbers of ν (CO_{ads}) after O_2 pretreatment and the conversion of NO_X at 450 ˚C. When S is 2.45 and 9.91, the conversion of NO_X at 450 ˚C becomes higher as the wave numbers of ν (CO_{ads}) becomes lower. It is derived from this result that inhibiting the oxidation of Pt on the catalysts belonging to the third group caused the increasing of NO_X reduction activity.

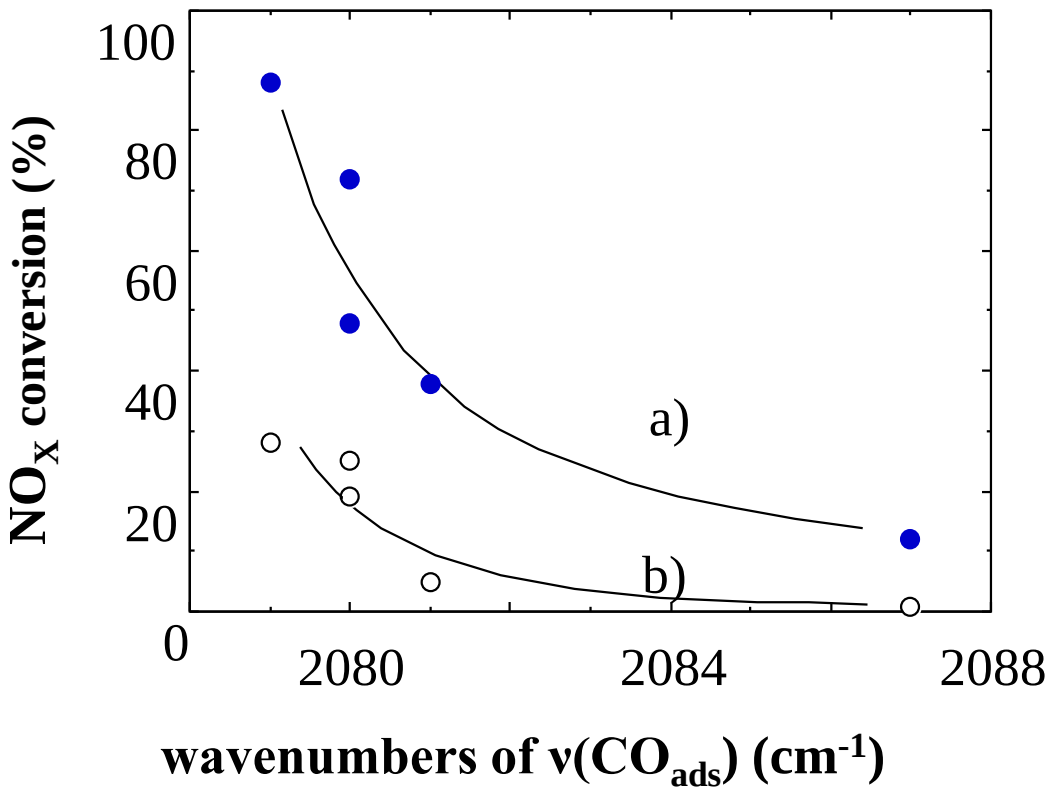

Fig. 5. The relation between the wave numbers of ν(COads) after O_2 pretreatment and NO_X conversion at 450 ˚C. The following redox ratio, S, are indicated: (a) 2.45 (simulated A/F = 15.2) and (b) 9.91 (simulated A/F = 18).

The study of the oxidation state of Pt by XPS leads to the same conclusion as mentioned above. Fig. 6 shows the XPS spectra in the region of the Pt $4f_{7/2}$ emission band of Mo containing catalyst such as PMS, PMNS2 and PMNS3 catalysts after O_2 pretreatment. The addition of Na causes the negative shift of the Pt $4f_{7/2}$ binding energy for $PtMoNa/SiO_2$ catalysts. XPS spectra measured under oxidizing conditions also clarifies that Pt on PMNS2 and PMNS3 catalysts are difficult to be oxidized even under considerable O_2 rich conditions and the oxidation state of Pt becomes lower with increasing Na content.

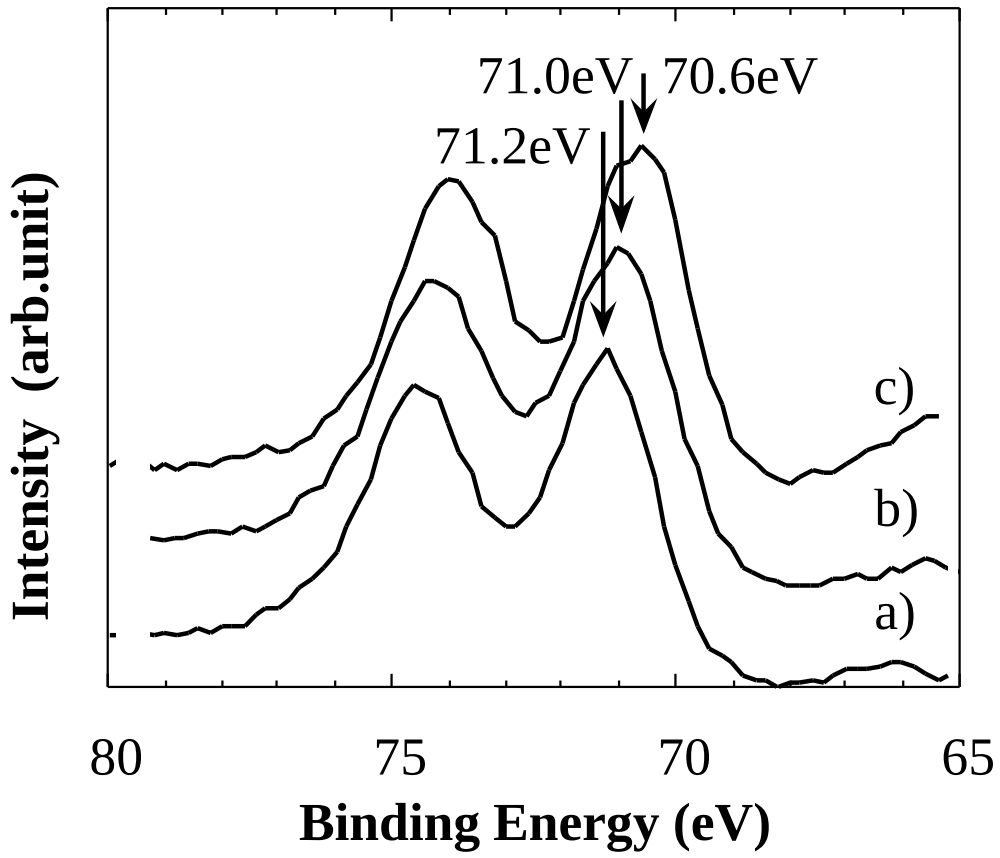

Fig. 6. XPS spectra of Pt 4f after O_2 pretreatment (1×10^{-7} torr O_2, 1 h). The following catalysts are indicated: (a) PMS, (b) PMNS2 and (c) PMNS3.

Table 3 shows the amount of CO adsorbed on catalysts under reducing conditions. As for PS and PNS catalysts, the amount of CO adsorbed on the catalyst is relatively large. This result indicates that large amount of Pt exists on the surface of the catalyst. On the other hand, the catalysts including only Mo lose their ability to chemisorb CO and the CO-to-Pt ratio (CO/Pt) becomes lower with increasing Na content. While XRD patterns show no crystalline Pt on the PtMoNa/SiO_2 catalysts in the third group. These results are in agreement with the model that Tri et al. [25] has already reported. As they have pointed out, it seems reasonable to suppose that there exists physically masking around Pt atoms by the Mo atoms deposited on the surface of the Pt atoms under reducing conditions. In addition, EXAFS and XPS analysis of PtMo/SiO_2 catalysts reported by Liu et al. [27] also support this model. In our case, as Na is added to PtMo/SiO_2 catalyst, probably, Na must assist Mo masking more widely around Pt atoms. Such assumption is supported by the decrease in the amount of adsorbed CO.

Table 3 . Amounts of CO adsorbed on catalysts

Catalyst	adsorbed CO mmol/g-cat	CO/Pt ratio %
PS	32.8	38.4
PNS	29.0	33.9
PMS	1.9	2.2
PMNS1	1.5	1.7
PMNS2	0.6	0.7
PMNS3	0.3	0.4

3.5. The possible reason for the change of catalytic performance in PtMoNa/SiO_2

Only Mo supported catalyst and only Na supported catalyst had not only activity of NO_X reduction but also that of C_3H_6 and CO oxidation under the reaction conditions in this paper. Therefore, the active center of PtMoNa/SiO_2 is Pt, which determines the catalytic performance of NO_X reduction. The effect of the addition of Mo and Na is estimated to change the reaction characteristics of the Pt.

From IR spectra of adsorbed CO and XPS spectra, it is demonstrated that the oxidation state of Pt on PtMoNa/SiO_2 catalysts is lower than that on PS catalyst, that Na content strongly affects the oxidation state of Pt on PtMoNa/SiO_2 catalysts, and that the oxidation state of Pt has a correlation with NO_X reduction activity. Further, the estimation of NO selectivity reveals that PtMoNa/SiO_2 catalysts has the feature that the reaction in which oxygen participates was inhibited in the presence of excess oxygen.

These results described above is possible to explain by the assumption that the oxidation of Pt corresponds to the activation of O_2 which leads to the oxidation of NO and reductants such as C_3H_6, CO and H_2. It is assumed that the adsorption or the dissociation of O_2 brings about oxidizing of Pt and that O_2 becomes an activated state for oxidation reaction through the adsorption and dissociation. In general, the dissociation rate of adsorbed O_2 is faster than that of adsorbed NO on Pt surface [31], so that NO is a weaker oxidant than O_2 on Pt surface and NO exerts rather as reductant and reacts with O_2 to produce NO_2 in the presence of excess oxygen. However, the addition of Mo and Na changes the characteristic of Pt under the conditions that oxygen sufficiently works as an oxidant, so that the activation of O_2 is inhibited and NO is easily reduced. The reason for this is assumed to lower the affinity between Pt and oxygen caused by the addition of Mo and Na.

From such structural information on PtMoNa/SiO_2 catalysts, it is concluded that there exists physically masking by Mo and Na around Pt, as mentioned before. Cáseres et

al. [32] have reported that MoO_3 exists poorly dispersed and has the high reducibility on a SiO_2 support compared with other supports.

We have clarified that the effect of the addition of Mo and Na to Pt catalyst was recognized significantly on SiO_2 support as described previously [28]. Perhaps, on SiO_2 support, MoO_3, which has high reducibility, interacts physically or chemically with Pt and the interaction assisted by the addition of Na affected the electron density of Pt atoms. As described above, Pt atoms on the PtMoNa/SiO_2 catalysts are kept at high electron density even under excess oxygen conditions and accordingly resists to be oxidized. Under such environmental conditions, Pt atoms are assumed to be the active component of the characteristic NO_X selective reduction as described above.

4. Conclusions

This paper has described the effects of the addition of Mo and Na to Pt/SiO_2 catalysts such as PtMoNa/SiO_2, compared with PtMo/SiO_2, PtNa/SiO_2 and Pt/SiO_2 catalysts. From above results, we found that PtMoNa/SiO_2 catalysts have different characteristics from conventional Pt catalyst such as Pt/SiO_2 catalyst or some points as described below.

1. Under lean static conditions, temperature window of NO_X reduction of the PtMoNa/SiO_2 catalysts is wider than that of the Pt/SiO_2 catalyst.

2. Under nearly stoichiometric condition, the PtMoNa/SiO_2 catalysts had wide redox ratio windows of NO_X reduction compared with the Pt/SiO_2 catalyst.

3. The PtMoNa/SiO_2 catalysts have the reaction feature that NO is used selectively as oxidant in oxidizing conditions.

4. It is assumed that the interaction of Mo and Na with Pt lowers the affinity between Pt

and oxygen, and results in the reaction characteristics of the PtMoNa/SiO_2 catalysts.

References

[1] M. Iwamoto, H. Yahiro, Y. Yu-u, S. Shundo, N. Mizuno, *Shokubai (Catalyst)* 32 (1990) 430.

[2] Y. Fujitani, H. Muraki, S. Kondo, M. Fukui, Jpn. Patent Publ. (Kouhou) 63-100919.

[3] W. Held, A. Konig, T. Richter, L. Puppe, *SAE Technical Paper Series,* SAE 900 496 (1990).

[4] S. Sato, Y. Yu-u, H. Yahiro, N. Mizuno, M. Iwamoto, *Appl.Catal.* 70 (1991) L1.

[5] G. Zhang, T. Yamazaki, H. Kawakami, T. Suzuki, *Appl.Catal. B* 1 (1992) L15.

[6] A. Obuchi, A. Ohi, M. Nakamura, A. Ogata, K. Mizuno, H. Ohuchi, *Appl. Catal. B* 2 (1993) 71.

[7] R. Burch, P. J. Millington, A. P. Walker, *Appl. Catal. B* 4 (1994) 65.

[8] R. Burch, T. C. Watling, *Catal. Lett.* 37 (1996) 51.

[9] T. Tanaka, T. Okuhara, M. Misono, *Appl. Catal. B* 4 (1994) L1.

[10] G. R. Bamwenda, A. Ogata, A. Obuchi, J. Ohi, K. Mizuno, J. Skrzypek, *Appl. Catal. B* 6 (1994) 311.

[11] P. Reyes, M. Oportus, G. Pecchi, R. Fréy, B. Moraweck, *Catal. Lett.* 37 (1996) 193.

[12] B. H. Engler, J. Leyler, E. S. Lox, K. Ostgathe, *SAE Technical Paper Series,* SAE 930 735 (1993).

[13] E. Echigoya, *J. Jpn. Petrol. Inst.* 23 (1980) 223.

[14] J. H. Jones, T. K. Kummer, K. Otto, M. Shelef, W. Weaver, *Environ. Sci. Tech.* 5 (1971) 790.

[15] K. Yokota, H. Muraki, Y. Fujitani, *SAE Technical Paper Series,* SAE 850 129 (1985).

[16] N. Takahashi, H. Shinjoh, T. Iijima, T. Suzuki, K. Yamazaki, K. Yokota, H. Suzuki, N. Mitoshi, S. Matsumoto, T. Tanizawa, T. Tanaka, S. Tateishi, K. Kasahara, *Catal. Today* 27 (1996) 63.

[17] N. Miyoshi, S. Matsumoto, K. Katoh, T. Tanaka, J. Harada, N. Takahashi, K. Yokota, M. Sugiura, K. Kasahara, *SAE Technical Paper Series*, SAE 950 809 (1995).

[18] Y. I. Yermakov, M. S. Ioffe, B. N. Kuznetsov, Y. A. Ryndin, *Kinet. Katal.* 16 (1975) 816.

[19] Y. I. Yermakov, B. N. Kuznetsov, Y. A. Ryndin, *Kinet. Katal.* 42 (1976) 73.

[20] T. M. Tri, J. Massardier, P. Gallezot, B. Imelik, *J. Catal.* 85 (1984) 244.

[21] Y. I. Yermakov, B. N. Kuznetsov, Y. A. Ryndin, Kinet. *Katal. Lett.* 2 (1975) 151.

[22] H. S. Gandhi, H. C. Yao, H. K. Stepien, in: A. T. Bell, L. Hegedus (Eds.), CS Symposium Series No.178 (Catalysis Under Transient).

[23] I. Halasz, A. Brenner, M. Shelef, *Appl. Catal. B* 2 (1993) 131.

[24] T. E. Hoost, G. W. Graham, M. Shelef, O. Alexeev, B. C. Gates, *Catal. Lett.* 38 (1996) 57.

[25] T. M. Tri, J. P. Candy, P. Gallezot, J. Massardier, M. Primet, J. C. Védrine, B. Imelik, *J. Catal.* 79 (1983) 396.

[26] J. E. DeVries, H. C. Yao, R. J. Baird, H. S. Gandhi, *J. Catal.* 84 (1983) 8.

[27] T. Liu, K. Asakura, U. Lee, Y. Matsui, Y. Iwasawa, *J. Catal.* 135 (1992) 367.

[28] T. Tanaka, K. Yokota, H. Doi, M. Sugiura, *Chem. Lett.* 5 (1997) 409.

[29] H. Muraki, H. Shinjoh, H. Sobukawa, K. Yokota, Y. Fujitani, *Ind. Eng. Chem. Prod. Res. Dev.* 25 (1986) 202-208.

[30] M. Shelef, *Catal. Rev.* 11 (1975) 1.

[31] H. G. Litz, *Surf. Sci.* 108 (1981) L486.

[32] C. V. Cáceres, J. L. G. Fierro, J. Lázaro, A. L. Agudo, J. Soria, *J. Catal.* 122 (1990) 113.

Part 2

Improvement of NO_X storage and reduction catalyst

Chapter 5

Improvement in sulfur desorption of NO_X storage and reduction catalysts using a Ba-Ti composite oxide.

Abstract

A Ba-Ti composite oxide was formed on a NO_X storage and reduction catalyst via impregnation of a Ba-Ti precursor solution composed of H_2O_2 added to a complex prepared using the citric acid method. The structure of the Ba-Ti composite in solution was analyzed by chemical composition analysis and FT-Raman and UV-vis spectroscopy. MM2 calculations were performed to propose its chemical structure. Both Ba and Ti together were found to form a composite molecule in the solution. Furthermore, TEM-EDX and XRD analyses of the Ba-Ti composite oxide on the catalyst prepared by impregnation with the Ba-Ti composite aqueous solution revealed that Ba and Ti in the catalyst were highly dispersed at the nm scale. The formation of the Ba-Ti composite oxide on the NSR catalyst enhanced sulfur desorption efficiency and led to high-performance NO_X conversion as a NO_X storage and reduction activity catalyst after desulfation treatment. It was assumed that the existence of nano-scaled Ba compounds combined with Ti was efficient for the inhibition of the sintering of barium sulfate and its facile decomposition. It was found that dispersion of Ba compounds for NO_X storage materials using a Ba-Ti complex solution is an efficient way to improve the durability of NSR catalysts.

1. Introduction

Curbing CO_2 emissions and improving the fuel efficiency and clean-up of automobile exhaust gases are required for global environmental protection. Lean-burning gasoline and diesel engines achieve high fuel economy using higher air/fuel ratios (A/F). It is difficult, however, to remove the NO_X in exhaust gases from these engines under excess oxygen conditions. Some NO_X purifying systems such as selective NO_X reduction by hydrocarbons [1 - 3], NH_3 (urea) [4], H_2 [5] and CO [6] have been researched, with a few of them developed for commercial use.

A NO_X storage and reduction (NSR) catalyst system is one of the most efficient ways to achieve NO_X purification [7, 8]. In the NSR system, NO_X (NO) is oxidized to NO_2 over precious metals in the catalyst, then combined with NO_X storage materials and finally stored as nitrate ions. In the following reduction stage, under a stoichiometric or reductive atmosphere (rich), the stored nitrate ions are released as NO_X (NO or NO_2) from the NO_X storage materials and then reduced to nitrogen. The NSR catalyst system has the advantages of high performance and feasibility for purifying NO_X compared with other methods.

Unfortunately, NSR catalysts deactivate due to sulfur poisoning and/or thermal deterioration. Sulfur deactivation in particular is the most important problem to be solved. The sulfur poisons the precious metals [9, 10], supports [11] and NO_X storage materials [8, 9]. Furthermore, sulfur poisoning strongly influences the NO_X storage ability of the system. NSR catalysts include some alkali metals or alkali earth metals that produce stable sulfates (SO_X) when exposed to exhaust gases. It has been confirmed that the adsorbed sulfur transforms the NO_X storage materials into sulfates [8 - 10]. The formation of nitrate on the storage compound is inhibited and thus the NO_X storage ability deteriorates. Consequently, the deactivation of NSR catalysts depends on the amount of sulfur poisoning of the catalyst [12]. Sulfur deactivation also depends on the particle size of the sulfate produced by the

NSR catalyst [13]. It has been reported that the decomposition temperature of sulfates decreases if the $BaSO_4$ particles in the catalyst are kept under 3 nm in size [14].

There have been several reports about improving the sulfur tolerance of NSR catalysts based on the above research. One of the methods involved the usage of TiO_2 [15]. The decomposition temperature of sulfates on a TiO_2 support was found to be lower than that on an Al_2O_3 support under reducing conditions. By blending TiO_2 with Al_2O_3 [16], sulfur deposition was simultaneously suppressed and enhanced the NO_X storage of the sulfur-aged catalyst. The tolerance of the NSR catalyst against sulfur poisoning was successfully improved by the use of fine TiO_2 particles [17 - 20]. The decomposition temperature of titanium sulfate is known to be 150 ˚C in the static condition, and is considerably lower than that of aluminum sulfate (770 ˚C) and cerium sulfate (900 ˚C) [21]. Although this decomposition temperature changes including reducing gases such as H_2, titanium sulfate that forms under exhaust gases including SO_X is assumed to be decomposed easily and release SO_X more readily compared with other oxides.

In conventional NSR catalysts, some alkali materials such as Ba and K compounds are supported on porous oxide supports such as Al_2O_3. The co-existence of both Ba and K is effective for expanding the active temperature range. The NO_X storage amount for the K containing NSR catalyst is higher than that of the Ba containing catalyst at high temperatures (over 450 ˚C) and lower at low temperatures (under 450 ˚C). For this reason, both Ba and K are used [22]. While the utilization of Ba compounds for the NSR catalyst is very important for NO_X storage performance, it also inhibits sulfur deterioration. Ba sulfate is more stable than other alkali sulfates [16], and thus more sulfur residue exists after desorption treatment on the Ba compounds in an NSR catalyst compared to the K compounds. Accordingly, desulfation of Ba containing NSR catalysts is the most important subject to address in order to prepare highly durable NSR catalyst systems.

Based on the above information, we felt that the most effective way to realize improvement of sulfur desorption from NSR catalysts would be to make highly

homogeneous fine particles of Ba and Ti compounds on a high surface area support such as Al_2O_3. One of the most simple and effective methods for achieving this aim is to disperse a composite aqueous complex solution including both Ba and Ti on the high surface area support. Citrate complexation is an efficient precursor method for producing fine and homogenous Ba-Ti composite oxides such as perovskite type $BaTiO_3$ [23 - 25]. In this method, however, the complex in solution tends to polymerize and produce a precipitate, which makes it difficult to use for impregnation on support oxides. However, we found that the addition of H_2O_2 is effective for keeping the solution stable [26]. In this study, we prepared NSR catalysts using a Ba-Ti composite oxide dispersed on the support surface and examined their structures and catalytic performance.

2. Experimental

2.1. Catalyst preparation

2.1.1. Preparation of Ba-Ti composite solution

The preparation method is described as follows. Citric acid was first dissolved in water at 75 ˚C followed by addition of $Ti(i\text{-}PrO)_4$ (Wako Co.) with continuous stirring. After stirring at 75 ˚C for 5 h, the solution transformed to a light yellowish transparent state without any precipitates. The solution was then cooled at room temperature and 30 % aqueous H_2O_2 solution (Wako Co.) was added, resulting in a change of color from light yellow to red. Finally, aqueous $Ba(CH_3COO)_2$ (Wako Co.) was added to the transparent red solution to obtain the Ba-Ti composite solution as the precursor of the Ba-Ti composite adsorbent. We found that addition of H_2O_2 inhibited precipitation,

making the Ba-Ti precursor solution more stable than when no additives were used. The prepared composite solution was suitable for impregnation on various oxide supports.

2.1.2. Catalyst preparation

Four catalyst formulations, BaTi-A, BaTi-B, Ba-A and Ba-B, as summarized in Table 1, were prepared in this study. Cordierite substrates (cylindrical, φ = 30 mm, L = 50 mm, 400 cells per square inch) were first coated with two types of metal oxides; 1) 7 g γ–Al_2O_3 (170 m^2/g) for characterization and 2) 9.45 g mixed oxides including γ-Al_2O_3, ZrO_2 and TiO_2 for estimation of catalytic activity. The wash coat was deposited by first immersing the substrate in an aqueous slurry of the above oxides. The excess slurry was gently removed by blowing air through the monolith channels. The samples were then dried and subsequently calcined. The coating procedure was repeated until the desired amount of alumina was deposited and the samples were then calcined for 1 h at 500 ˚C in air. Catalysts were prepared by impregnating $Pt(NH_3)_2(NO_2)_2$ and $Rh(NO_3)_3$ (Tanaka Precious Metals) followed by drying at 110 ˚C for 12 h and then calcining at 300 ˚C for 3 h in air. The amount of Pt and Rh loading was 2 and 0.5 g/L, respectively. The monolith obtained was then added to an aqueous solution containing Ba to form the storage material. The BaTi-A and BaTi-B catalysts were prepared using the Ba-Ti composite solution prepared above. The Ba-A and Ba-B catalysts were prepared using $(CH_3COO)_2Ba$. Finally, an aqueous solution containing CH_3COOK and CH_3COOLi (Wako Pure Chemical Industries) was impregnated on the monolithic samples containing Pt and Rh, such as BaTi-B and Ba-B. The loading amounts of Ba, K and Li were 0.2, 0.15 and 0.1 mol/L, respectively. After the catalysts were dried at 110 ˚C for 12 h, they were calcined at 300 ˚C for 3 h in air.

Table 1.
Catalyst formulations

Catalyst	Support	Pt g/L	Rh g/L	Ba mol/L	Ti mol/L	K mol/L	Li mol/L
BaTi-A	γ-Al_2O_3	2	-	0.2	0.2	-	-
BaTi-B	mixed oxides	2	0.5	0.2	0.2	0.15	0.1
Ba-A	γ-Al_2O_3	2	-	0.2	-	-	-
Ba-B	mixed oxides	2	0.5	0.2	-	0.15	0.1

2.2. Characterization of the Ba-Ti composite precursor solution

The structure of the Ba-Ti composite in solution was analyzed by chemical composition analysis and FT-Raman and UV-vis spectroscopy. Chemical composition analysis was performed on the solid obtained by accumulating the red colored fraction separated by silica gel column chromatography using water as a solvent. The content of Ba and Ti were analyzed by ICP (SSI Nano-TEC SPS4000) and the content of C was analyzed by the combustion infrared absorption method (Horiba Co. EMIA810). The chemical structure of the Ba-Ti composite in solution was proposed by performing an optimized geometry calculation in mechanics using CAChe and SCiGRESS software (FUJITSU Limited) with augmented MM2 parameters based on the results of the above analyses.

2.3. Characterization of the catalysts

XRD patterns were recorded using an X-ray diffractometer (Cu Ka radiation λ = 1.5418 Å, 40 kV, 30 mA) (Rigaku, RINT-1500V). Samples of catalyst powders were pressed into wafers and affixed to standard sized microscope slides. The particle size of Pt was calculated using Scherrer's formula.

The ratio of Ti to Ba in the BaTi catalyst powder was analyzed using an energy-dispersive X-ray (EDX) analyzer equipped with a field-emission transmission

electron microscope (Hitachi, HF-2000). The diameter of the EDX analysis area was approximately 10 nm.

2.4. Thermal aging test and sulfur treatment

Thermal aging was performed by exposing the catalysts to 1 L/min of air at 750 ˚C for 5 h. Table 2 shows the composition of the feed streams used to simulate actual engine exhaust gases for the catalytic performance test using a conventional fixed-bed flow reactor (Best Sokki Bex-5900 with a flame photometric detector) at atmospheric pressure and fixed temperature. For the sulfur exposure treatment, catalysts were exposed to the sulfur adsorption gas atmosphere (Table 2), cycling lean (120 sec) and rich (3 sec) for 41 min at 400 ˚C. The total sulfur amount introduced to the catalyst during this treatment was 1.52 g/L-catalyst (47.6 mmol/L-catalyst), which was enough for sulfur deterioration of the NSR catalyst (vide infra). After the sulfur adsorption procedure, the gas composition was switched to the Sulfur desorption atmosphere to measure the sulfur species desorbed from the catalysts. The gas hourly space velocity (GHSV) was 54,000 h^{-1} for both the adsorption and desorption steps.

2.5. Catalytic performance test

To investigate the influence of Ba-Ti composite oxides on the desulfation of the NSR catalysts, the deactivated catalysts were reduced under the sulfur desorption gas indicated in Table 2 at 600 or 650 ˚C for 10 min and subsequently exposed to the NO_X storage measurement gas atmosphere, cycling lean and rich as described above. These procedures were repeated several times. From the measured NO_X concentration, the NO_X conversion and NO_X storage amount were calculated.

Table 2.
Simulated gases composition for the catalytic performance tests

Atmosphere	O_2 %	NO ppm	CO %	H_2 %	THC ppmC	CO_2 %	S ppm	H_2O %
Sulfur adsorption								
lean	6	470	0	0	100	10	30	10
rich	0	470	6	2	50	10	30	10
Sulfur desorption	0	0	0.13	0.09	0	15	0	10
NO_X storage measurement								
lean	6	470	0	0	100	10	0	10
rich	0	470	6	2	50	10	0	10

3. Results and discussion

3.1. Structure of the Ba-Ti precursor

UV-vis, NMR and Raman spectra, chemical analysis and MD calculations were performed in order to propose a structure for the Ba-Ti precursor.

UV-vis spectra of the Ba-Ti precursor solution are shown in Fig. 1. A peak around 380 nm is attributed to a Ti-peroxo complex [27, 28], which indicates production of O_2 following addition of H_2O_2 and then coordination of O_2 to Ti.

The chemical composition of the red part of the solution, separated by using silica gel column chromatography, is presented in Table 3. Both Ba and Ti were included in the separated solution, and the ratio of Ba to Ti was 0.7 to 1.0. It is confirmed that Ba was included by a large amount in the column separation part of a red color part including Ti-peroxo complex. Although it is estimated that about 30 % of Ti has not combined to Ba, this result suggests that there is a high possibility of Ba and Ti-O_2 complexes coexisting in the same molecule.

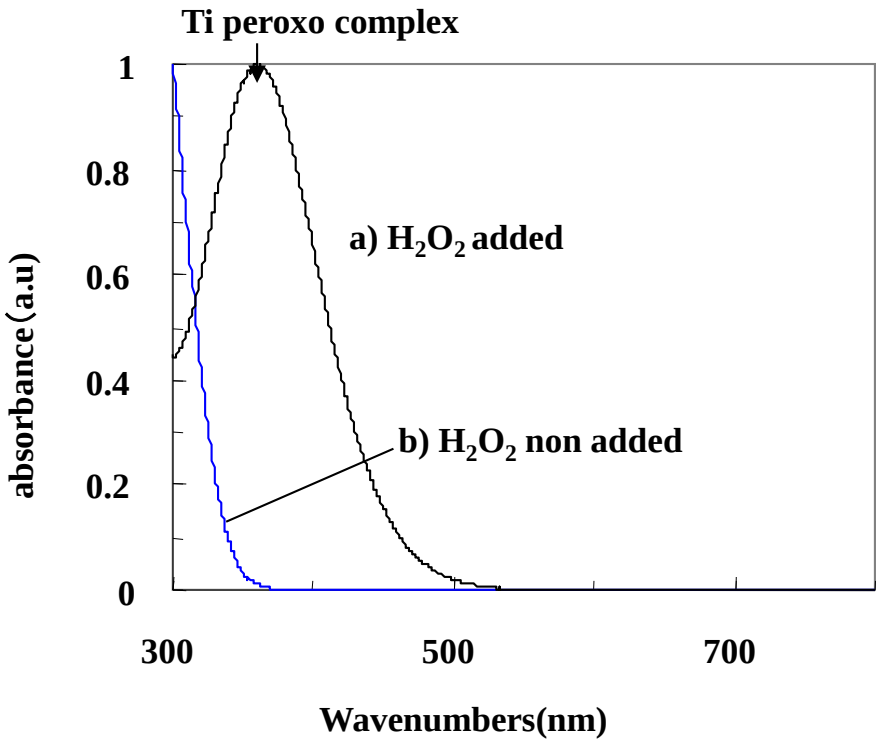

Fig. 1. UV-vis spectra of Ba-Ti precursor solutions.

Table 3.
Composition of the solid after column separation

Element	Average measured weight (%)	Mol ratio
Ba	7.91	0.7
Ti	3.92	1.0
C	34.4	35.0

Raman spectra of the Ba-Ti solution and the ingredients used to prepare it are depicted in Fig. 2. Some characteristic peaks were noted. A peak around 620 cm^{-1} was detected in the Ba-Ti precursor solution (a) and the solution of Ti citric acid and H_2O_2 (b)

but not in the Ti citric acid solution (c), H_2O_2 solution (d) or the $Ba(CH_3COO)_2$ solution (e). The peak was attributed to a Ti-(O_2) bond as reported by Fang [29]. A 900 cm^{-1} peak was also detected in both solutions containing Ti, citric acid and H_2O_2 (a and b). It was attributed to an O-O bond of the Ti-O_2 complex as previously reported [29]. A 370 cm^{-1} peak was detected only for the Ba-Ti precursor solution. We confirmed that this peak increased with increasing concentration of Ba acetate solution and reached a maximum when Ba/Ti = 1. Based on a previous identification by Su [30], we think this peak results from a Ba-O bond in the Ba-Ti precursor solution.

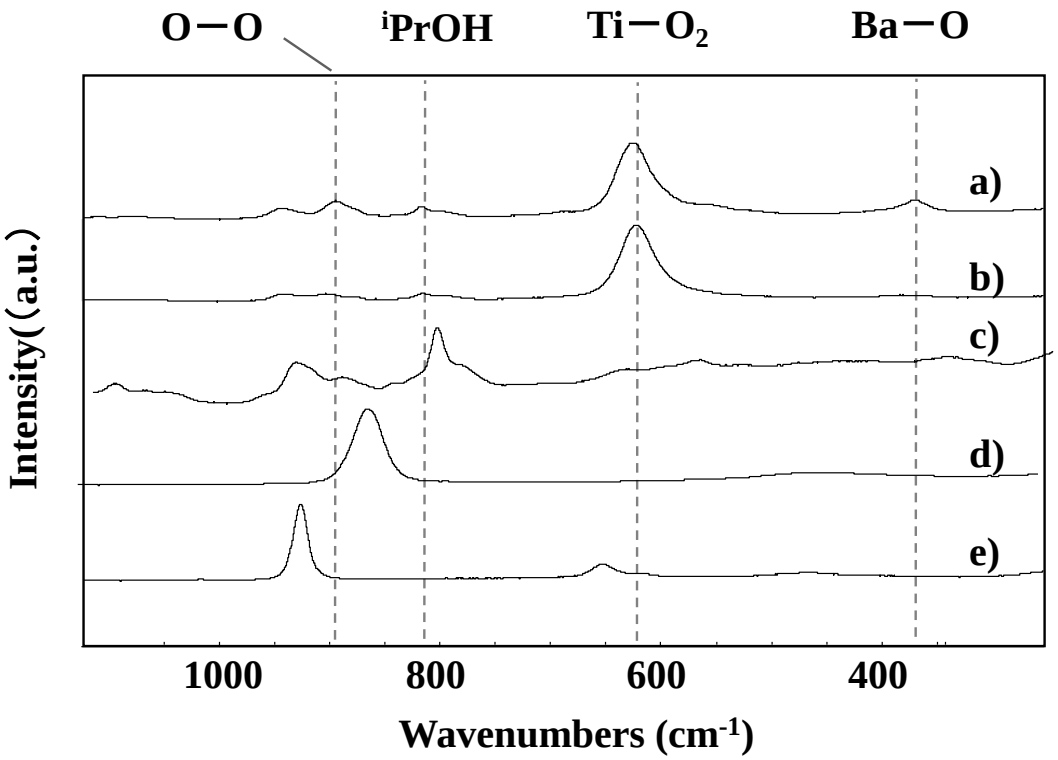

Fig. 2. Raman Spectra of the precursor solutions; a) BaTi precursor solution ($Ba(CH_3COO)_2$ + Ti citric acid + H_2O_2), b) Ti citric acid + H_2O_2 , c) Ti citric acid, d) H_2O_2 and e) $Ba(CH_3COO)_2$.

The XRD patterns of the powders obtained after calcining the precursors in air at 650 ˚C for 3 h are shown in Fig. 3. XRD patterns of the calcined powders showed that the crystallization of the precursor occurred at 650 ˚C and only $BaTiO_3$ perovskite was formed without the presence of other crystalline phases such as $BaCO_3$ and TiO_2. This result means that Ba and Ti exist in a state resulting from their facile combination in the precursor solution.

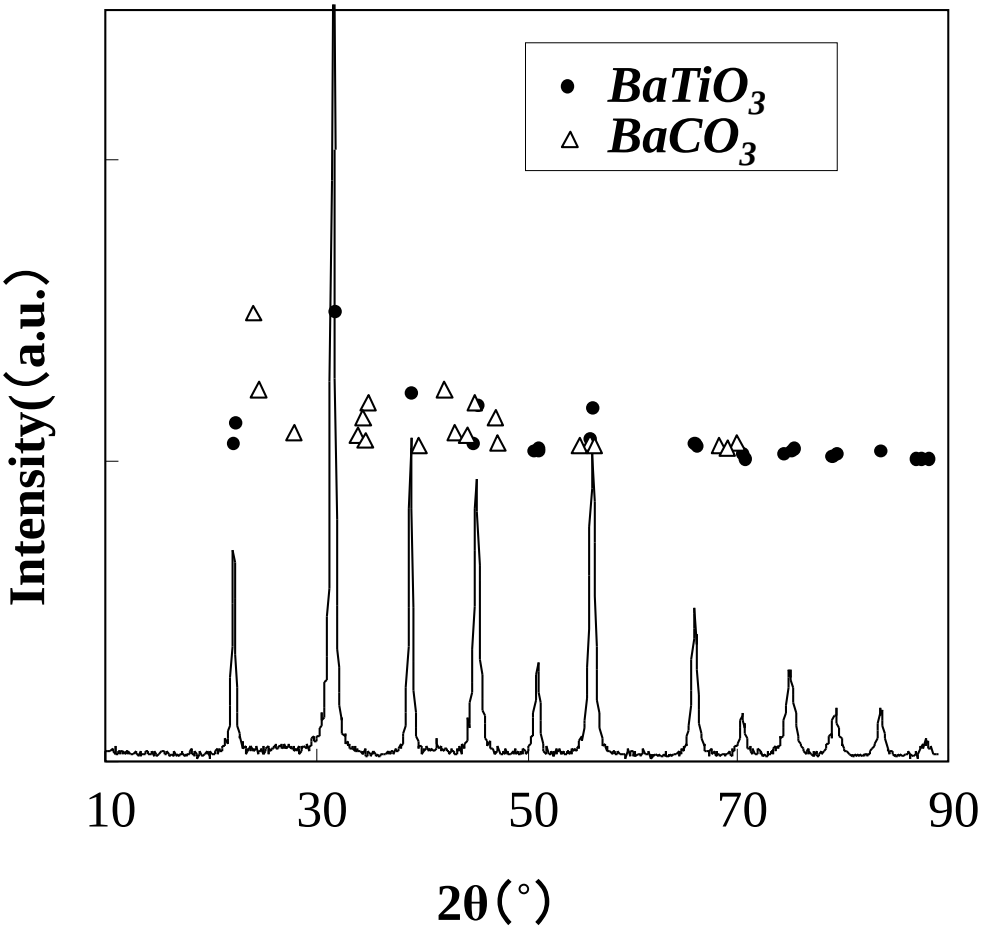

Fig. 3. XRD patterns of Ba-Ti composite oxides obtained after calcination of the precursor solutions at 650 ˚C for 5 h.

MM2 calculations were performed based on the results obtained for the chemical analysis and from the UV-vis and Raman spectra. Firstly, based on Fang's previous report [29], a stabilized cage type structure containing Ba^{2+}, Ti^{4+} and 6 molecules of citric acid was calculated. It was found, however, that one molecule of coordinated citric acid is comparatively unstable and easily displaced by a peroxo ligand in the presence of H_2O_2, forming a more stabilized structure. This estimated stable structure of the complex in the Ba-Ti precursor solution prepared above is shown in Fig. 4. The cage type structure with Ba and Ti surrounded by 5 citric acid molecules can be clearly seen. The improved stability of this prepared Ba-Ti composite structure is likely the reason that this form is preferred.

The analysis of the data described above about the Ba-Ti composite solution supports the idea that both Ba and Ti together form a composite molecule in the solution.

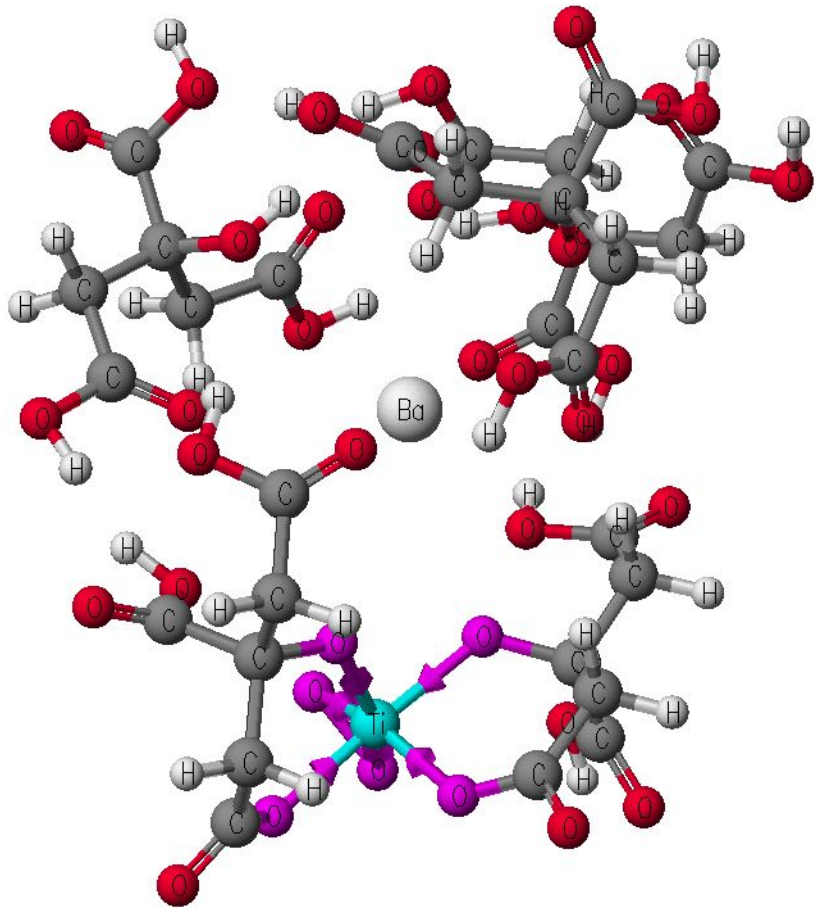

Fig. 4. Estimated structure of the Ba-Ti precursor complex.

3.2. Structure of the Ba-Ti composite oxide with Pt on the support surface

XRD patterns of the BaTi-A and Ba-A catalysts after 500 ˚C calcination are shown in Fig. 5. A diffraction peak at 23.8 ˚, attributed to $BaCO_3$, was recognized for the Ba-A catalyst but not for the BaTi-A catalyst. No other peaks derived from Ba compounds such $BaCO_3$ and $BaTiO_3$ were detected for BaTi-A. This result suggests that the Ba compounds on the BaTi-A catalyst are well dispersed with a fine structure. It is assumed that the bulky caged structure of the Ba-Ti complex speculated above inhibits aggregation of Ba compounds on the calcined catalyst because of the formation of a composite oxide with Ti.

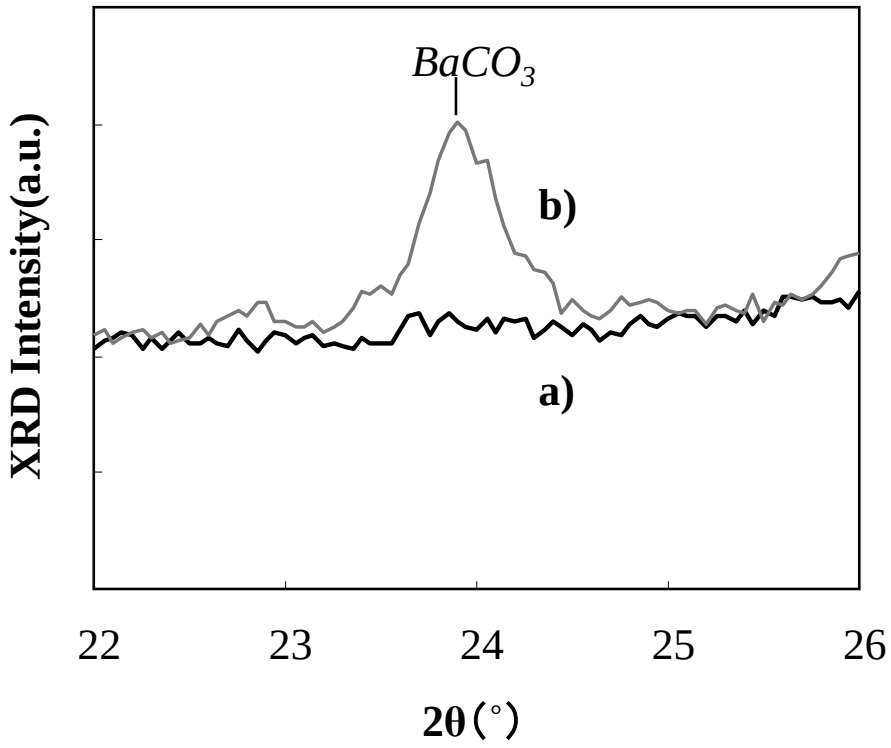

Fig. 5. XRD patterns of fresh catalysts;

a) BaTi-A and b) Ba-A after 500 ˚C calcination.

A TEM image of the BaTi-A catalyst is shown in Fig. 6. Ba and Ti were well dispersed on Al_2O_3 primary particles. No discrete particles such as $BaCO_3$, $BaTiO_3$ or TiO_2 were observed in the BaTi-A catalyst. This result indicates that Ba and Ti are present homogeneously on Al_2O_3. In order to clarify the Ba and Ti concentration on the Al_2O_3 particles, random analysis spots of Al_2O_3 primary particles were examined using EDX. The compositions of two selected spots are listed in Table 4. Ba and Ti were detected in each analysis spot on the nm scale. In this test, the number of surface Ba on BaTi-A or Ba-A is estimated to be 3.5 per nanometer square from Ba loading and a specific surface area of Al_2O_3 support, which corresponds to 62 % or 51 % of the theoretical numbers of $BaCO_3$ or $BaTiO_3$, respectively, on Al_2O_3 for the monolayer coverage. On the BaTi-A catalyst, Ba is presumed to be dispersed as similar to monolayer with no crystallize part.

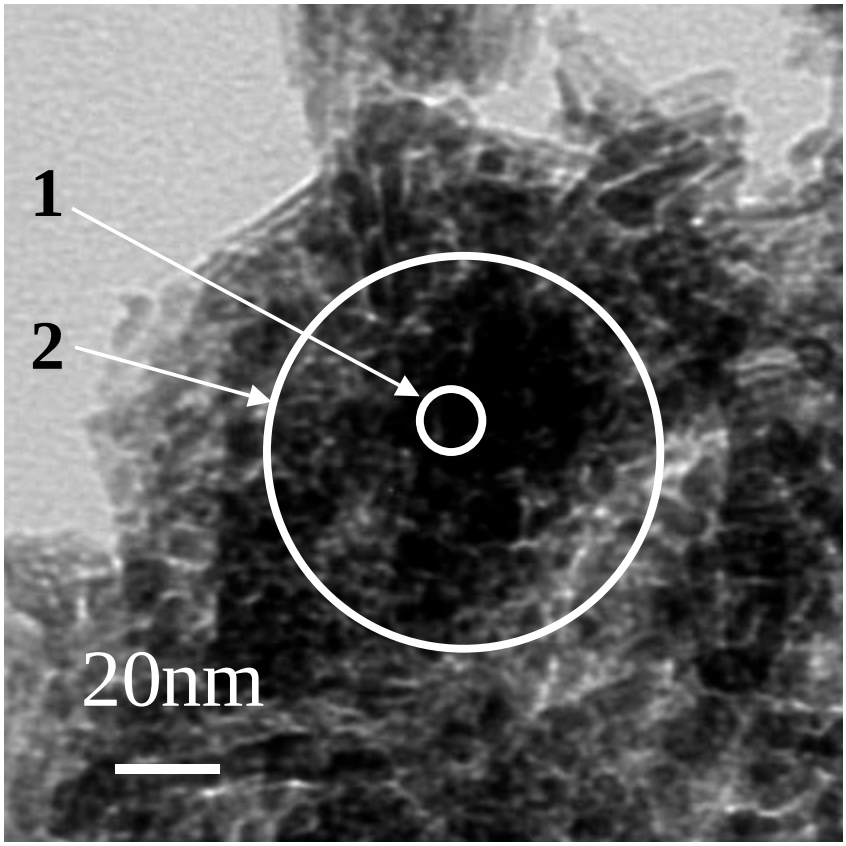

Fig. 6. FE-TEM micrograph of the BaTi-A catalyst after 500 ˚C calcination.

Table 4.
Ba/Ti composition on Al_2O_3 primary particles observed in EDX analysis

area	Al wt%	Ti wt%	Ba wt%
1	90.4	5.8	3.8
2	85.4	7.1	7.3

Therefore, the surface of the Al_2O_3 particle was modified with Ba and Ti in a highly dispersed state, and this surface localization is expected to work effectively for sulfur resistance as discussed below.

The XRD patterns of the BaTi-B and the Ba-B catalysts after 750 ˚C thermal aging followed by the sulfur exposure treatment are shown in Fig. 7. A diffraction peak at 43 ˚, attributed to $BaSO_4$, was recognized on the Ba-B catalyst but not on BaTi-B. The size of the $BaSO_4$ particles on Ba-B was estimated using Scherrer's formula to be 10 nm. Because no sulfur concentration in the outlet gases from both of these catalysts during the sulfur exposure treatment was detected, the estimated amount of sulfur deposited on both of the catalysts was determined to be about 1.5 g/L (47 mmol/L). The comparison of the $BaSO_4$ peaks suggested that barium sulfate on BaTi-B was dispersed with a considerably fine structure compared with that on Ba-B. On the other hand, the diffraction peak originated from K and Li was not detected in both BaTi-B and Ba-B, which indicated that sulfate compound with K and Li did not exist as obvious crystal form. Furthermore, a diffraction peak at 39.8 ˚ attributed to Pt was recognized for both BaTi-B and Ba-B. The average particle sizes of the Pt on the BaTi-B and Ba-B catalysts calculated from these diffraction peaks were 34 nm and 35 nm, respectively. We think the distribution of Pt particle size ware similar between on the two catalysts which used the same oxide support.

It was assumed that a change of the storage materials from Ba to Ba-Ti did not affect the average Pt particle sizes although the distribution of Pt particles was not examined. Furthermore, the number of Pt active sites was equal in both catalysts. These results suggest that the addition of Ba compounds should have a predominant influence on the state of the NO_X storage materials and their catalytic performance.

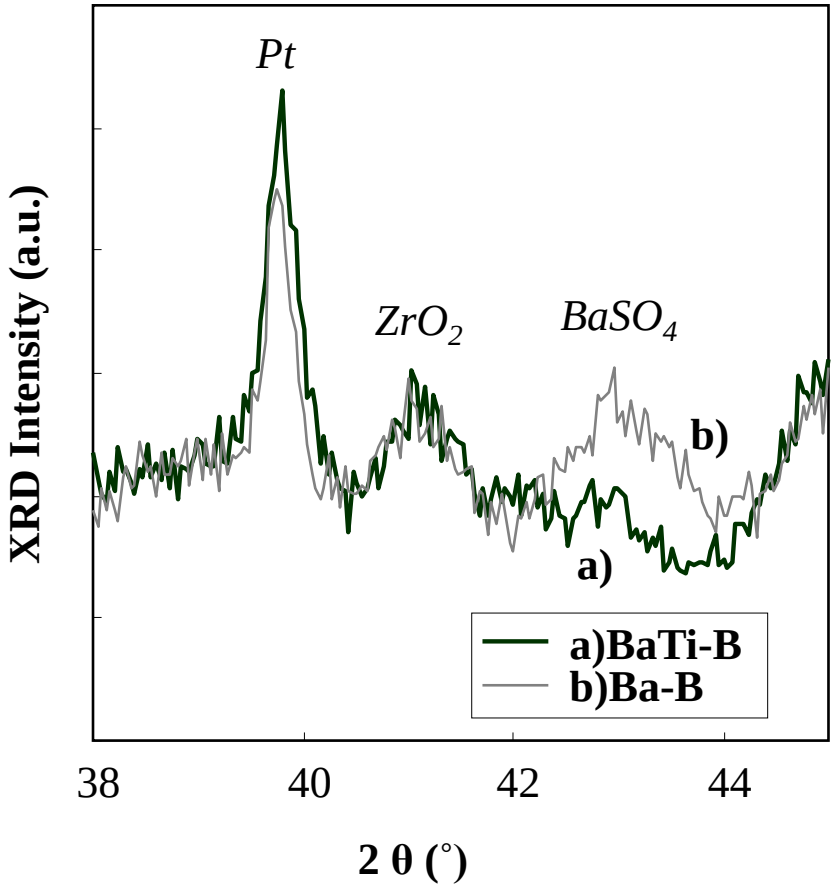

Fig. 7. XRD patterns of catalysts after 750 ˚C thermal aging followed by sulfur aging; a) BaTi-B and b) Ba-B.

The analysis of the supported BaTi catalysts revealed that utilization of the Ba-Ti composite solution led to formation of highly dispersed Ba compounds. Surface species on NSR catalysts composed of Ba (such as $BaCO_3$) have been reported to store NO_X and be converted to $BaSO_4$ through sulfur exposure [8]. Though no detailed information about the

structure of the Ba compounds on our BaTi catalyst was gathered, it was assumed that the formation of fine structures of Ba compounds on the BaTi catalyst prevented the formation of crystalline $BaSO_4$.

3.3. Catalytic performance

Sulfur desorption profiles during rich treatment of the BaTi-B and Ba-B catalysts at 600 ˚C or 650 ˚C after 750 ˚C thermal aging followed by the sulfur exposure treatment are depicted in Fig. 8. Further, the desorbed sulfur amount and the ratio of that amount to the inlet quantity during the sulfur desorption treatment are indicated in Table 5.

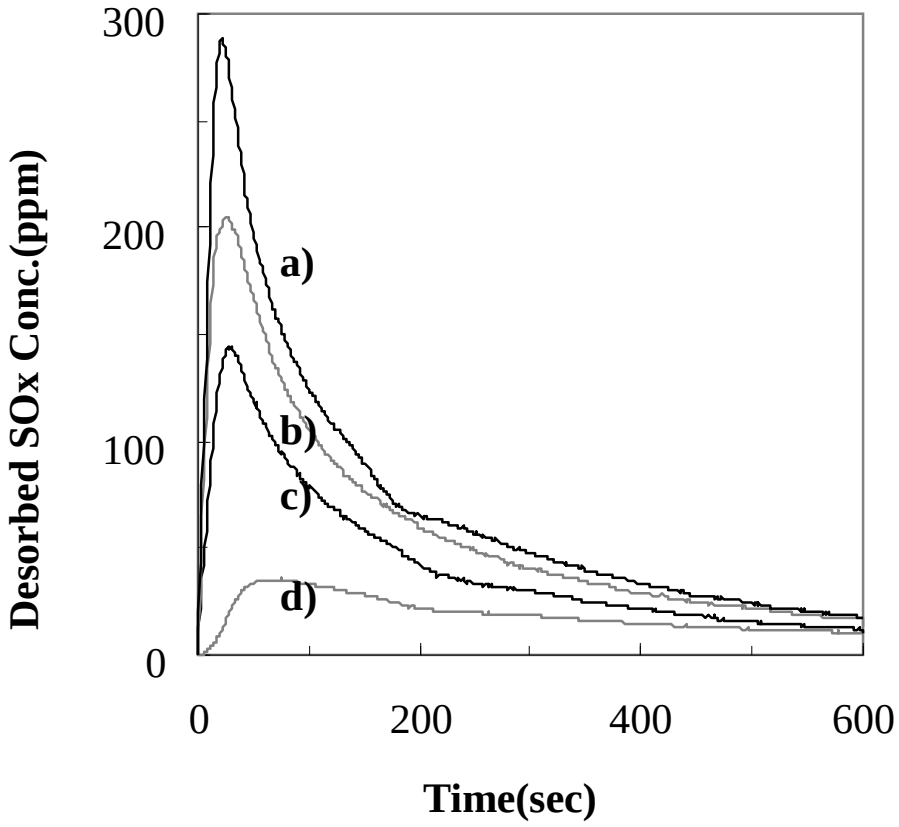

Fig. 8. Sulfur desorption profiles during SO_X regeneration from NSR catalysts after 750 ˚C thermal aging ; a) BaTi-B at 650 ˚C, b) BaTi-B at 600 ˚C, c) Ba-B at 650 ˚C and d) Ba-B at 600 ˚C.

Table 5.
Amount and ratio to inlet sulfur of desorbed sulfur during sulfur desorption

Sulfur desorption temperature (˚C)	Desorpted sulfur amount and the ratio			
	BaTi-B		Ba-B	
	S_d (mmol/L)[a]	R_d (%)[b]	S_d (mmol/L)	R_d (%)
600	22.7	47.6	7.2	15.2
650	26.9	56.6	16.2	34.1

[a] S_d: desorbed sulfur amount
[b] R_d: the ratio of desorbed sulfur to inlet one

The amount of desorbed sulfur from BaTi-B was higher than for the Ba-B catalyst at the same inlet gas temperature (more than 1.7 times). In these catalysts, Ba, K, and Li compounds are included as NO_X storage materials.

NO_X conversion activity on the BaTi-B and Ba-B catalysts after 750 ˚C thermal aging was measured during the repetitive procedure consisting of sulfur adsorption and desorption treatment. The NO_X profiles during lean/rich cycling of the NSR catalysts at 400 ˚C after sulfur desorption at 600 or 650 ˚C are shown in Fig. 9. The NO_X storage amount for BaTi-B was higher compared to that for Ba-B. The transition of NO_X conversion at 400 ˚C during repetitive sulfur adsorption (lean/rich cycles for 20 times at 400 ˚C) and desorption (rich at 650 ˚C) for 3 cycles can be seen in Fig. 10. During the sulfur adsorption procedure, NO_X conversion gradually declined after 20 lean/rich cycles. After desulfation treatment, NO_X conversion recovered to the same level as the previous treatment, which indicated that sulfur poisoned the active site for NO_X storage. In addition, recovering of NO_X conversion confirmed that sulfur removal treatment at 650 ˚C did not relate to thermal degradation for these 750 ˚C aged catalysts.

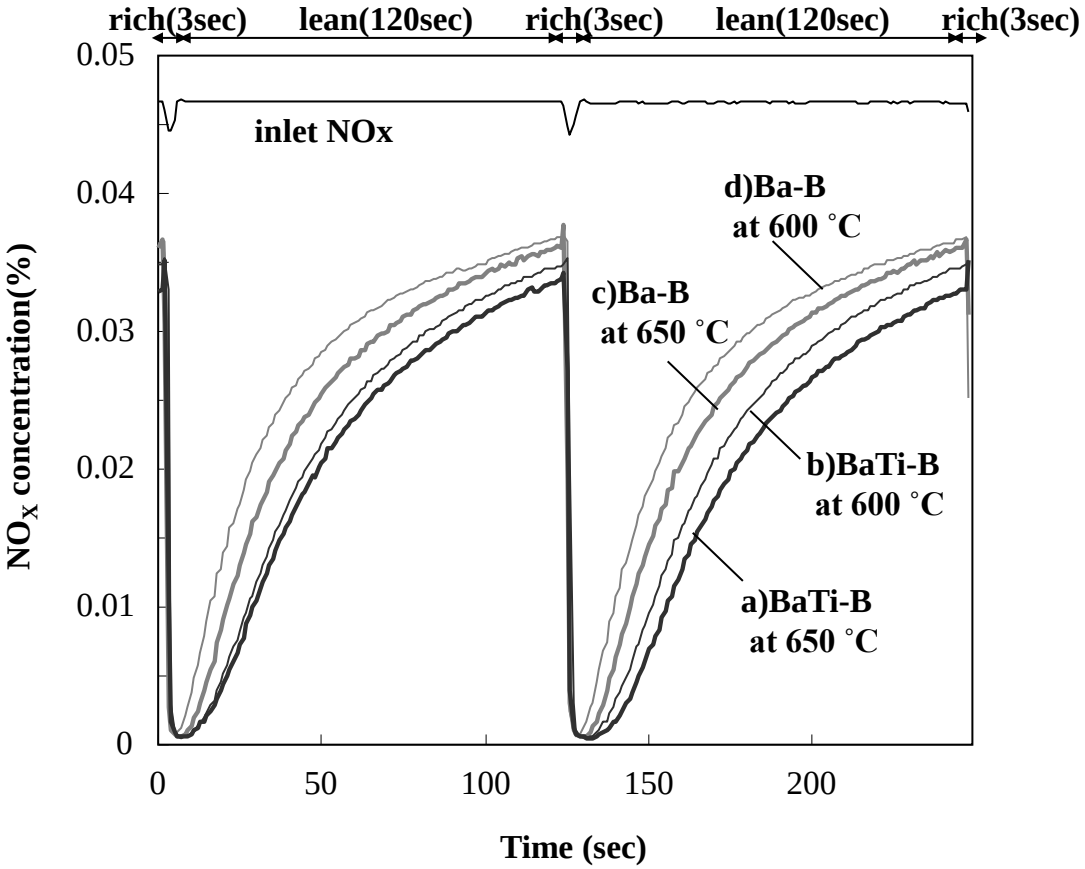

Fig. 9. NO_X concentration profiles at 400 ˚C during lean/rich cycle test over 750 ˚C thermal aged NSR catalysts after the sulfur desorption procedure; a) BaTi-B at 650 ˚C, b) BaTi-B at 600 ˚C, c) Ba-B at 650 ˚C and d) Ba-B at 600 ˚C.

The relationship between the amount of desorbed sulfur during desulfation treatment and the average amount of stored NO_X calculated from the concentration of NO_X during lean/rich cycles after sulfur desorption treatment at the different desorption temperatures on both the BaTi-B and Ba-B catalysts is shown in Fig. 11. The differences in NO_X storage activities between the tested catalysts during lean/rich cycles was similar to the differences in their sulfur desorption abilities.

On an NSR catalyst, NO_X is firstly stored during lean conditions and then is reduced by reacting with reductants such as H_2 and CO during rich conditions (vide supra).

The NSR reaction proceeds continuously through these repetitive processes. The important factors for performance of the catalyst are the dispersion of the platinum group metals and the storage materials, which take on the red-ox function, and the formation of nitrate by the reaction of NO_X. However, in this study of BaTi-B and Ba-B catalysts, the dispersion of Ba compounds as storage materials seems to be directly related to their performances because the particle size of Pt in both of the catalysts was nearly equal.

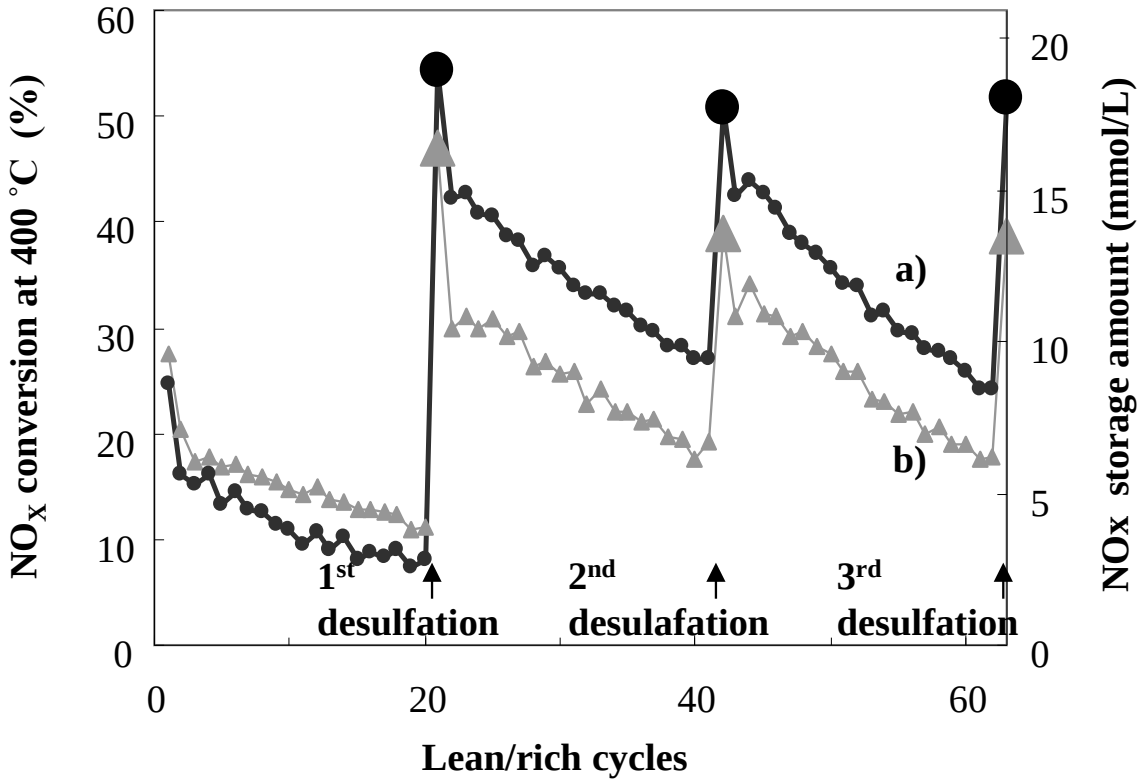

Fig. 10. NO_X conversion change at 400 ˚C during repetitive sulfur adsorption procedures (20 lean/rich cycles at 400 ˚C) and desorption (rich at 650 ˚C) over 750 ˚C thermal aged NSR catalysts; a) BaTi-B and b) Ba-B catalysts.

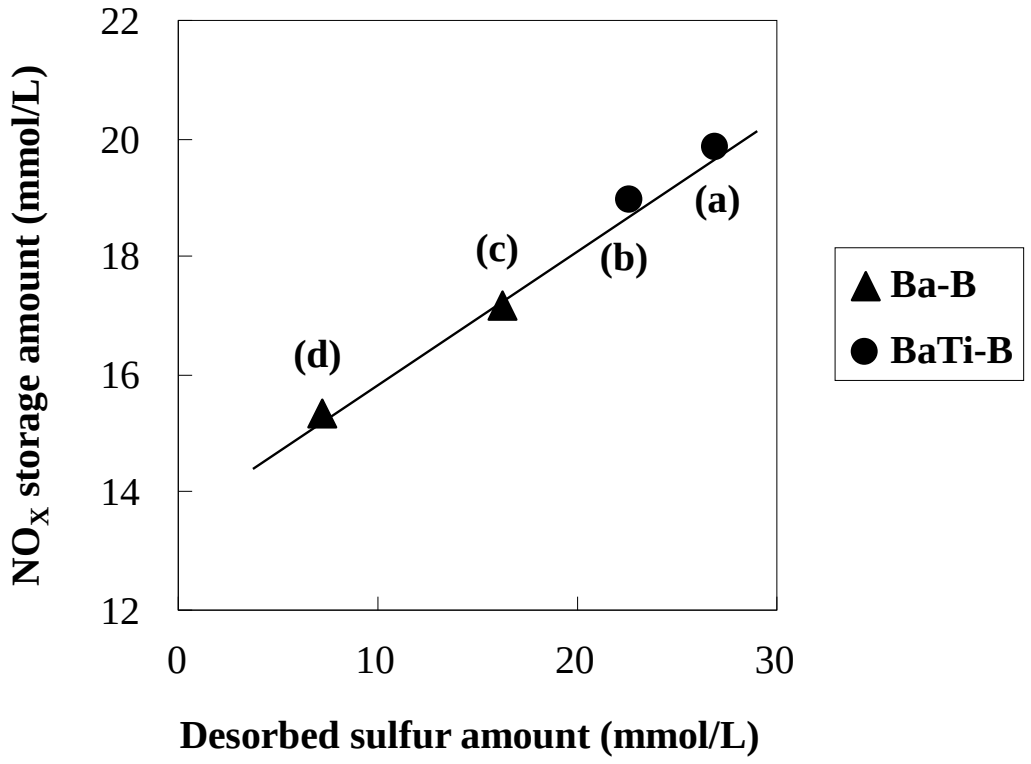

Fig. 11. Relationship between desorbed sulfur and NO_X storage amounts over 750 ˚C thermal aged NSR catalysts after sulfur regeneration; a) BaTi-B at 650 ˚C, b) BaTi-B at 600 ˚C, c) Ba-B at 650 ˚C and d) Ba-B at 600 ˚C.

As previously noted, one of the most important problems to be solved with NSR catalysts is the deactivation by sulfur poisoning. The improvement of catalyst activity for rapid desulfation is also necessary to obtain high catalytic performance. The deterioration of the NO_X storage ability of the NSR catalyst corresponds to the amount of adsorbed sulfur on the surface, and the regeneration of the catalytic activity depends on its sulfur removal ability. For practical use of NSR catalysts, NO_X storage sites need to be recovered by desulfation in a very short time. Ba compounds play an important role in securing larger NO_X storage amounts but Ba sulfates are difficult to decompose. Sulfur desorption from

Ba compounds strongly influences sulfur desorption from NSR catalysts. On the BaTi catalyst, we deduced that the formation of the fine Ba-Ti composite oxide identified from XRD and TEM analyses contributes to its high performance in sulfur desorption and is a primary factor for the high sulfur desorption ability.

On the BaTi-B catalyst, it is thought that the Ba compounds, by combining with Ti, are highly dispersed. Sintering of the sulfate during sulfur circulation is controlled in such a form, and this control leads to improvement in sulfur desorption. It has been shown that the decomposition temperature is lowered when the particle size of generated sulfates is smaller [13], and it has also been reported that barium sulfate with a particle size of 3 nm or less is resolved easily at lower temperature [14]. Furthermore, using pore size controlled supports has been found to improve the decomposition of sulfates by physically inhibiting the sintering of the sulfate [31]. In addition to the improvement resulting from greater Ba dispersion, the combination with TiO_2 works advantageously for desorption of sulfur compounds because of the instability of Ti sulfate. Though enough information on K and Li is not obtained for this examination, it is presumed to lead to the improvement of the NO_X storage performance by influencing on the decomposition of these sulfates by the Ti addition.

For practical use in a lean-burning exhaust, engine combustion management at a high temperature and rich atmosphere is necessary for reproducible sulfur deactivation with conventional NSR catalysts, which leads to a fuel penalty. Application of the Ba-Ti composite oxide for preparation of NSR catalysts makes it possible to shorten the treatment time for sulfur desorption because of its high sulfur desorption rate, resulting in improved catalyst performance with sulfur containing fuel.

4. Conclusions

We prepared a Ba-Ti composite aqueous solution using citric acid and H_2O_2 and then prepared an NSR catalyst containing a Ba-Ti composite oxide using this solution. It was found that by impregnation with the Ba-Ti composite aqueous solution, Ba and Ti in the catalyst were highly dispersed on the oxide support within the nm order size. Furthermore, the formation of the Ba-Ti composite oxide on the NSR catalyst enhanced sulfur desorption efficiency and led to high-performance NO_X conversion as a NO_X storage and reduction activity catalyst after desulfation treatment. It was assumed that the existence of nano-scaled Ba compounds combined with Ti was efficient for the inhibition of the sintering of barium sulfate and its facile decomposition. We believe that the dispersion of Ba compounds for NO_X storage materials using a Ba-Ti complex solution is an efficient way to improve the durability of NSR catalysts.

References

[1] M. Iwamoto, H. Yahiro, Y. Yu-u, S. Shundo, N. Mizuno, *Shokubai (Catalyst)* 32 (1990) 430.

[2] T. Tanaka, T. Okuhara, M. Misono, *Appl. Catal. B* 4 (1994)L1

[3] T. Tanaka, K. Yokota, N. Isomura, H. Doi, M. Sugiura, *Appl. Catal. B* 16 (1998) 199.

[4] F. Nakajima, I. Hamada, Catal. Today 29 (1996) 109; R. M. Heck, *Catal. Today* 53 (1999) 519.

[5] Japanese Patent No.3382361.

[6] Japanese Unexamined Patent Application Publication No. Hei 8-10575.

[7] N. Miyoshi, S. Matsumoto, K. Katoh, T. Tanaka, J. Harada, N. Takahashi, K. Yokota,

M. Sugiura, K. Kasahara, *SAE Tech. Paper* 950809 (1995).

[8] N. Takahashi, H. Shinjoh, T. Iijima, T. Suzuki, K. Yamazaki, K. Yokota, H. Suzuki, N. Miyoshi, S. Matsumoto, T. Tanizawa, T. Tanaka, S. Tateishi, K. Kasahara, *Catal. Today* 27 (1996) 63.

[9] A. Amberntsson, B. Westerberg, P. Engström, E. Fridell, M. Skoglundh, *Stud. Surf. Sci. Catal.; Catal. Deact.* 1999 (1999) 317.

[10] E. Fridell, H. Persson, L. Olsson, B. Westerberg, A. Amberntsson, M. Skoglundh, *Top. Catal.* 16/17 (2001) 133.

[11] S. Matsumoto, Y. Ikeda, H. Suzuki, M. Ogai, N. Miyoshi, *Appl. Catal. B* 25 (2000) 115.

[12] P. Engström, A. Amberntsson, M. Skoglundh, E. Fridell, G. Smedler, *Appl. Catal. B* 22 (1999) L241.

[13] D. H. Kim, J. Szanyi, J. H. Kwak, T. Szailer, J. Hanson, C. M. Wang, C. H. F. Peden, *J. Phys. Chem. B* 110 (2006) 10441.

[14] X. Wei, X. Liu, M. Deeba, *Appl. Catal. B* 58 (2005) 41.

[15] H. Suzuki, R. Muramoto, N. Takahashi, *Toyota Tech. Rev.* 46 (1996) 68.

[16] S. Matsumoto, Y. Ikeda, H. Suzuki, M. Ogai, N. Miyoshi, *Appl. Catal. B* 25 (2000) 115.

[17] I. Hachisuka, H. Hirata, Y. Ikeda, S. Matsumoto, *SAE Tech. Paper* 2000-01-1196 (2000).

[18] H. Hirata, I. Hachisuka, Y. Ikeda, S. Tsuji, S. Matsumoto, *Top. Catal.* 16/17 (2001) 145.

[19] N Takahashi, A. Suda, I. Hachisuka, M. Sugiura, H. Sobukawa, H. Shinjoh, *Appl. Catal. B* 72 (2007) 187.

[20] H. Imagawa, T. Tanaka, N. Takahashi, S. Matsunaga, A. Suda, H. Shinjoh, *J. Catal.* 251 (2007) 315.

[21] Kagakubinran Kisohen I, Maruzen, Tokyo (1993), p. 118-231 (4th ed.).

[22] I. Hachisuka, T. Yoshida, H. Ueno, N. Takahashi, A. Suda, M. Sugiura, *SAE Tech. Paper* 2002-01-0732 (2002).

[23] M. Rajendran, M. S. Rao, *J. Solid State Chem.* 113 (1994) 239.

[24] J-d. Tsay, T. T. Fang, *J. Am. Ceram. Soc.* 82 (1999) 1409.

[25] M. Kakihana, M. Arima, *Chem. Mater.* 11 (1999) 438.

[26] Japanese Patent No.4599817.

[27] F. Bonino, A. Damin, G. Ricchiardi, M. Ricci, G. Spano`, R. D'Aloisio, A. Zecchina, C. Lamberti, C. Prestipino, S. Bordiga, *J. Phys. Chem. B* 108 (2004) 3573.

[28] D. Srinivas, P. Manikandan, S. C. Laha, R. Kumar, P. Ratnasamy, *J. Catal.* 217 (2003) 160.

[29] T. T. Fang, M. S. Wu, J. D. Tsai, *J. Am. Ceram. Soc.* 85 (2002) 2984.

[30] H. B. Su, D. O. Welch, W. Wong-Ng, L. P. Cook, Z. Yang, *Appl. Phys. Lett.* 91 (2007) 172510.

[31] Japanese Unexamined Patent Application Publication No. 2002-11347.

Chapter 6

Studies on the regeneration of sulfur-poisoned NO_X storage and reduction catalysts, including a Ba composite oxide.

Abstract

The analysis of sulfur deterioration and regeneration of a NO_X storage and reduction (NSR) catalyst containing Ba as the storage material and TiO_2 as the support was conducted. It was found that the inhibition of sulfur re-adsorption during the sulfur desorption procedure under a rich atmosphere is important for improving sulfur desorption from a sulfur poisoned NSR catalyst, and that the combination of a Ba compound and a TiO_2 support is effective for the inhibition of sulfur poisoning under both lean and rich conditions. On the basis of these results, a highly dispersed Ba-Ti composite oxide catalyst was prepared using a Ba-Ti complex precursor in order to realize the nm-scale distribution of Ba and Ti. Furthermore, it was concluded that the principal factor contributing to the high performance of the Ba-Ti catalyst in terms of the sulfur desorption rate was its ability to inhibit repetitive adsorption during rich treatment for sulfur desorption.

1. Introduction

The curbing of CO_2 emissions, improved fuel efficiency and the clean-up of automobile exhaust gases are required for global environmental protection. Lean-burn gasoline and diesel engines achieve high fuel economy using higher air/fuel ratios (A/F). It is difficult, however, to remove NO_X in exhaust gases from these engines under excess oxygen conditions. Some NO_X purifying systems, such as selective NO_X reduction by hydrocarbons [1 - 6], NH_3 (urea) [7, 8], H_2 [9 - 11], and CO [9, 10, 12], have been researched and developed for commercial use.

A NO_X storage and reduction (NSR) catalyst system is one of the efficient ways to achieve NO_X purification [13, 14]. In the NSR system, NO_X (NO) is oxidized to NO_2 over the precious metals in the catalyst, then combined with the NO_X storage materials, and finally stored as nitrate ions in the first excess oxygen atmosphere (lean). In the following reduction stage, under a stoichiometric or reductive atmosphere (rich), the stored nitrate ions are released as NO_X (NO or NO_2) from the NO_X storage materials and then reduced to nitrogen.

Unfortunately, NSR catalysts are deactivated by sulfur poisoning and/or thermal deterioration. Sulfur deactivation, in particular, is the most serious problem to be solved. Sulfur poisons the precious metals [15, 16], supports [17], and NO_X storage materials [14, 15]. Furthermore, sulfur poisoning strongly influences the NO_X storage ability of the system. NSR catalysts include some alkali metals or alkaline earth metals that produce stable sulfates (SO_X) when exposed to exhaust gases, including sulfur compounds. It has been confirmed that the adsorbed sulfur transforms the NO_X storage materials into sulfates [14 - 16]. The formation of nitrate on the storage compound is thus inhibited, and therefore, the NO_X storage ability deteriorates. Consequently, the deactivation of NSR catalysts depends on the amount of sulfur poisoning of the catalyst [18]. In order to regenerate the

NSR catalyst after poisoning by SO_X, it is necessary to effectively decompose the sulfate using reductants such as H_2 and CO [19, 20]. However, continuous rich combustion and the addition of fuel to produce rich conditions result in a fuel penalty. Therefore, it is necessary to execute the regeneration in as short a time as possible. Previously, it has been reported that sulfur desorption depends on the particle size of the sulfate produced by the NSR catalyst [21, 22]. Accordingly, to improve the sulfur tolerance of the NSR catalyst, the crystal size of the NO_X storage materials must be reduced.

There have been several reports on improvements in the sulfur tolerance of NSR catalysts based on the above research. One of the methods involved the use of TiO_2 [23 - 27]. The decomposition temperature of sulfates on a TiO_2 support was found to be lower than that on an Al_2O_3 support under reducing conditions. Although this reduction of the decomposition temperature included the use of reducing gases such as H_2, the titanium sulfate that formed under exhaust gases including SO_X was assumed to be easily decomposed and more ready to release SO_X compared with other oxides.

Our approach to improve sulfur desorption from NSR catalysts is to make fine particles of Ba and Ti compounds with high homogeneity on a high surface area support, such as Al_2O_3 [10, 28]. In a previous report [28], a Ba-Ti composite oxide was formed on an NSR catalyst via impregnation of a Ba-Ti precursor solution composed of H_2O_2 added to a complex prepared using the citric acid method. It was found that Ba and Ti in the catalyst were highly dispersed on the oxide support at the nm scale, and furthermore, the formation of the Ba-Ti composite oxide on the NSR catalyst enhanced the sulfur desorption efficiency and led to high-performance NO_X conversion as a NO_X storage and reduction catalyst after desulfation treatment. It was assumed that the existence of nano-scale Ba compounds combined with Ti was efficient for inhibition of the sintering of barium sulfate and its facile decomposition.

In the present study, the adsorption and desorption properties of sulfur on NSR catalysts containing Ba and K as storage materials and Al_2O_3 and TiO_2 as supports were

examined in order to confirm that the combination of Ba ant Ti is effective for the improvement of NSR activity with respect to sulfur poisoning. An attempt was also made to understand the primary factors for the high performance of the BaTi catalyst using a Ba-Ti composite oxide.

2. Experimental

2.1. Catalyst preparation

Two catalyst formulations, BaTi-cat and Ba-cat, as summarized in Table 1, were prepared in this study. The synthetic route for preparation of the monolith catalysts has previously been described in detail [28]. Cordierite substrates (cylindrical, φ = 30 mm, L = 50 mm, 400 cells per square inch) were first coated with mixed oxides (9.45 g), including γ-Al_2O_3 (170 m^2/g), ZrO_2 doped TiO_2 (100 m^2/g), and ZrO_2 (90 m^2/g), for estimation of the catalytic activity. The ratio of Al/Ti/Zr in the mixed oxide was 1/0.19/0.38. These support materials were combined based on the previous research about NSR catalyst [17, 23, 26]. Next, PtRh supported catalysts were prepared by impregnating $Pt(NH_3)_2(NO_2)_2$ and $Rh(NO_3)_3$ followed by drying at 110 ˚C for 12 h and then calcining at 300 ˚C for 3 h in air. The amount of loaded Pt and Rh was 2 and 0.5 g/L, respectively. Subsequently, the BaTi catalyst was prepared by impregnating on the PtRh supported catalyst using a BaTi precursor solution, in which Ba and Ti were estimated to co-exist in a complex molecule [28]. On the other hand, the Ba catalyst was prepared by impregnating using an aqueous solution containing $(CH_3COO)_2Ba$. After these catalysts were dried at 110 ˚C for 12 h, they were calcined at 300 ˚C for 3 h in air. Finally, an aqueous solution containing CH_3COOK and CH_3COOLi was impregnated on the monolithic samples containing the Pt, Rh and Ba, such as the BaTi catalyst and the Ba catalyst. After these catalysts were dried at 110 ˚C for

12 h, they were calcined at 300 ˚C for 3 h in air. The loading amounts of Ba, K and Li were 0.2, 0.15, and 0.1 mol/L, respectively. Thermal aging was performed by exposing each catalyst to 1 L/min air at 750 ˚C for 5 h.

Table 1. Catalyst formulations

Catalyst	Support	Loaded components					
		Pt g/L	Rh g/L	Ba mol/L	Ti mol/L	K mol/L	Li mol/L
BaTi-cat	**mix oxides**	**2**	**0.5**	**0.2**	**0.2**	**0.15**	**0.1**
Ba-cat	**mix oxides**	**2**	**0.5**	**0.2**	**0**	**0.15**	**0.1**

mix oxides: γ-Al_2O_3 , ZrO_2 doped TiO_2 , and ZrO_2

2.2. Sulfur treatment and catalytic performance test

Table 2 shows the composition of the feed streams used to analyze the catalytic performance and sulfur treatment behavior of the catalysts. All of the tests were executed using a conventional fixed-bed flow reactor attached to a gas exhaust evaluation system (Best Sokki Bex-5900, CATA-5000) with a chemiluminescence analyzer for measuring the concentrations of NO_X, a paramagnetic analyzer for O_2, a flame ionization detector for hydrocarbons (HC), a flame photometric detector for total-S, a non-dispersive infrared analyzer for CO and CO_2, and a hydrogen analyzer (Horiba MSHA-1000L) with a mass spectrometer for H_2. A synthetic exhaust gas indicated in Table 2 was prepared by adjusting the mass flow controller of the particular exhaust gas components.

The catalysts were exposed to the SO_X adsorption gas atmosphere (from SA-L to SA-R in Table 2) for the sulfur exposure treatment, and to the SO_X desorption gas atmosphere (from SD-R1 to SD-R10 in Table 2) for the sulfur desorption treatment at 400, 600, 650, and 700 ˚C. The influence of the amount of sulfur on the deactivation of the NSR

catalyst was examined using the monolith-type NSR catalysts. The total S amount introduced to the catalyst during these treatments was varied from 0.5 to 7.5 g/L-catalyst by changing the concentration of SO_2 using cyclic lean-rich gases (120 s SA-L and 3 s SA-R) at 400 ˚C for 41 min. After the sulfur adsorption procedure, in which 1.5 g/L-catalyst of sulfur was accumulated at 400 ˚C, the gas composition was switched to the rich gases (from SD-R1 to SD-R10) in order to measure the sulfur species desorbed from the catalysts. The gas hourly space velocity (GHSV) was 54,000 h^{-1} for both the adsorption and desorption steps.

Table 2. Gas compositions for the catalytic performance test

Gas composition		O_2 %	NO ppm	CO %	H_2 %	THC ppmC	CO_2 %	SO_2 ppm	H_2O %	Flow rate L/miin
SOx adsoption procedure										
lean-rich	SA-L	5.50	470	0.00	0.00	100	10.4	variable	10.0	30.0
	SA-R	0.00	470	6.00	2.00	50	10.4	variable	10.0	30.0
rich	SA-R1	0.00	0	0.00	0.00	0	11.0	30.0	5.0	10.0
	SA-R2	0.00	0	0.10	0.00	0	11.0	30.0	5.0	10.0
	SA-R3	0.00	0	0.13	0.09	0	11.0	30.0	5.0	10.0
	SA-R4	0.00	0	5.00	2.00	0	11.0	30.0	5.0	10.0
	SA-R5	0.00	0	0.13	0.09	0	15.0	150.0	10.0	30.0
lean	SA-L1	5.50	470	0.00	0.00	100	10.4	150.0	10.0	30.0
SOx desoption procedure										
rich	SD-R1	0.00	0	0.10	0.00	0	15.0	0.0	10.0	30.0
	SD-R2	0.00	0	0.20	0.00	0	15.0	0.0	10.0	30.0
	SD-R3	0.00	0	0.00	0.05	0	15.0	0.0	10.0	30.0
	SD-R4	0.00	0	0.00	0.10	0	15.0	0.0	10.0	30.0
	SD-R5	0.00	0	0.00	0.20	0	15.0	0.0	10.0	30.0
	SD-R6	0.00	0	0.00	0.30	0	15.0	0.0	10.0	30.0
	SD-R7	0.00	0	0.10	0.01	0	15.0	0.0	10.0	30.0
	SD-R8	0.00	0	0.10	0.05	0	15.0	0.0	10.0	30.0
	SD-R9	0.00	0	0.13	0.09	0	15.0	0.0	10.0	30.0
	SD-R10	0.00	0	0.00	0.00	0	15.0	0.0	10.0	30.0
NOx storage and reduction measurement										
lean-rich	NSR-L	5.50	470	0.00	0.00	100	10.4	0.0	10.0	30.0
	NSR-R	0.0	470	6.00	2.0	50	10.4	0.0	10.0	30.0

The amount of adsorbed sulfur was also measured when the concentration of CO and H_2 as reducing gases was changed in the rich model gas containing SO_2. The monolith-type NSR catalysts tested above were crushed and 2 g of each was formed into 1-2 mm pellets for analysis. The amount of sulfur adsorption was measured during exposure to a flow of model gases with varying concentrations of CO and H_2 (from SA-R1 to SA-R4), as shown in Table 2. The temperature of the inlet gas during the rich sulfur treatment was 650 ˚C, and the amount of adsorbed sulfur necessary to reach saturation was

determined. Furthermore, the dependence of sulfur adsorption in a rich atmosphere on the temperature was estimated by measuring the amount of adsorbed sulfur for 20 min at 600, 650, and 700 ˚C under a flow of a simulated gas for rich desulfation that contained sulfur (SA-R5).

To investigate the influence of the Ba-Ti composite oxides on the desulfation of the NSR catalysts, the deactivated catalysts after treatment using lean gas (SA-L containing 30 ppm SO_2) at 400°C were reduced at 600 or 650 ˚C for 10 min under the sulfur desorption gas mixture (SD-R9) indicated in Table 2. Subsequently, they were exposed to the NO_X storage measurement gas atmospheres (NSR-L and NSR-R), cycling the lean (120 s) and rich (3 s) conditions as described above. These procedures were repeated several times. The NO_X conversion was calculated from the measured NO_X concentration.

2.3. Chemical bonding state of the adsorbed sulfur and Ba

The chemical bonding states of Ba and S in the catalysts after the sulfur exposure treatment were analyzed using XPS spectroscopy (Mg-Kα radiation) (PHI, PHI-5500MC). The diameter of the XPS analysis area was approximately 1 mm, and the depth was 2 - 3 nm. For the sulfur exposure treatment, catalysts were exposed to the sulfur adsorption gas atmosphere (Table 2), lean (SA-L1) for 220 s or rich (SA-R5) for 41 min, at 400 ˚C. The total sulfur amount accumulated on the catalyst during each treatment was 0.73 g/L-catalyst (22.8 mmol/L-catalyst), which was enough for sulfur deterioration of the NSR catalyst.

2.4. Distribution of sulfur in the catalyst coating

The distribution of S, Ba, K, Al, and Ti in the catalyst coating after the sulfur

exposure treatment was analyzed using electron probe X-ray microanalysis (EPMA). The diameter of the EPMA analysis area was approximately 2 - 3 μm, and the depth was also 2 - 3 μm. For the sulfur exposure treatment, catalysts were exposed to the same conditions as for the above XPS measurement. A piece of each of the sulfur poisoned samples was mounted in epoxy, ground, and polished. The polished samples were carbon coated to provide a conductive surface layer, and the EPMA spectra were measured using a JEOL JXA-8200 electron microprobe in order to determine the elemental distributions.

3. Results and discussion

3.1. Influence of the amount of poisoning sulfur on the NO_X storage and reduction activity

The influence of the amount of poisoning sulfur was examined on Ba-cat. The NO_X purification performance during the lean/rich cycles with various concentrations of SO_X were measured and plotted versus SO_2 exposure in Fig. 1. The amount of deposited sulfur during the cycles was also plotted in Fig. 1. The deterioration of the NO_X storage ability of Ba-cat did not depend on the concentration of SO_X, but on the amount of adsorbed sulfur on the surface, as reported previously [18]. The 80 % conversion that was achieved when the catalyst was not exposed to sulfur declined to 20 % after poisoning with 6.5 g/L sulfur. On an NSR catalyst, NO_X is first stored on the sites composed of alkali compounds during lean conditions, and then is reduced by reacting with reductants such as H_2 and CO under rich conditions. It is presumed that the precious metals, such as Pt, on the NSR catalyst play an important role in the reduction of the stored NO_X, and that the reduction is more effectively accelerated near the precious metals. The formation of a stable compound, such as $BaSO_4$, by sulfur poisoning gives rise to the deactivation of the

NSR catalyst.

On Ba-cat, 450 mmol of alkaline compound and 15.1 mmol of Pt and Rh were supported per 1 L of catalyst. The accumulated sulfur amount on the Ba-cat was 6.5 g/L (converted into 202 mmol/L), which corresponds to 45 % of the alkaline compounds. The deterioration of NO_X conversion was calculated to be 21 mmol, which corresponds to 10 % of the poisoned sulfur, and 1.4 times the Pt and Rh content. If the active center that performs the red-ox reaction contains Pt and Rh, it is presumed that the deactivation by sulfur poisoning is caused by poisoning of a portion of the storage sites that are near the precious metals.

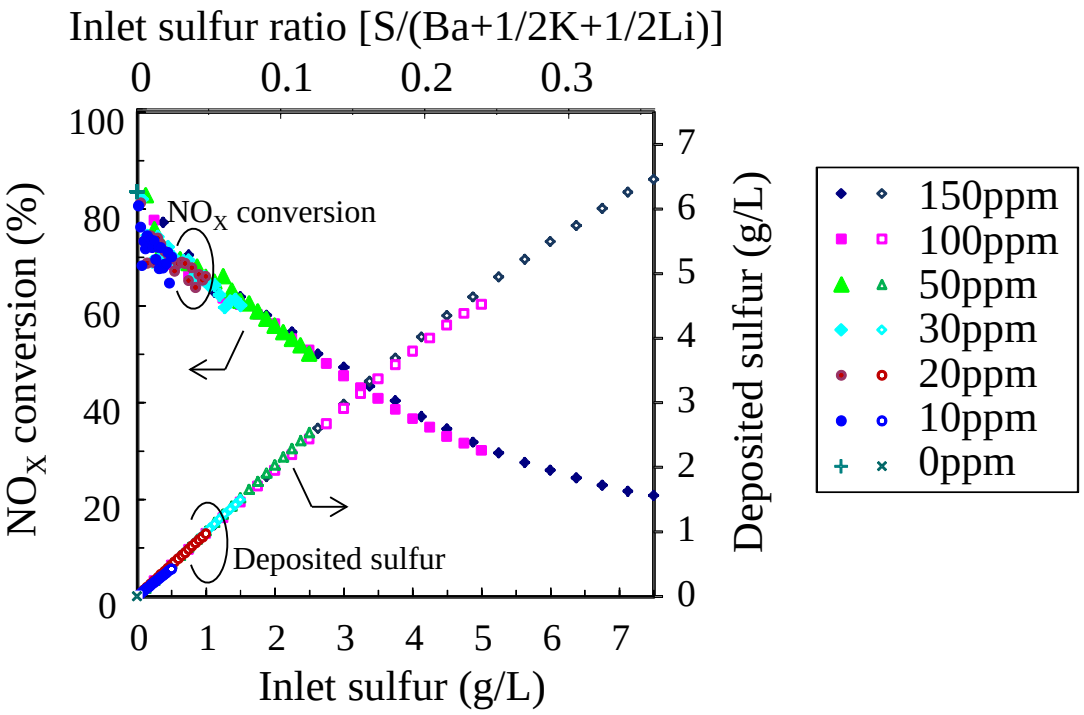

Fig. 1. NO_X conversion and deposited sulfur amount during the sulfur adsorption procedure at 400℃ under cycling of lean (120 s) and rich (3 s) conditions using the SA-L and SA-R gases.

3.2. Influence of the composition of the reductive gases on the regeneration of the sulfur poisoned catalyst

When actually used in a lean-burning engine system, a sulfur poisoned NSR catalyst is regenerated during exposure to rich gases that are produced by fuel-rich combustion or fuel dosing upstream of the NSR catalyst at temperatures over 600 ˚C. During the fuel-rich step, lean-burn engines emit CO, H_2, and hydrocarbons, which are effective for the decomposition and desorption of the sulfate and can restore the NO_X conversion activity. The correlation between the sulfur desorption rate and the NO_X conversion recovery has now been recognized [28]. Therefore, it is necessary to attain a higher sulfur desorption rate in order to obtain higher NO_X conversion.

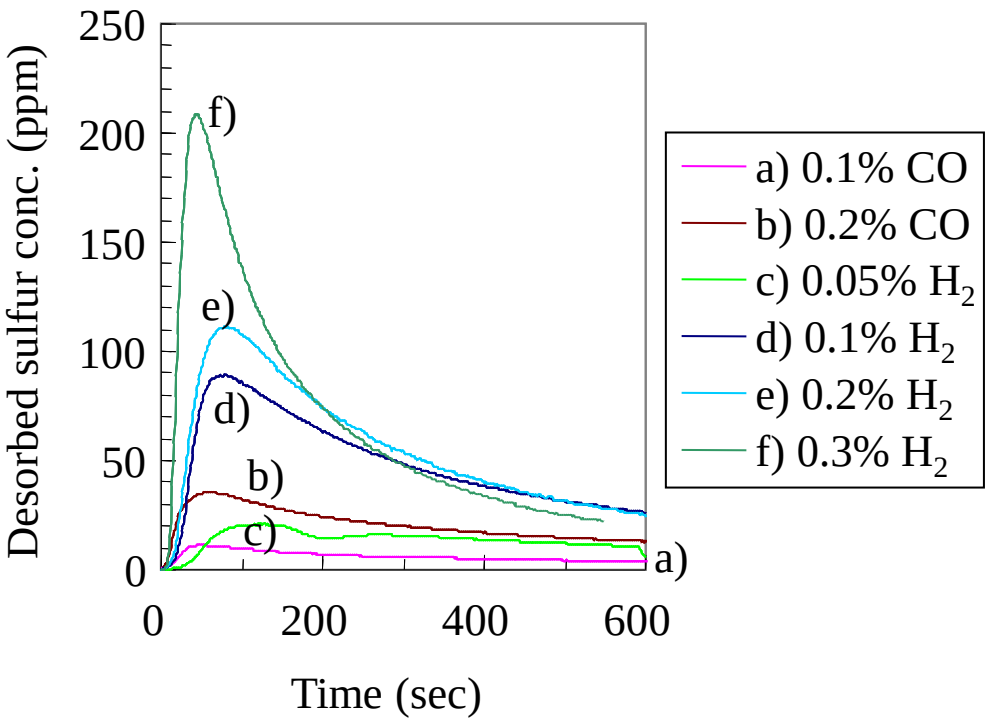

Fig. 2. Sulfur desorption profiles during regeneration for 10 min at 650 ℃ using the (a) SD-R1, (b) SD-R2, (c) SD-R3, (d) SD-R4, (e) SD-R5, and (f) SD-R6 gas composition, as indicated in Table 2.

The influence of the concentration of CO and H_2 in the simulated regeneration gases on the recovery of NO_X conversion activity was also investigated. The desorbed sulfur concentration during the rich regeneration step using various concentrations of CO and H_2 is shown in Fig. 2. In addition, the desorbed sulfur amount was plotted as a function of the inlet CO + H_2 concentration, and is depicted in Fig. 3.

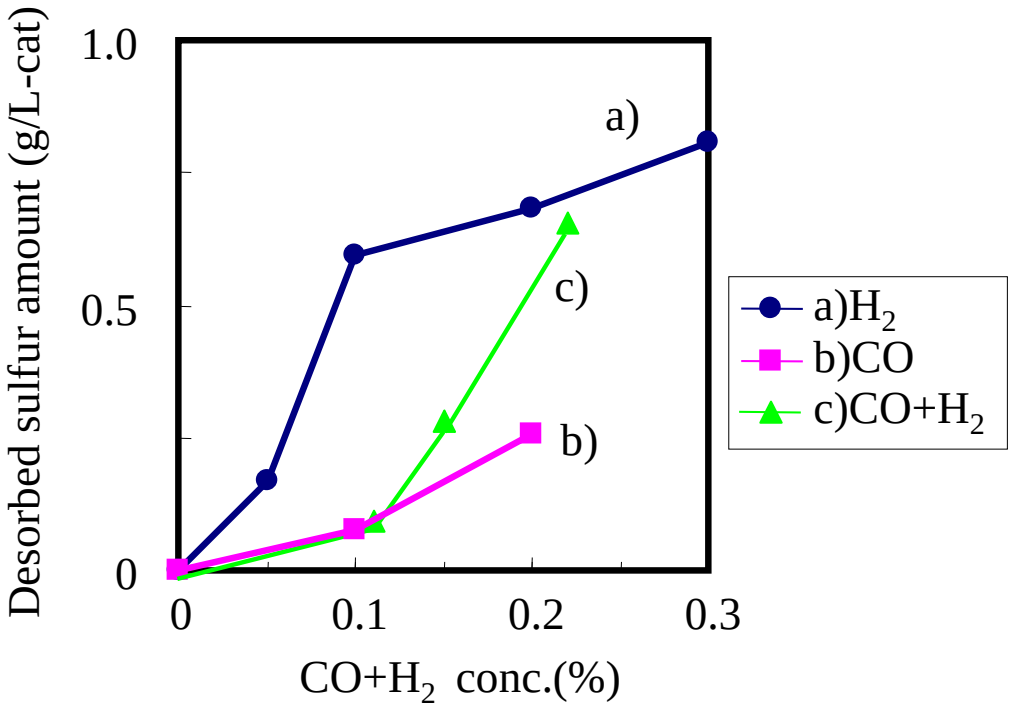

Fig. 3. Influence of the CO+H_2 concentration on the sulfur desorption amount during regeneration for 10 min at 650 ℃ . The gas compositions for regeneration are the same as those in Fig. 2.

The amount of desorbed sulfur using 0.1 % H_2 was 8 times that when using 0.1 % CO. This result indicates that H_2 is effective for sulfur desorption, as has been reported [17]. The desorbed sulfur amount was plotted against the outlet H_2 concentration measured 10 min after the beginning of the regeneration step, and this graph is shown in Fig. 4. It was found that the sulfur desorption rate depended on the H_2 concentration, indicating that H_2

is actually involved in sulfur desorption, even in the case when CO is used. Furthermore, when CO is supplied as a reducing gas in an atmosphere in which H_2O coexists, H_2 is assumed to be generated by the CO shift reaction on the catalyst as reported in the previous research [17], and it is thought that it participates in sulfur desorption as well.

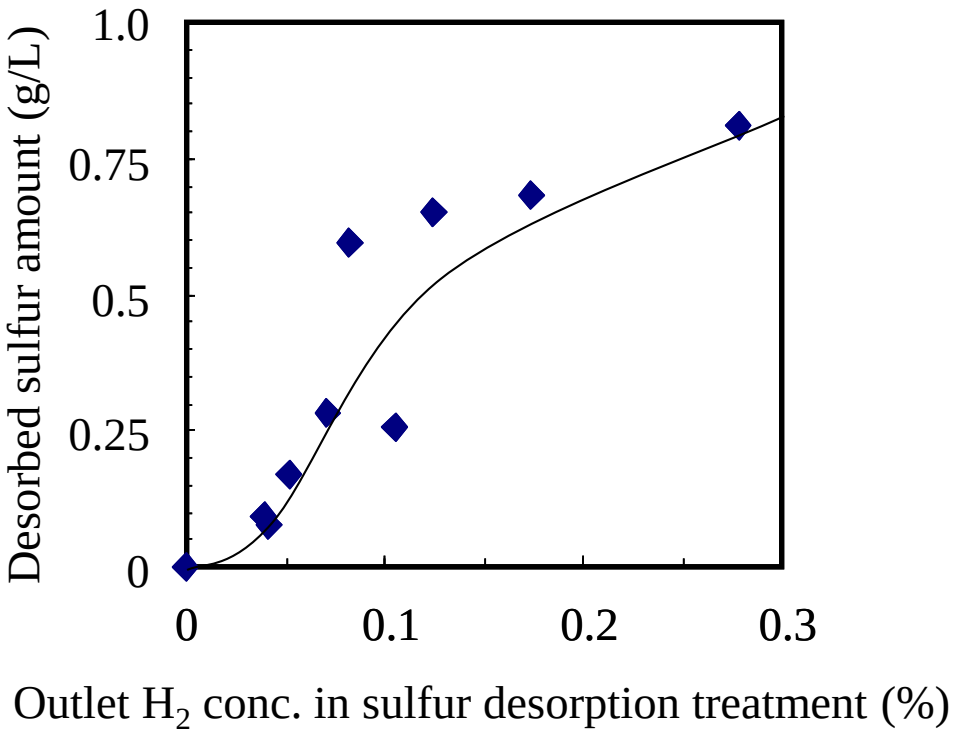

Fig. 4. Influence of the outlet H_2 concentration on the sulfur desorption amount during regeneration for 10 min at 650 ℃. The gas compositions for the regeneration are the same as those in Fig. 2.

Sulfur desorption during the rich regeneration step proceeds at a comparatively slow rate (on the order of minutes), as indicated in Fig. 2. One of the reasons for the slow desorption is assumed to be the strong stability of the sulfate, and another is the downstream repetitive adsorption of the desorbed sulfur. To clarify the possibility of the redeposition under rich conditions, the amount of adsorbed sulfur was measured in

different rich gas compositions. Sulfur concentrations as a function of time during exposure to the different rich conditions described in Table 2 are shown in Fig. 5, while the sulfur amount deposited on the catalyst is shown in Fig. 6. These results indicate that the sulfur definitely adsorbs onto the catalyst, even under rich conditions, and that the amount of adsorbed sulfur depends on the concentration of the reducing gases. When a catalyst with 1.5 g/L of deposited sulfur was subjected to the regeneration procedure using sulfur-free SD-R9 gas, the amount of sulfur that remained on the catalyst was approximately 0.75 g/L, which is equal to the amount of sulfur adsorbed during the sulfur adsorption procedure using sulfur-inclusive SA-R3 gases.

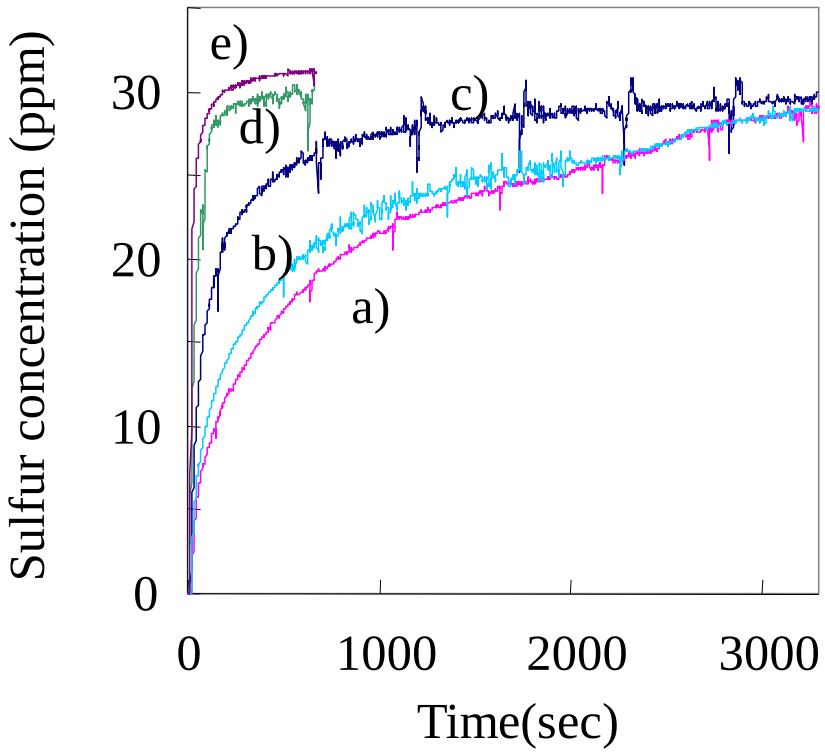

Fig. 5. Outlet sulfur concentration during sulfur adsorption using 2 g of catalyst at 650℃ under rich conditions: (a) SA-R1, (b) SA-R2, (c) SA-R3, (d) SA-R4, and (e) the inlet sulfur concentration.

Accordingly, the inhibition of the sulfur desorption during the regeneration procedure is assumed to be strongly influenced by the occurrence of sulfur redeposition, even in a rich atmosphere.

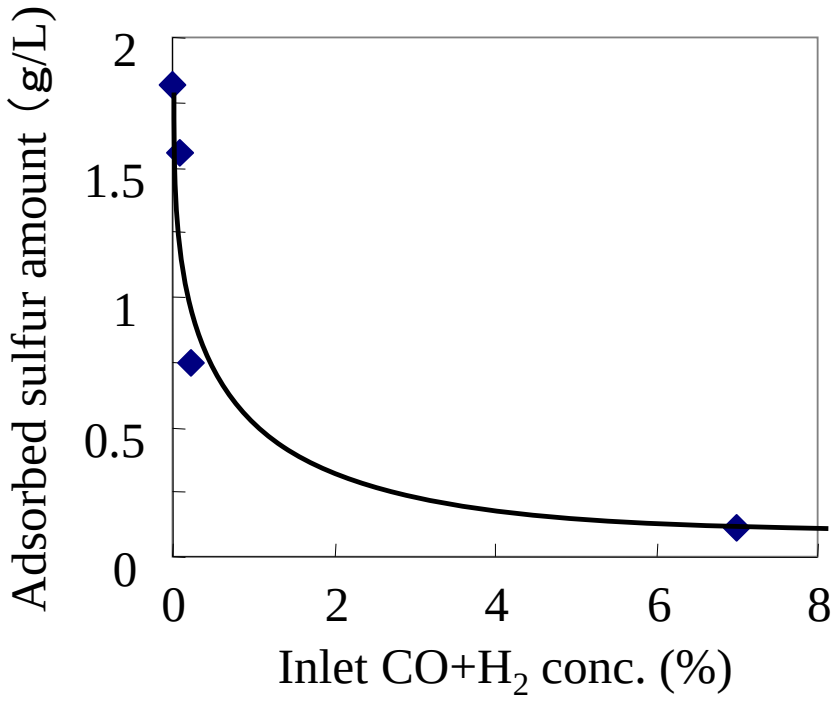

Fig. 6. Relationship between the adsorbed sulfur amount on Ba-cat and the inlet CO + H_2 concentration. The gas compositions for this reaction are the same as those in Fig. 2.

3.3. Chemical bonding state of the poisoned sulfur

The chemical bonding states of the adsorbed sulfur and barium under lean and rich conditions were examined using XPS spectroscopy. The S_{2p} and Ba_{3d} XPS spectra of Ba-cat after the sulfur adsorption procedure under lean and rich conditions using simulated gases for lean burn exhaust are shown in Fig. 7.

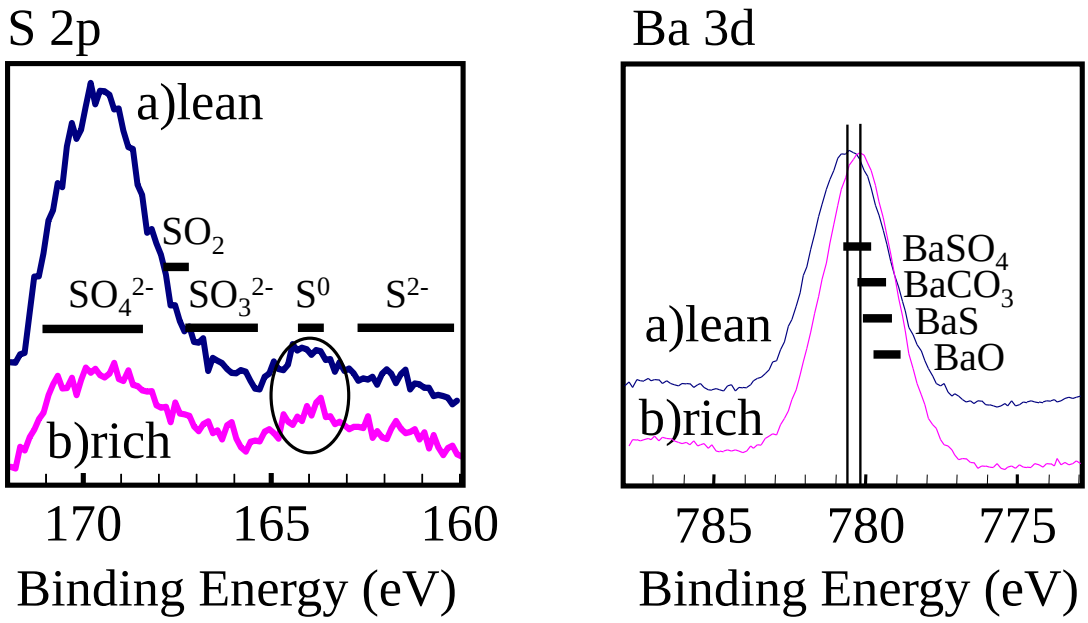

Fig. 7. XPS spectra of S2p and Bs3d of Ba-cat after sulfur poisoning after the sulfur exposure treatment using (a) lean gases (SA-L1) for 220 s and (b) rich gases (SA-R5) for 41 min at 400℃.

The S_{2P} spectra of both after lean treatment and rich treatment show three specific, recognizable peaks at 170, 164, and 162 eV, as indicated in Fig. 7, which are identified as sulfate (SO_4^{2-}), sulfur (S^0), and sulfide (S^{2-}), respectively [29]. It was observed that the ratio of S^0 and S^{2-} was relatively higher in the catalyst after rich treatment, while the sulfur existed mainly as sulfate after lean treatment. It can be concluded that the low valence state of sulfur was more favorable under rich conditions. The Ba_{3d} spectra indicated in Fig. 7 shows peak maxima at 780.1 eV after rich treatment and at 780.7 eV after lean treatment. It was observed that sulfur exposure under lean conditions predominantly resulted in the formation of $BaSO_4$. From these XPS results, it was determined that the treatment condition (lean or rich) influenced the chemical state of the adsorbed sulfur. Under lean conditions, the adsorbed sulfur existed in a highly oxidized state, such as sulfate or $BaSO_4$,

by strongly combining with Ba, and existed in a slightly reduced state, such as S^0 or S^{2-}, under rich conditions, where the interaction between sulfur and Ba is weak.

An XPS analysis by Poulston and Rajaram [30] indicated that the sulfate on a $Ba/Pt/Al_2O_3$ catalyst transformed to BaS after H_2 reduction at 800°C. The existence of BaS was also recognized in an x-ray diffraction (XRD) analysis completed by Elbouazzaoui et al. [31] after H_2 treatment of a sulfated catalyst at 800 ˚C. Amberntsson et al. [32] reported that deactivation is faster when SO_2 is present in the feed under rich conditions than under lean or continuous SO_2 exposure. Furthermore, Kim et al. [33] explained by XRD and XANES analyses that the suppression of the large BaS crystallites during reductive treatment on $Pt\text{-}BaO/CeO_2$ was an important factor for the maintenance of higher NSR activity. These results indicate that the poisoned sulfur exists as sulfate, mainly $BaSO_4$, under lean conditions, while different compounds, such as S^0 and S^{2-}, also exist under rich conditions. Accordingly, to achieve high performance as an NSR catalyst through the inhibition of sulfur poisoning under rich conditions, it is necessary to inhibit the reaction of SO_2 with Ba, and to stabilize the Ba on a support such as Al_2O_3.

3.4. Distribution of sulfur in the catalyst after sulfur poisoning

The distributions of the S, Ba, K, Al, and Ti concentrations on the cross section of the Ba-cat after lean and rich sulfur treatment using SA-L1 and SA-R5 gases, respectively, were measured using EPMA, and the results are presented in Figs. 8-11. In this estimation, Al_2O_3 and TiO_2 were selected as components of support oxides among the mix oxide support because ZrO_2 was existed in the two different forms, a ZrO_2 dopant in TiO_2 or an independent ZrO_2. The distributions of the S, Ba, Al, and Ti concentrations after sulfur treatment under lean conditions are shown in Fig. 8 as different colored dots, and those after sulfur treatment under rich conditions are presented in Fig. 9. The S, K, Al, and Ti distributions are also depicted in Figs. 10 and 11, along with the distributions for Al_2O_3 and

TiO_2, which were detected separately because a catalyst coating on Ba-cat was formed using a slurry consisting of a physically mixed powder containing Al_2O_3 and TiO_2. It can be seen that the Ba and K were spread uniformly over both the Al_2O_3 and TiO_2 in the coating. Accordingly, it is possible to compare the tendency for sulfur to adsorb onto each support. In addition, the combinations of coexisting Ba, K, Al, and Ti are indicated with different colors based on the concentration of each element at each measurement point in the bottom right figure. For example, in Fig. 9(a), the overlapping points for S, Ba, and Al are marked with white colored points, indicating the sulfur that is located on a Ba compound supported on Al_2O_3, while the yellow colored points correspond to the positions where sulfur is on a Ba compound without Al_2O_3.

After sulfur poisoning under lean conditions (Figs. 8 and 10), sulfur existed on the superficial parts of the catalyst coating layer, whereas it was found over the entire catalyst coating layer after sulfur treatment under rich conditions (Figs. 9 and 11). These results indicate that more sulfur adsorption sites existed under lean conditions than under rich conditions. From the comparison of the overlapping S-Ba-Al and S-Ba-Ti areas in Figs. 8 and 9, respectively, it was found that sulfur existed on Ba compounds supported on Al_2O_3 more preferentially than on TiO_2, because the white-colored sections in Figs. 8a and 9a, which indicate overlapping S, Ba, and Al, were confirmed to be present at higher ratios than those in Figs. 8b and 9b, which show the overlapping S, Ba, and Ti areas.

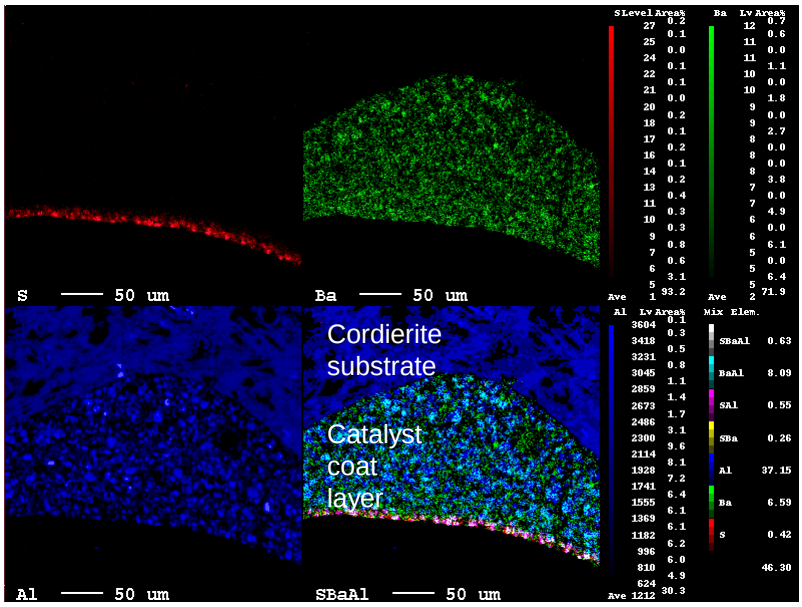

a) The distribution of S, Ba and Al

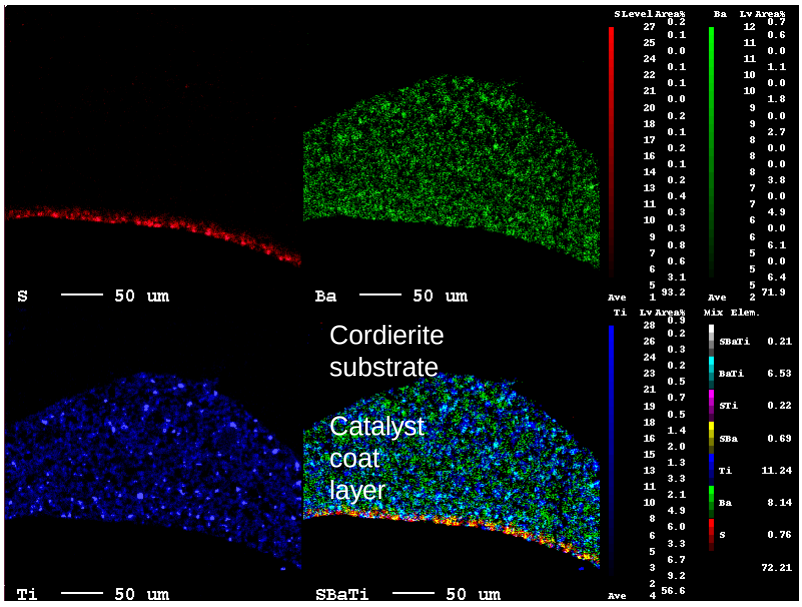

b) The distribution of S, Ba and Ti

Fig. 8. Series of elemental maps showing the distributions of (a) S, Ba, and Al, and (b) S, Ba, and Ti on the cross section of the Ba-cat after lean sulfur treatment using SA-L1 gases. The colored scale bar at the right shows the relative concentration. The lower right figure shows the overlapping combinations of (a) S, Ba, and Al, and (b) S, Ba, and Ti. Map conditions: 20 kV, 185 nA, 5-μm step size (in *x* and *y*), and a counting time of 15 ms per step. Each map is 0.5 mm × 0.5 mm.

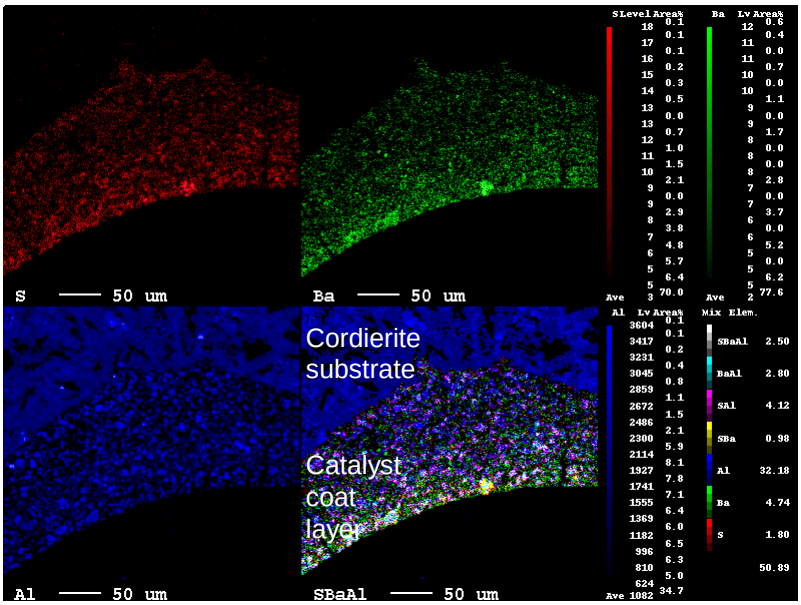

a) The distribution of S, Ba and Al

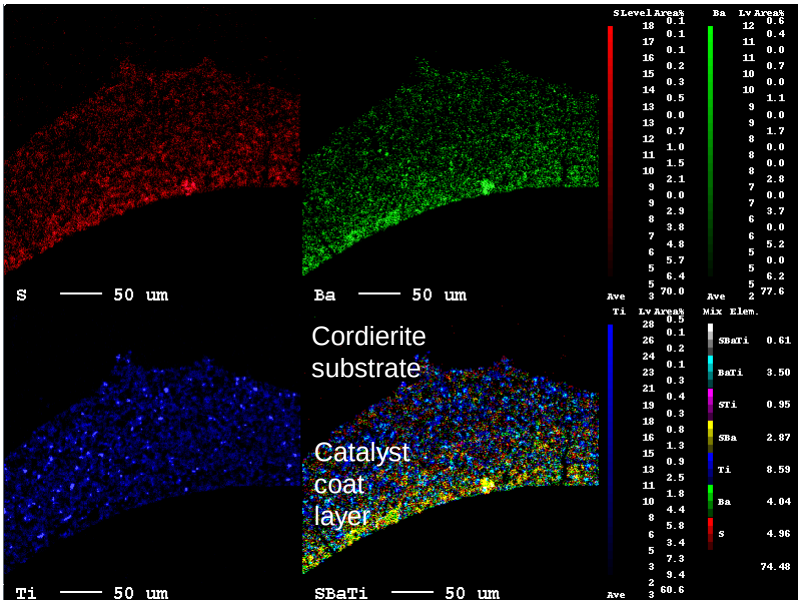

b) The distribution of S, Ba and Ti

Fig. 9. Series of elemental maps showing the distributions of (a) S, Ba, and Al, and (b) S, Ba, and Ti on the cross section of the Ba-cat after rich sulfur treatment using SA-R5 gases. The colored scale bar at the right shows the relative concentration. The lower right figure shows the overlapping combinations of (a) S, Ba, and Al, and (b) S, Ba, and Ti. Map conditions are same as Fig. 8.

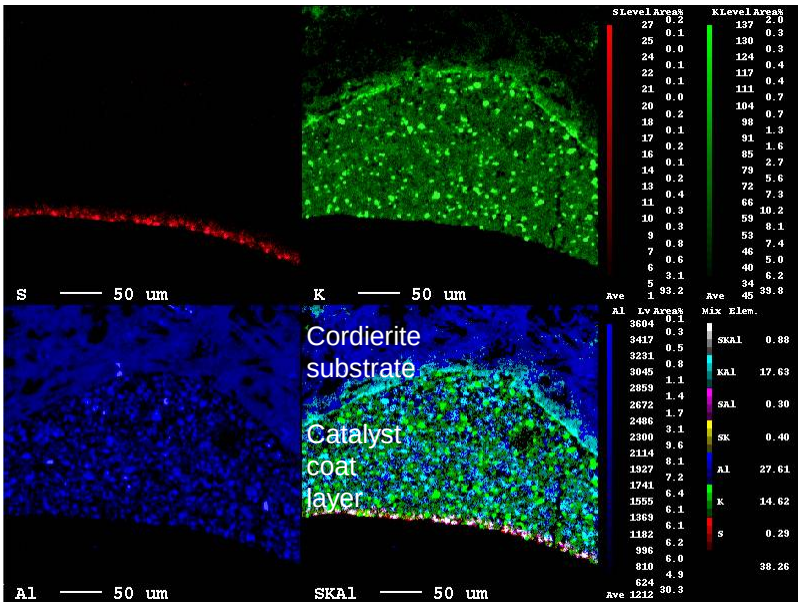

a) The distribution of S, K and Al

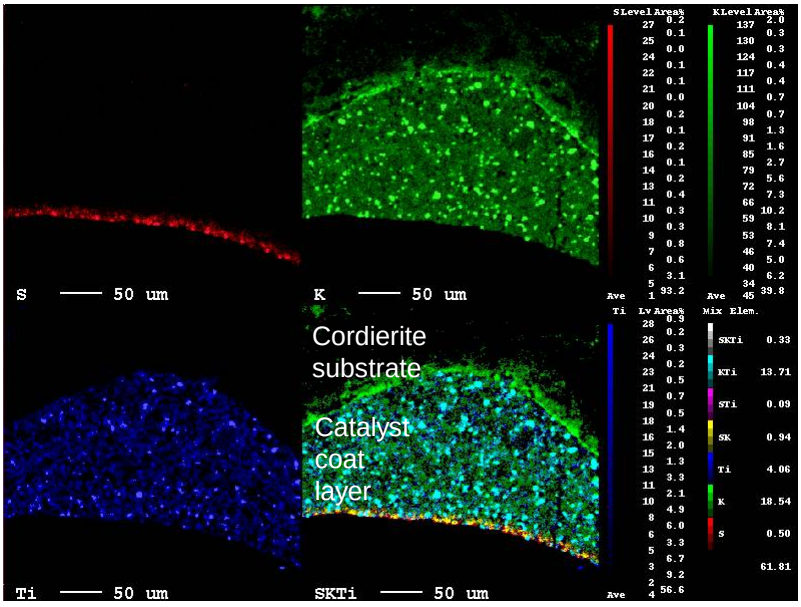

b) The distribution of S, K and Ti

Fig. 10. Series of elemental maps showing the distributions of (a) S, K, and Al, and (b) S, K, and Ti on the cross section of the Ba-cat after lean sulfur treatment using SA-L1 gases. The colored scale bar at the right shows the relative concentration. The lower right figure shows the overlapping combinations of (a) S, Ba, and Al, and (b) S, Ba, and Ti. Map conditions are same as Fig. 8.

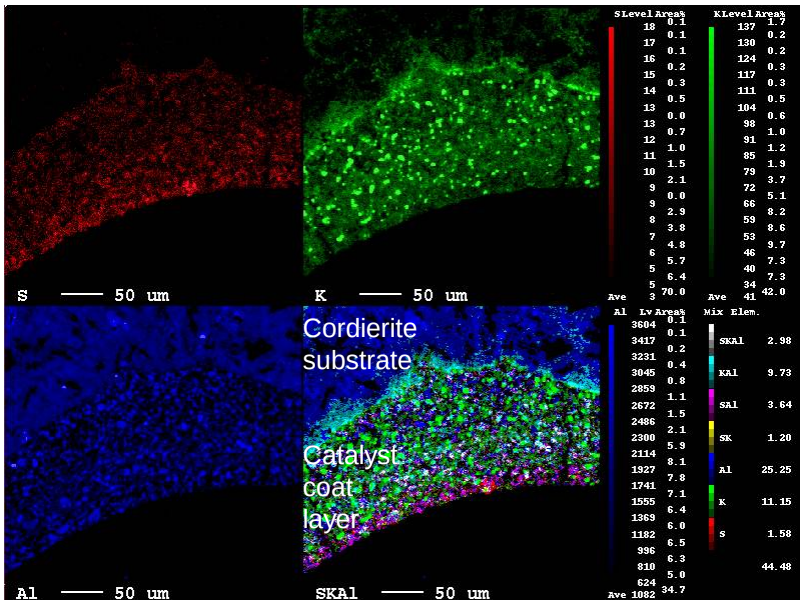

a) The distribution of S, K and Al

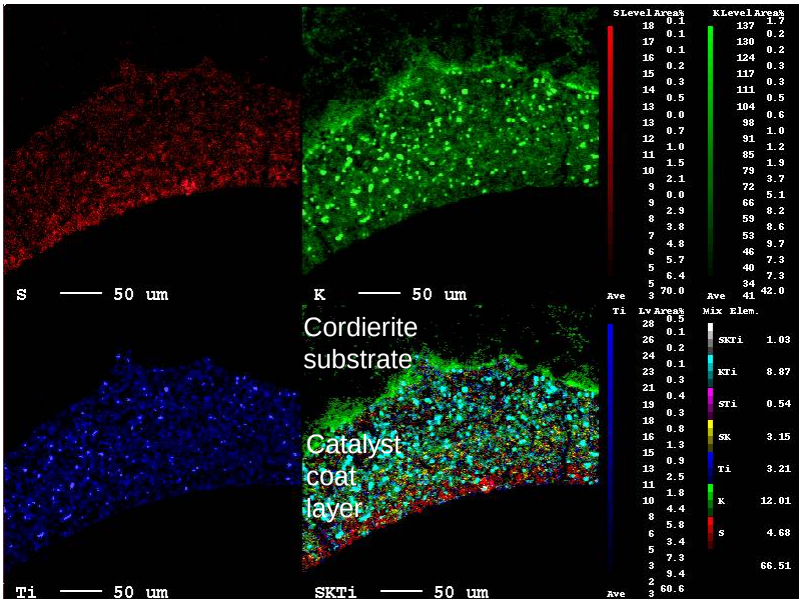

b) The distribution of S, K and Ti

Fig. 11. Series of elemental maps showing the distributions of (a) S, K, and Al, and (b) S, K, and Ti on the cross section of the Ba-cat after rich sulfur treatment using SA-R5 gases. The colored scale bar at the right shows the relative concentration. The below right figure shows the overlapping combinations of (a) S, Ba, and Al, and (b) S, Ba, and Ti. Map conditions are same as Fig. 8.

To obtain semi-quantitative information about the sulfur distribution from these results, the percentage of sulfur adsorbed on Ba compounds supported on Al_2O_3 ($R_{S\text{-}BaAl}$) was calculated as the ratio of the area of S-Ba-Al overlapping ($S_{Ba\text{-}Al\text{-}S}$) sites to the area of the overall Ba-Al overlapping region ($S_{Ba\text{-}Al}$): $R_{S\text{-}BaAl} = S_{S\text{-}Ba\text{-}Al} / S_{Ba\text{-}Al}$. In the same way, the percentage of sulfur adsorbed on Ba compounds supported on TiO_2 ($R_{S\text{-}BaTi}$), the percentage of sulfur adsorbed on K compounds supported on Al_2O_3 ($R_{S\text{-}KAl}$), and the percentage of sulfur adsorbed on K compounds supported on TiO_2 ($R_{S\text{-}KTi}$) were calculated as $R_{S\text{-}BaTi} = S_{S\text{-}Ba\text{-}Ti} / S_{Ba\text{-}Ti}$, $R_{S\text{-}KAl} = S_{S\text{-}K\text{-}Al} / S_{K\text{-}Al}$, and $R_{S\text{-}KTi} = S_{S\text{-}K\text{-}Ti} / S_{K\text{-}Ti}$, respectively. These percentages after lean and rich sulfur treatment are plotted in Fig. 12. The adsorbed sulfur percentages increase in the order K-Ti < Ba-Ti < K-Al < Ba-Al in both the lean and rich conditions. From this result, it was found that sulfur was preferentially adsorbed near the Ba compounds on the Al_2O_3 support, whereas its absorption was inhibited near K compounds and on the TiO_2 support. Furthermore, the percentage was on the same order in each part after both the lean and rich conditions.

Based on the above results, it was determined that sulfur poisoning occurred on Ba compounds more preferentially than on K compounds, and that it was reduced on the TiO_2 support in both the lean and rich atmospheres. The decomposition temperature of titanium sulfate is known to be 150 ˚C and in the static condition, and are considerably lower than that of aluminum sulfate (770 ˚C) [34]. Although these decomposition temperature change including reducing gases such as H_2, titanium sulfate that forms under exhaust gases including SO_X is assumed to be decomposed easily and release SO_X more readily compared with other oxides. Considering that Ba compounds play a significant role in the NSR reaction [25], it can be deduced that the inclusion of neighboring Ba and Ti atoms is an effective strategy for obtain higher NSR activity after sulfur poisoning, as discussed below.

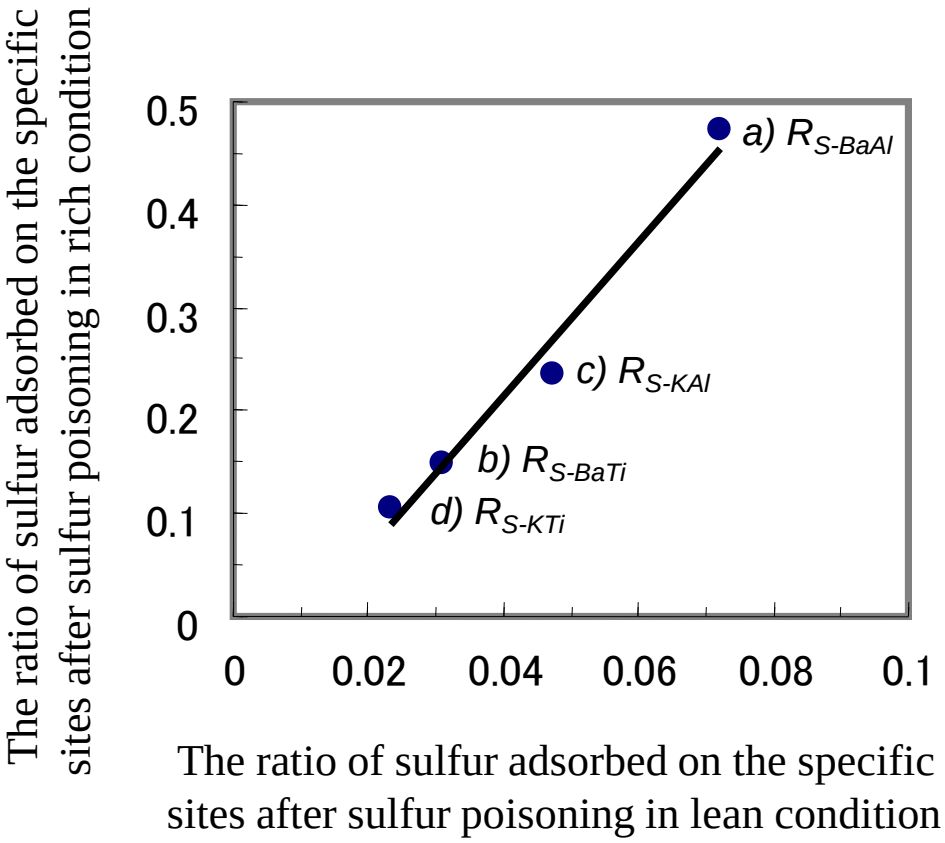

Fig. 12. The percentage of sulfur adsorbed on the specific sites estimated from the EPMA analysis after sulfur poisoning in lean and rich conditions using SA-L1 and SA-R5 gases, respectively. (a) $R_{S\text{-}BaAl}$; the percentage of sulfur adsorbed on Ba compounds supported on Al_2O_3, (b) $R_{S\text{-}BaTi}$; the percentage of sulfur adsorbed on Ba compounds supported on TiO_2, (c) $R_{S\text{-}KAl}$; the percentage of sulfur adsorbed on K compounds supported on Al_2O_3, and (d) $R_{S\text{-}KTi}$; the percentage of sulfur adsorbed on K compounds supported on TiO_2.

3.5. Examination of sulfur adsorption on BaTi-cat under rich conditions

Previously [28], it was revealed that the sulfur desorption ability was obviously increased using fine BaTi composite oxides as storage materials prepared using a stable

Ba-Ti citrate complex precursor, as indicated in Fig. 13. In addition, analysis using TEM-EDX and XRD revealed that the Ba and Ti in the catalyst existed as highly dispersed composite oxides on the support at the nm scale. Furthermore, it was concluded that the existence of nano-scale Ba compounds combined with Ti was efficient for the inhibition of the sintering of barium sulfate and its facile decomposition. On the present BaTi-cat, therefore, we examined the sulfur adsorption properties and the properties of the residue under rich conditions, and confirmed the above results.

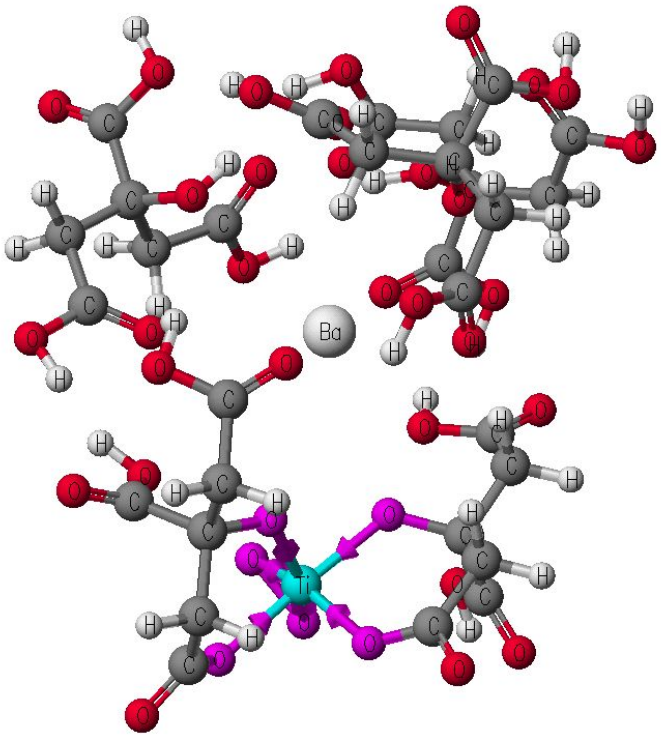

Fig. 13. Estimated structure of the Ba-Ti precursor complex.

In this study, Ba, K, and Li compounds were supported on the NSR catalyst as NO_X storage materials. As indicated in 2.1, K and Li compounds were impregnated on both BaTi-cat and Ba-cat in the same way. We assumed that the structure of the supported Ba compounds have a predominant influence on the catalytic activity, as described previously [28]. Although enough information on K and Li has not yet been obtained for this examination, they were presumed to lead to an improvement in the NO_X storage

performance by influencing the decomposition of the sulfates formed as a result of Ti addition. However, the diffraction peaks due to K and Li were not detected in either BaTi-cat or Ba-cat, indicating that sulfate compounds of K and Li did not obviously exist in the crystal form [28]. Accordingly, it was deduced that the deactivation of these NSR catalysts by sulfur results mainly due to the deterioration of the barium sites, and that TiO_2 combined with barium is effective for improving NSR activity through the structural changes caused by incorporation of barium compounds into BaTi-cat.

Furthermore, it is well-known that precious metals such as Pt strongly affect the catalytic activity and sulfur desorption ability. In a previous study, the average particle size of Pt on BaTi-cat and Ba-cat catalysts, as calculated from the diffraction peaks, was 34 and 35 nm, respectively [28]. It is thought that the Pt particle size distribution was similar for the two catalysts, which used the same oxide support. Although the distribution of the Pt particles was not examined, it is thought that the change in the storage materials from Ba to Ba-Ti did not affect the average Pt particle size. Accordingly, the difference between BaTi-cat and Ba-cat is mainly derived from the structure of the Ba compounds on the surface.

Fig. 14 shows the outlet sulfur concentration under SO_2-inclusive rich conditions at 600 - 700 ˚C. The difference in the amount of sulfur between the outlet concentration under rich conditions and the inlet concentration corresponds to the adsorbed sulfur amount (S_R). The relationship between the amount of accumulated sulfur during the measurements and the adsorption temperature is depicted in Fig. 15. The residual sulfur amounts after regeneration of the lean sulfated catalysts using SA-L gas (S_L) are also plotted in Fig. 15. In addition, the relationship between the amount of desorbed sulfur during the desulfation treatment and NO_X conversion calculated from the concentration of NO_X during the lean/rich cycles at 400 ˚C after the sulfur desorption treatment at different desorption temperatures on both the BaTi-cat and Ba-cat is shown in Fig. 16.

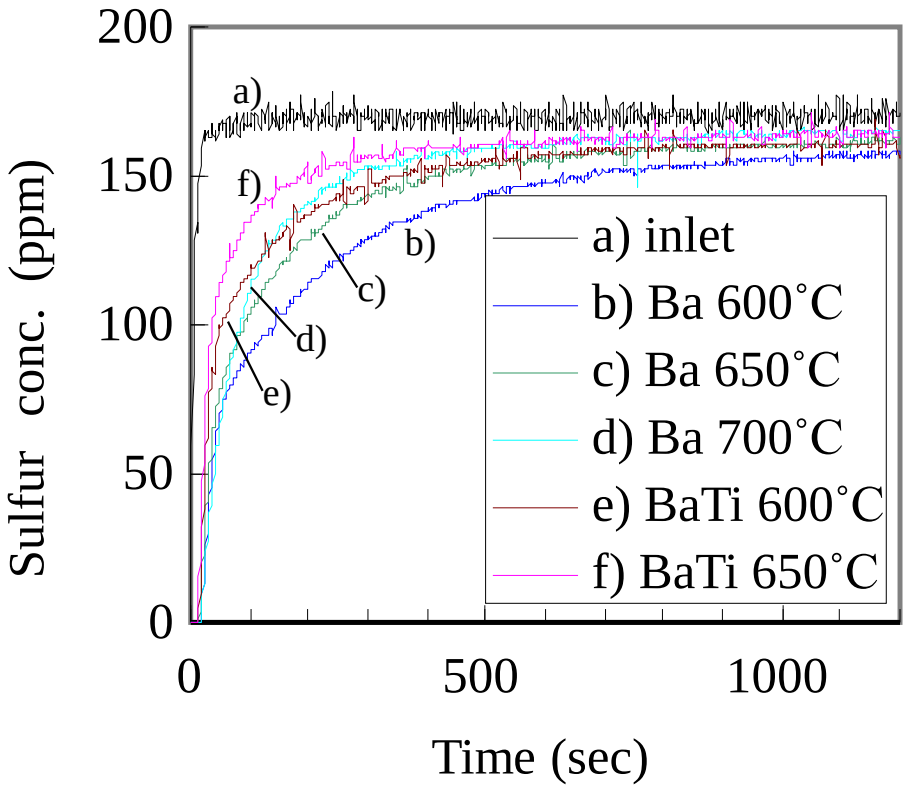

Fig. 14. Outlet sulfur concentration during sulfur adsorption using Ba-cat and BaTi-cat at various temperatures under rich conditions (SA-R5).

As can be seen in Fig. 16, the NO_X conversion activity correlated with the residual sulfur amount. As indicated in Fig. 1, NSR activity depends on the sulfur amount introduced into the catalyst. The differences in the NO_X storage activities between the tested catalysts during lean/rich cycles was similar to the differences in their sulfur desorption abilities. In Fig. 15, it can be seen that S_R and S_L for both catalysts gradually decreased as a function of the treatment temperature. In the case of Ba-cat, S_R corresponded to approximately 60 % of S_L. On the other hand, both S_R and S_L for BaTi-cat were at lower levels compared with those of Ba-cat. These results confirmed that sulfur adsorption under rich conditions was inhibited on BaTi-cat. Furthermore, S_R was estimated

to be at least 50 times that of Pt, indicating that most of the sulfur adsorption sites were other than Pt. These results showed that the stability of the adsorbed sulfur was lowered on the BaTi nano-composite oxide of BaTi-cat.

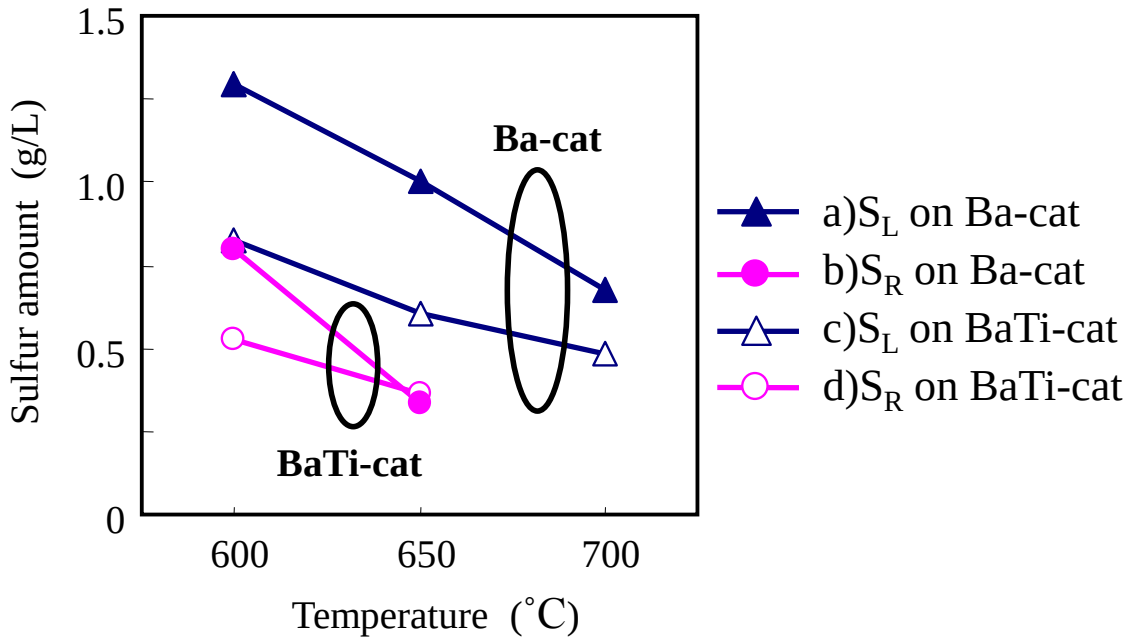

Fig. 15. Residual sulfur amount (S_L, S_R) on Ba-cat and BaTi-cat at 600 - 700 ℃. S_L: residual sulfur amount after regeneration (SD-R9) of the pre-sulfated catalyst at 400 ℃ using lean (120 s) / rich (3 s) gases (SA-L and SA-R including 30 ppm SO_2, respectively); S_R: adsorbed sulfur amount under rich conditions (SA-R5).

The desorption of sulfur from a sulfated catalyst is presumed to proceed in two steps; the first step is the decomposition of the sulfate, such as $BaSO_4$, and the second is the transfer of the decomposed sulfur compound from the inside layer to the outside, and from upstream of the monolith to downstream. It is thought that adsorption of sulfur under the rich regeneration procedure leads to inhibition of the latter transfer process.

Accordingly, the S_R value in Fig. 15 seems to be a correlation index for the inhibition of the transfer. Moreover, the difference between S_L and S_R appears to correspond to the facility of the sulfate decomposition. On BaTi-cat, it is assumed that the sulfur transfer was accelerated by the low interaction of sulfur under rich conditions, so that the sulfur desorption rate was enhanced. As indicated in 3.4, EPMA analysis of Ba-cat revealed that much of the adsorbed sulfur existed near the Ba and not near the Ti. On BaTi-cat, the Ba compound is finely dispersed via interaction with finely dispersed TiO_2 and forms a Ba-Ti nano-composite oxide, as reported previously [28]. On the other hand, Ba forms a stable Ba carbonate that has a strong affinity with the desorbed sulfur compounds on Ba-cat. It was therefore deduced that the difference in the surface structure of the Ba compound has an influence on the extent of the interaction between the sulfur and the Ba compound that leads to the improvement in catalytic performance, although the details of the mechanism of inhibition on BaTi-cat are not yet clear.

In Fig. 15, the difference between the S_L and S_R of BaTi-cat was smaller than that for Ba-cat. This result indicates that the enhancement of the decomposition rate of Ba sulfate also leads to an improvement in the sulfur desorption performance. The improvement in the decomposition rate of Ba sulfate on BaTi-cat is assumed to be due to the existence of microscopic Ba compounds combined with Ti that are efficient at inhibiting the sintering of barium sulfate and its facile decomposition, as reported previously [28]. This examination of the NSR catalyst using only the Ba compound clarified that the combination of Ba and Ti particles is important for reducing the amount of adsorbed sulfur under rich regeneration conditions, and thus for enhancing the restoration of the sulfur poisoned catalyst.

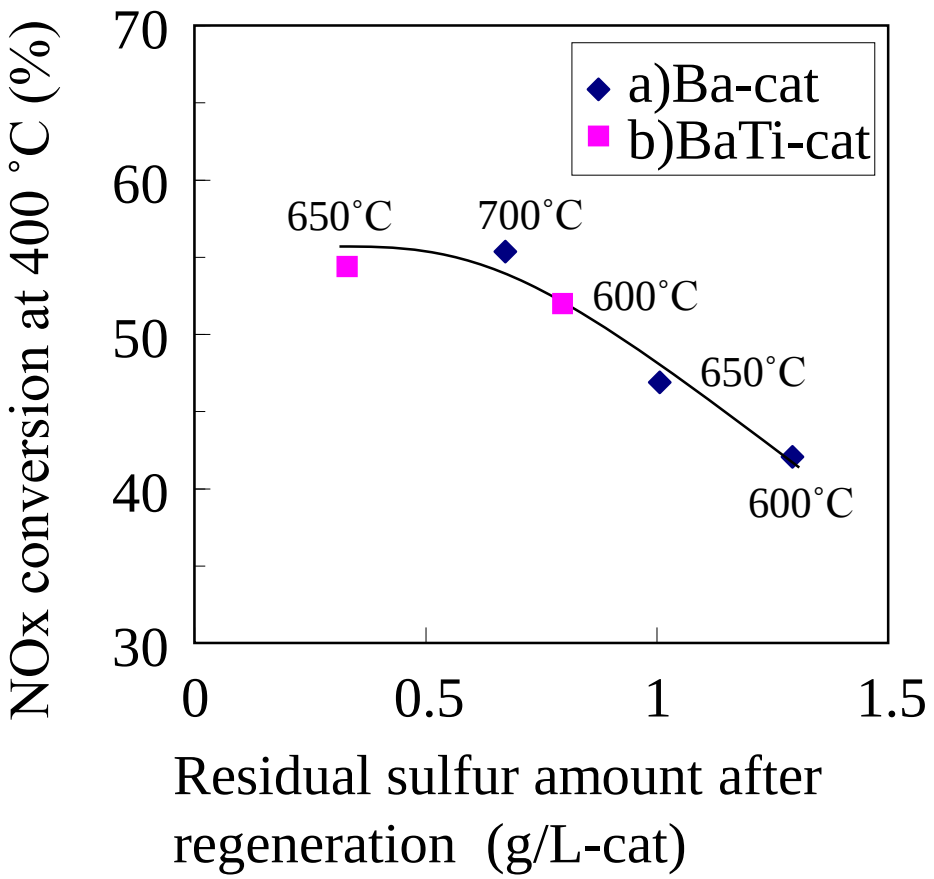

Fig. 16. Relationship between the residual sulfur amount and the NO_X conversion at 400 ℃ during lean (120 s) / rich (3 s) cycles using NSR-L and NSR-R gases on (a) Ba-cat and (b) BaTi-cat. Both catalysts were regenerated at 600 - 700 ℃ using SD-R9 gas after being sulfated using lean (120 s) / rich (3 s) gases (SA-L and SA-R) at 400 ℃.

In the literature, many researchers have reported the results of investigations of the sulfur poisoning and regeneration of NSR catalysts. For example, H_2-TPR, XRD and NO_X adsorption tests of a $PtBa/Al_2O_3$ catalyst [31] led to the conclusion that there are three types of sulfur poisoning compounds - Al sulfate, surface Ba sulfate, and bulk Ba sulfate - and that Ba sulfate changes to a stable BaS under rich conditions. The existence of BaS

(S^{2-}) on the sulfur poisoned NSR catalyst after various regeneration conditions was detected by XPS analysis, as reported previously [30]. In this study, the existence of low valence sulfur compounds such as S^0 and S^{2-} was confirmed after exposing simulated gases for lean burn exhaust. These low valence sulfur compounds were oxidized under lean conditions and stabilized as sulfate by reacting with alkaline compounds. This phenomenon is assumed to be a factor in the sulfur deterioration of NSR catalysts.

Consequently, the prevention of the accumulation of these low valence sulfur compounds during rich regeneration conditions is an important subject for further research. Previously, it was found that, on BaTi-cat, Ba was highly dispersed and combined with TiO_2 at the nm scale, and did not likely exist as $BaCO_3$ on the surface. On such a surface, it is presumed that the amount of sulfur desorption under rich regeneration conditions would probably be suppressed compared with that on Ba-cat, because of the low stability of S^0 or S^{2-}. Such factors are presumed to have led to the realization of the high sulfur desorption, including the decomposition of the sulfate and the transfer of the decomposed sulfur compound from the inside layer to the outside, and from upstream of the monolith to downstream.

4. Conclusions

The deterioration of NSR performance by sulfur poisoning and regeneration of the catalyst under various rich treatment conditions was investigated in order to determine the factors contributing to the sulfur desorption ability in catalysts using Ba compounds as a NO_X storage material. It was determined that NSR activity decreased as the amount of adsorbed sulfur increased under lean conditions, and increased as the amount of desorbed sulfur increased. In the regeneration procedure, use of H_2 gas was effective for sulfur desorption, and the rate of recovery depended on the concentration of H_2. The amount of

residual sulfur after the regeneration procedure using rich gases depended on the amount of sulfur adsorbed under the same rich gas conditions. Accordingly, re-adsorption of sulfur in the rich regeneration procedure was estimated to be an important factor contributing to the length of time required for sulfur desorption, and for inhibiting the recovery of activity after sulfur poisoning. In addition, it was found that sulfur poisoning occurred preferentially on Ba compounds compared to K compounds, and was reduced on a TiO_2 support both in lean and rich atmospheres. Furthermore, improvement of the sulfur regeneration of NSR catalysts containing Ba was achieved with a novel BaTi catalyst via the formation of a Ba-Ti composite oxide prepared using a Ba-Ti complex precursor. The sulfur adsorption amount under rich conditions on the BaTi catalyst was suppressed compared with that on the conventional Ba catalyst, and it was concluded that the BaTi catalyst has a higher performance for NSR activity, including sulfur desorption and regeneration, due to the inhibition of sulfur adsorption under rich conditions. Furthermore, enhancement of the decomposition of sulfate also contributed to its performance. On the BaTi catalyst, Ba oxide is combined with nm-sized fine TiO_2, and the particle size of the Ba compounds also remains very small, which enables enhanced decomposition and inhibition of the re-adsorption of sulfur compounds during the rich regeneration procedure.

References

[1] M. Iwamoto, H. Yahiro, Y. Yu-u, S. Shundo, N. Mizuno, *Shokubai (Catalyst)* 32 (1990) 430-433.

[2] T. Tanaka, T. Okuhara, M. Misono, *Appl. Catal. B* 4 (1994) L1-L9.

[3] T. Tanaka, K. Yokota, N. Isomura, H. Doi, M. Sugiura, *Appl. Catal. B* 16 (1998) 199-208.

[4] T. Tanaka, K. Yokota, H. Doi, M. Sugiura, *Chem. Lett.* 5 (1997) 409-410.

[5] T. Tanaka, K. Yokota, N. Isomura, H. Doi, M. Sugiura, *Toyota Central R&D Review of Toyota CRDL* 33 (1998) 41-51.

[6] C. He, M. Paulus, W. Chu, J. Find, J. A. Nick, K. Köhler, *Catal. Today* 131 (2008) 305-313.

[7] F. Nakajima, I. Hamada, *Catal. Today* 29 (1996) 109-115.

[8] R. M. Heck, *Catal. Today* 53 (1999) 519-523.

[9] K. Yokota, M. Fukui, T. Tanaka, *Appl. Surf. Sci.* 121 (1997) 273-277.

[10] Japanese Patent No.3382361.

[11] Y. Reneme, F. Dhainaut, P. Granger, *Appl. Catal. B* 111(2012) 424-434.

[12] Japanese Unexamined Patent Application Publication No. Hei 8-10575.

[13] N. Miyoshi, S. Matsumoto, K. Katoh, T. Tanaka, J. Harada, N. Takahashi, K. Yokota, M. Sugiura, K. Kasahara, *SAE Tech. Paper* 950809 (1995).

[14] N. Takahashi, H. Shinjoh, T. Iijima, T. Suzuki, K. Yamazaki, K. Yokota, H. Suzuki, N. Miyoshi, S. Matsumoto, T. Tanizawa, T. Tanaka, S. Tateishi, K. Kasahara, *Catal. Today* 27 (1996) 63-69.

[15] A. Amberntsson, B. Westerberg, P. Engström, E. Fridell, M. Skoglundh, *Stud. Surf. Sci. Catal.; Catal. Deact.* 1999 (1999) 317-324.

[16] E. Fridell, H. Persson, L. Olsson, B. Westerberg, A. Amberntsson, M. Skoglundh, *Top. Catal.* 16/17 (2001) 133-137.

[17] S. Matsumoto, Y. Ikeda, H. Suzuki, M. Ogai, N. Miyoshi, *Appl. Catal. B* 25 (2000) 115-124.

[18] P. Engström, A. Amberntsson, M. Skoglundh, E. Fridell, G. Smedler, *Appl. Catal. B* 22 (1999) L241-L248.

[19] H. Hirata, I. Hachisuka, Y. Ikeda, S. Tsuji, S. Matsumoto, *Top. Catal.* 16/17 (2001) 145-149.

[20] F. E. Lopez-Suarez, M. J. Illan-Gomez, A. Bueno-Lopez, J. A. Anderson, *Appl. Catal.*

B 104 (2011) 261-267.

[21] D. H. Kim, J. Szanyi, J. H. Kwak, T. Szailer, J. Hanson, C. M. Wang, C. H. F. Peden, *J. Phys. Chem. B* 110 (2006) 10441-10448.

[22] X. Wei, X. Liu, M. Deeba, *Appl. Catal. B* 58 (2005) 41-49.

[23] N. Takahashi, A. Suda, I. Hachisuka, M. Sugiura, H. Sobukawa, H. Shinjoh, *Appl. Catal. B* 72 (2007) 187-195.

[24] H. Suzuki, R. Muramoto, N. Takahashi, *Toyota Tech. Rev.* 46 (1996) 68-74.

[25] I. Hachisuka, H. Hirata, Y. Ikeda, S. Matsumoto, *SAE Tech. Paper* 2000-01-1196 (2000).

[26] H. Imagawa, T. Tanaka, N. Takahashi, S. Matsunaga, A. Suda, H. Shinjoh, *J. Catal.* 251 (2007) 315-320.

[27] I. S. Pieta, W. S. Epling, M. García-Diéguez, J. Y. Luo, M. A. Larrubia, M. C. Herrera, L. J. Alemany, *Catal. Today* 175 (2011) 55-64.

[28] T. Tanaka, I. Tajima, Y. Kato, Y. Nishihara, H. Shinjoh, *Appl. Catal. B* 102 (2011) 620-626.

[29] J. F. Moulder, W. F. Stickle, P. E. Sobol, K. D. Bomben, Handbook of X-ray Photoelectron Spectroscopy.

[30] S. Poulston, R. R. Rajaram, *Catal. Today* 81 (2003) 603-610.

[31] S. Elbouazzaoui, E. C. Corbos, X. Courtois, P. Marecot and D. Duprez, *Appl. Catal. B* 61 (2005) 236-243.

[32] A. Amberntsson, M. Skoglundh, S. Ljungström, E. Fridell, *J. Catal.* 217 (2003) 253-263.

[33] D. H. Kim, J. H. Kwak, J. Szanyi, X. Wang, G. Li, J. C. Hanson, C. H. F. Peden, *J. Phys. Chem. C* 113 (2009) 21123-21129.

[34] Kagakubinran Kisohen I, Maruzen, Tokyo (1993), p. 118-231 (4th ed.).

Part 3

New method to improve low temperature NO_X removal using NO_X trapping catalyst

Chapter 7

Improved low temperature removal of NO_X from lean-burn exhaust via adsorption on TiO_2-modified Ag-alumina.

Abstract

TiO_2-modified Ag-alumina was studied as an NO_X trapping material with the aim of improving the removal of NO_X from lean-burn exhaust at low temperatures. This trapping material, in which both Ag and TiO_2 were finely dispersed throughout the alumina support on a nanometre scale, effectively adsorbed NO_X at temperatures as low as 150 ˚C. The TiO_2-modification of Ag-alumina improved the NO_X trapping performance of the material by enhancing NO adsorption in the presence of other gases, including CO, hydrocarbons, CO_2 and H_2O. This modified material also exhibited less deterioration resulting from sulfur poisoning as compared to either conventional NO_X storage and reduction (NSR) catalysts or unmodified Ag-alumina. TiO_2 was shown to be dispersed throughout the alumina in an octahedral structure, and spectroscopic analyses along with DFT calculations demonstrated that this dispersion is effective at stabilizing Ag in the material. It was also determined that Ag supported on octahedral TiO_2 formed active sites at which the redox reaction between Ag^0 and Ag^+ proceeded, and that NO was effectively

oxidized and adsorbed as nitro and nitrite species on the active surface composed of the dispersed Ag and TiO_2.

1. Introduction

The protection and conservation of the environment has become an increasingly important issue. A vital aspect of environmental protection is a reduction in CO_2 emissions, which can partly be accomplished by improving the fuel efficiency of automobiles and by reducing exhaust gas emissions. The fuel economy of lean-burning gasoline and diesel engines can be improved by using higher air/fuel (A/F) ratios, but these excess oxygen conditions make it difficult to remove NO_X in the exhaust gases. Various NO_X removal systems, such as selective catalytic reduction (SCR) using NH_3 or urea [1, 2] and NO_X storage and reduction (NSR) [3, 4], have been both studied and developed with the aim of finding practical means to lower NO_X emissions. Conventional SCR catalysts, however, are inefficient at removing NO_X at low temperatures (below approximately 200 ˚C). Therefore, present day NO_X removal systems have only a limited ability to meet increasingly stringent emissions regulations in the future under the low bed temperature conditions which may be applied to lessen CO_2 emissions.

In the case of SCR systems, it is well known that the use of urea as a reducing agent, and in particular the NH_3 produced by the decomposition of urea, works more efficiently and exhibits higher rates of NO_X conversion as compared to the conversion of either hydrocarbons (HC) [5 - 8] or CO [9 - 11]. To improve the low temperature NO_X removal abilities of NH_3-based SCR systems, it is necessary to explore ways to increase the decomposition rate of urea to NH_3, to improve the catalytic activity for the oxidation of NO to NO_2, and to increase the decomposition rate of intermediates such as NH_4NO_3. One means of improving the SCR process is to employ H_2 [9, 10, 12] as a reducing agent, a

modification which has been reported to allow NO_X conversion at temperatures below 150 ˚C. However, there are challenges associated with this process with regard to supplying sufficient H_2 to the catalyst, and also the undesirable production of N_2O.

In the NSR system, NO is oxidized to NO_2 over precious metals within the catalyst, and all NO_2 is then chemically combined with NO_X storage materials and stored as nitrate ions. In the subsequent reduction stage, under a stoichiometric or reducing atmosphere, the stored nitrate ions are released from the storage materials as NO_X (NO or NO_2) and then reduced to nitrogen. The proportion of NO_2 in the incoming exhaust is an important factor in determining the degree of storage activity, since the NSR system works more efficiently when the NO_2 content is higher than the NO content [13]. This is problematic since, at temperatures below 200 ˚C, platinum group metals (PGMs) present in the NSR system, such as Pt itself [14], catalyze the decomposition of NO_2 into NO and thus decrease the NO_X storage capacity. Furthermore, interactions between PGMs and basic compounds in the exhaust stream may change the oxidation state of the PGMs such that they are no longer in the metallic state, and this process can also lead to a decrease in NO_X reduction activity. Finally, a variety of additional gaseous compounds, such as H_2O, CO_2, CO, HC and SO_X are typically found in engine exhaust and it is important to exclude these other gases such that NO_X, and especially NO, are selectively adsorbed.

In an attempt to overcome these challenges with low temperature catalytic NO_X reduction, we explored the possibility of improving performance by combining an NO_X trap capable of adsorbing NO_X at low temperatures with an NO_X reduction catalyst, as shown in Fig. 1. Separating the NO_X storage and NO_X reduction sites in this manner, and applying appropriate materials at each location, is considered an effective means of improving the overall reduction efficiency. In a previous study, we investigated the possibility of such a system, and confirmed the improvements resulting from using separated catalysts [15, 16]. In the study reported herein, we focused on the low temperature NO_X trapping portion of the reduction system. The aims of this research were

to develop a material capable of trapping NO_X at low temperature, where the NO_X storage performance of NSR systems typically decreases, and to apply this material in a close-coupled NSR system to improve the NO_X reduction performance under low temperature conditions.

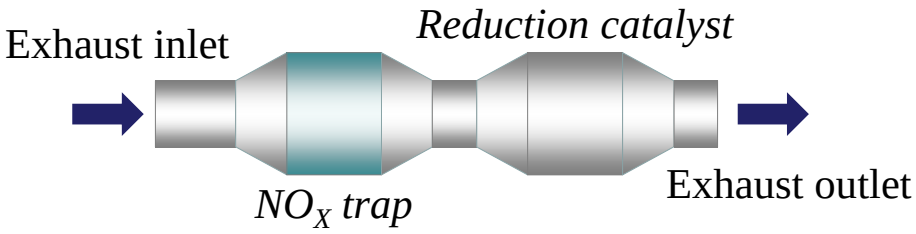

Fig. 1. NO_X reduction system incorporating a low-temperature NO_X trap.

Some materials have already been proposed for use as low temperature NO_X traps, including $BaSnO_3$ [17], $LaMnO_3$ [18], Mn–Ce oxide [19], $Pt/CeO_2/Al_2O_3$ [20] and $Ag/\alpha\text{-}Al_2O_3$ [21]. The associated literature, however, report that it is difficult to achieve sufficient NO_X trapping performance below 200 ˚C using any of these materials. In our previous work, Ag/Al_2O_3 has shown relatively high performance as an NO_X adsorption material, compared to other supported transition metals such as Mn, Cu and Ni [15]. Further improvement is required, however, before this material will exhibit satisfactory performance in practical applications in the presence of other exhaust gases, such as CO_2, H_2O, HC, CO and SO_X. In addition, it is also necessary for this material to adsorb large amounts of NO, which may be present in the exhaust at higher concentrations than NO_2.

Materials employing Ag, such as Ag/Al_2O_3, have been widely studied as SCR catalysts for the removal of hydrocarbons, including C_3H_6 [22], C_3H_8 [23] and CH_4 [24], rather than as NO_X traps. The effects of the structure of the Ag/Al_2O_3 catalyst on HC-SCR has been well researched, and various types of silver species, such as isolated Ag^+ ions, small Ag-aluminate clusters, Ag_2O and small charged metallic $Ag_n^{\delta+}$-like clusters, have

been proposed as the active sites for the HC-SCR reaction [25, 26]. Furthermore, the reaction mechanism associated with SCR of hydrocarbons has also been investigated, and nitrogen-containing species (for example, R-NO_2(a)) have been proposed as possible intermediates [27, 28]. Although the properties of supported Ag catalysts as low temperature NO_X traps was not the main focus of such work, it is recognized that they exhibit both NO oxidation and NO_X adsorption [29] and thus are expected to be effective as low temperature NO_X traps.

Based on the above background, we attempted to control the structure of the supported Ag to obtain suitably high performance of this material as a low temperature NO_X trap in combination with a reduction catalyst. From our previous studies on NSR catalysts, we have already confirmed that the utilization of dispersed TiO_2 is effective at improving both the sulfur regeneration [30 - 33, 45] and NO_X storage [32, 33, 45] abilities of catalytic systems. Therefore, we used surface-modified TiO_2 in an attempt to improve the performance of the NO_X trap, with respect to reducing the inhibitory influence of co-existing gases and promoting the desorption of SO_X. Herein, we report the results of our investigation into the NO_X reducing performance of a TiO_2-modified Ag-alumina (Ag/Ti/Al_2O_3), and discuss the NO_X trapping mechanism based on its characterization.

2. Experimental

2.1. Material preparation

Thirteen material formulations were prepared in this study, as summarized in Table 1. Ag/Ti/Al_2O_3, Ag/Al_2O_3, Ti/Al_2O_3 and BaKLi/Pt/Al_2O_3 were designated as NO_X traps and NSR catalysts, respectively. The Al_2O_3 supports were made first, by coating 200 g/L γ–Al_2O_3 (Rhodia, MI386, 170 m^2/g) on cylindrical cordierite substrates (φ = 30 mm, *L*

= 50 mm, 400 cells per square inch). Ti/Al_2O_3 was synthesized by impregnating the Al_2O_3 supports with an aqueous solution of Ti citrate, using a technique reported previously [30], followed by drying at 110 ˚C for 12 h and then calcining at 300 ˚C for 3 h in air. $Ag/Ti/Al_2O_3$ and Ag/Al_2O_3 were prepared by impregnating either the Ti/Al_2O_3 or Al_2O_3 supports with an aqueous $AgNO_3$ solution, followed by drying at 110 ˚C for 12 h and then calcining at 300 ˚C for 3 h in air. Pt/Al_2O_3 was made by impregnating Al_2O_3 supports with an aqueous solution of $Pt(NH_3)_2(NO_2)_2$, followed by drying at 110 ˚C for 12 h and then calcining at 300 ˚C for 3 h in air. $BaKLi/Pt/Al_2O_3$ was prepared by impregnating Pt/Al_2O_3, synthesized as above, with an aqueous solution containing CH_3COOBa, CH_3COOK and CH_3COOLi, followed by drying at 110 ˚C for 12 h and then calcining at 300 ˚C for 3 h in air. The loadings of Ag, Ti, Pd, Pt, Ba, K and Li were varied by changing the concentrations of the metal ion in the impregnating solutions. All materials thus prepared were calcined at 500 ˚C for 3 h in 5 % H_2/N_2 for initial activation and decomposition of precursor salt such as $AgNO_3$ and $Pt(NH_3)_2(NO_2)_2$ to obtain the reproducible data. Thermal aging was performed by exposing these materials to a 1 L/min air flow at 750 ˚C for 5 h.

Table 1. Material formulations.

	Catalyst	γ-Al_2O_3 support g/L	Ag mol/L	Ti mol/L	Pt mol/L	Ba mol/L	K mol/L	Li mol/L
Ag/Al_2O_3	Ag/A-1	200	0.24	-	-	-	-	-
	Ag/A-2	200	0.4	-	-	-	-	-
$Ag/Ti/Al_2O_3$	AgTi/A-1	200	0.24	0.03				
	AgTi/A-2	200	0.24	0.1				
	AgTi/A-3	200	0.24	0.15	-	-	-	-
	AgTi/A-4	200	0.24	0.27				
	AgTi/A-5	200	0.24	0.5	-	-	-	-
	AgTi/A-6	200	0.24	0.75	-	-	-	-
	AgTi/A-7	200	0.24	1	-	-	-	-
	AgTi/A-8	200	0.4	0.27	-	-	-	-
	AgTi/A-9	200	0.4	0.5	-	-	-	-
Ti/Al_2O_3	Ti/A	200	-	0.5	-	-	-	-
NSR	BaKLi/Pt/A	200	-	-	2	0.2	0.15	0.1

2.2. Performance testing

The performance of each material as a low temperature NO_X trap was evaluated using simulated diesel exhaust gases. Table 2 presents the compositions of the feed streams used to analyze the NO_X trapping performance and the sulfur treatment response of each material. All tests were performed using a conventional fixed-bed flow reactor attached to a gas exhaust evaluation system (Best Sokki Bex-5900, CATA-5000) with a chemi-luminescence analyzer for the measurement of NO_X concentrations, a paramagnetic analyzer for O_2, a flame ionization detector for hydrocarbons (HC), a flame photometric detector for total S, a non-dispersive infrared analyzer for CO and CO_2 and a hydrogen analyzer coupled with a mass spectrometer for H_2. Each synthetic exhaust gas as indicated in Table 2 was prepared by adjusting the mass flow controllers of the particular exhaust gas components.

Table 2. Gas compositions for NO_X trapping performance tests.

Gas composition		O_2 %	NO ppm	NO_2 ppm	CO ppm	H_2 %	THC ppmC	CO_2 %	SO_2 ppm	H_2O %	Flow rate L/miin
Pretreatment											
Rich pretreatment	P-R	0	0	0	1300	0.09	5	10.0	0	5.0	15.0
Lesn pretreatment	P-L	10.0	0	0	0	0	0	10.0	0	5.0	15.0
NO_X trap procedure											
NO_X adsorption	N-A1	10.0	100	0	800	0	400	10.0	0	5.0	15.0
	N-A2	10.0	0	100	800	0	400	10.0	0	5.0	15.0
NO_X desorption	N-D	10.0	0	0	0	0	0	10.0	0	5.0	15.0
SO_X poisoning procedure											
SO_X adsoption	S-AL	10.0	200	0	0	0	100	10.0	30.0	5.0	30.0
	S-AR	0	200	0	0	0	20000	10.0	30.0	5.0	30.0
SO_X desoption	S-D	0.1	0	0	0	0	2000	10.0	0	5.0	30.0

To investigate the NO_X trapping performance of the materials, thermally deactivated monolithic samples were first exposed to pretreatment gases (P-R and P-L as indicated in Table 2) at 400 °C, and subsequently exposed to NO_X atmospheres (N-A1 or N-A2) at 150 ˚C for 15 min, as indicated in Fig. 2. The quantity of NO_X adsorbed during

this stage was calculated from measurements of the outgoing NO_X concentrations during this step. Subsequently, the materials were exposed to the NO_X desorption gas (N-D) and heated at a rate of 11.5 ˚C/min to 400 ˚C under the same gas conditions. The quantity of desorbed NO_X was calculated from the outgoing NO_X concentration in this NO_X desorption step.

The responses of the deactivated materials to sulfur poisoning were also examined by exposing them to alternating SO_X poisoning atmospheres (S-AL for 120 s and S-AR for 3 s, compositions as in Table 2) at 400 ˚C for 41 min. The total sulfur amount introduced to the material during these treatments was 1.5 g/L. Following this exposure, the materials were cooled to 150 ˚C under the lean pretreatment gas composition indicated in Table 2, after which they were heated to 650 ˚C at a rate of 20 ˚C/min under the SO_X desorption gas conditions indicated in Table 2, to investigate their desulfation characteristics. Following such desulfation treatment, the material specimens were referred to as sulfur-aged materials.

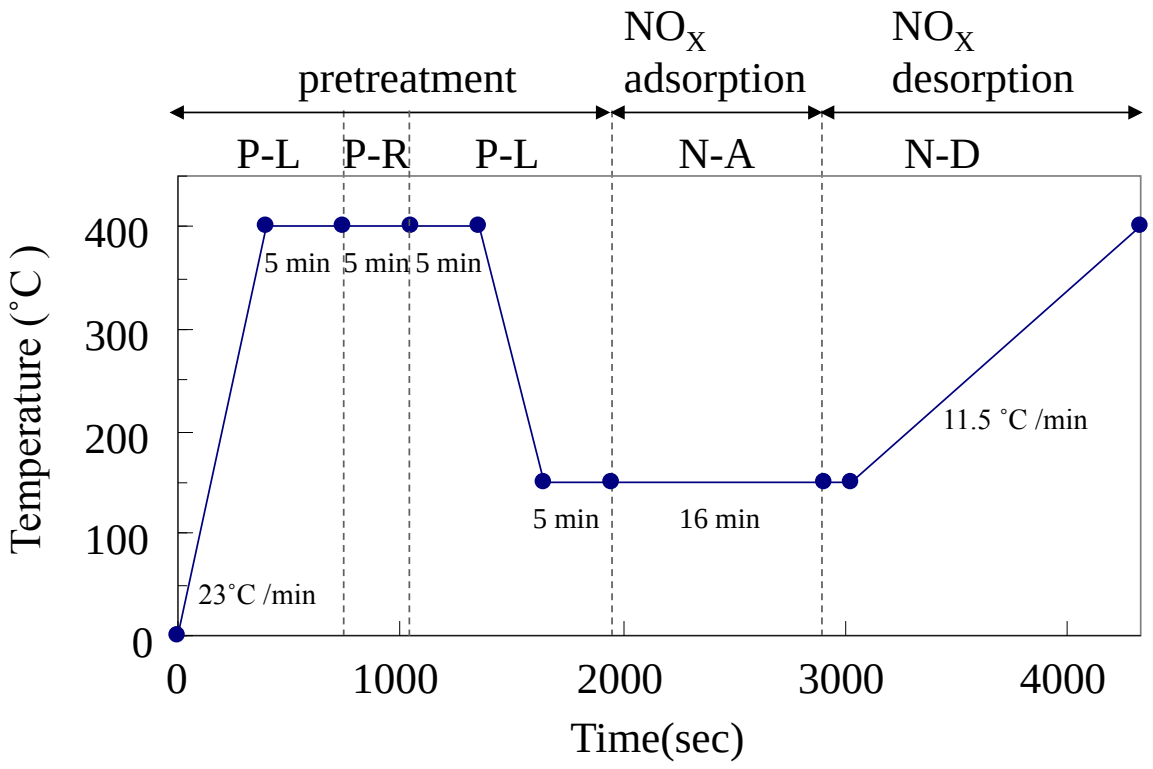

Fig. 2. Treatment process for the evaluation of catalyst performance.

2.3. Analysis of adsorbed NO_X

Adsorbed species on the surfaces of the NO_X trapping materials were determined by Fourier transform infrared (FT-IR) spectroscopy. FT-IR spectra were recorded on a Nicolet NEXUS670 using a diffuse reflectance attachment (DRIFTS). Material powder scraped from the monolithic specimens was set in the DRIFTS reactor cell and pretreated under a 200 cc/min N_2 flow at 400 ˚C for 15 min. Baseline spectra were then recorded at temperatures from 400 to 150 ˚C in 50 ˚C intervals. The IR spectrum of the NO_X trapping materials after exposure to a mixture of 0.2 % NO and 10 % O_2 in N_2 at 150 ˚C for 20 min were then recorded. Subsequently, IR spectra of the NO_X trapping materials during a desorption procedure under 200 cc/min N_2 flow were acquired between 150 and 400 ˚C. The IR spectra of adsorbed species were evaluated by subtracting the earlier baseline spectra from the spectra after NO_X adsorption at each temperature. For all IR measurements, the number of scans and the resolution were 500 and 4 cm^{-1}, respectively.

2.4. Characterization of materials

The NO_X trapping materials were characterized by transmission electron microscopy - energy dispersive X-ray (TEM-EDX) analyses, X-ray diffraction (XRD), near edge X-Ray absorption fine structure (NEXAFS) spectroscopy, UV-visible spectroscopy, CO-O_2 pulsed reaction and CO_2 temperature programmed desorption (CO_2-TPD) in order to examine factors which might influence their performance.

XRD patterns of Ag/A-2 and AgTi/A-8 were recorded using an X-ray diffractometer (Cu-Kα λ = 1.5418 Å, 40 kV, 30 mA) (Rigaku, RINT-1500V) to clarify the structure of Ag and TiO_2. Material powder scraped from the coating layer on sulfur-aged monolithic samples was pressed into wafers and affixed to standard microscope slides. The sizes of the Ag particles were calculated from the diffraction lines of Ag (111), Ag (200),

Ag (311) and Ag (222) using Scherrer's formula.

The chemical bonding states of Ag and Al in Ag/A-2 and AgTi/A-8 following sulfur exposure were analyzed using XPS spectroscopy (Mg-Kα radiation) (PHI, PHI-5500MC) to clarify the structure of Ag. The diameter of the XPS analysis area was approximately 1 mm at a depth of 2-3 nm.

Field-emission-transmission electron microscopy (FE-TEM) and energy dispersive X-ray analysis (EDX) were performed to analyze the distribution of the supported Ag as well as the Ag, Ti and Al contents of Ag/A-2 and AgTi/A-8, using a Hitachi HF-2000. The diameter of the EDX analysis area was approximately 10 nm.

NEXAFS spectroscopy was applied to the analysis of TiO_2 surface structures on AgTi/A-5, as well as to some references samples, such as rutile TiO_2, anatase TiO_2 and $BaTiO_3$. Powder scraped from the coating layer of the monolithic sample was formed into a plate shape and NEXAFS spectra were acquired in the sample current mode under ultra-low vacuum conditions (between 10^{-8} and 10^{-9} torr) using the BL-12 beam line at SAGA-LS (Kyushu Synchrotron Light Research Center).

UV-vis spectra were recorded under ambient conditions using a Nippon Bunko V-560-DS spectrometer in the diffuse reflectance mode over 200 - 850 nm at 0.5 nm intervals with a 2 nm bandwidth. Powder scraped from the coating layer of sulfur-aged monolithic Ag/A-1 and AgTi/A-5 was pretreated under 5 % O_2/N_2, 5 % H_2/N_2 and N_2 at 500 ˚C and then affixed to a $BaSO_4$ support. A background $BaSO_4$ spectrum was subtracted from each sample spectrum.

The quantity of active oxygen species in each NO_X trapping material was measured using a conventional fixed-bed flow reactor attached to the gas exhaust evaluation system (Best Sokki Bex-5900, CATA-5000) noted earlier. The monolithic AgTi/A-5, Ag/A-1 and Al_2O_3 were exposed to gas mixtures, cycling between 1 % CO/N_2 (80 s) and 1% O_2/N_2 (40 sec) for 60 min at 150 ˚C, and the resulting concentration of CO_2 was measured during these cycles. The amount of CO_2 produced during this process was

considered to represent the quantity of active oxygen in the material.

CO_2 adsorption properties of AgTi/A-5, Ag/A-1 and Al_2O_3 were determined using TPD on a conventional fixed-bed flow reactor noted earlier. After pretreatment with 10 % O_2/N_2 at 5 L/min and CO_2 exposure via 1 % CO_2/N_2 at 5 L/min, the desorbed CO_2 concentration was measured under a N_2 flow of 5 L/min during TPD at 10 ˚C/min. The adsorbed CO_2 data acquired in this manner was used to better understand the basic characteristics of the materials and to examine the extent of poisoning caused by CO_2.

2.5. DFT calculations

Calculations were based on density functional theory (DFT), using the Quantum ESPRESSO suite of codes [34]. For integration in the reciprocal space, a converged energy was achieved using a *k*-point grid of 0.05 $Å^{-1}$. Ultrasoft pseudo potentials were used to describe the ion-electron interactions. The crystalline orbitals were expanded in a set of plane waves limited by a kinetic energy cut-off of 30 Ry, which converged the energies to approximately 1.0 meV. The generalized gradient approximation (GGA) with the Perdew-Burke-Ernzerhof (PBE) parameterization was utilized for the exchange correlation part of the energy function [35].

3. Results and discussions

3.1. NO_X trapping performance

The quantities of NO_X adsorbed on the Ag/Al_2O_3 at 150 ˚C following exposure to the NO or NO_2 gas mixtures (compositions N-A1 or N-A2 as in Table 2) are shown in Table 3. Significantly greater adsorption was obtained during NO_2 exposure as compared

to NO exposure. These results demonstrate that, under low temperature conditions, the proportion of NO_2 in the exhaust is an important factor with regard to the level of NO_X adsorption on the Ag material, as has been reported previously for NSR systems. Accordingly, as noted earlier, it would be beneficial to improve the material's adsorption efficiency for NO in the presence of other gases, especially since NO makes up a larger proportion of exhaust gas than NO_2 does.

Table 3. Amounts of NO_X adsorbed on Ag/Al_2O_3.

Gas condition	Adsorbed NO_X amount (mg/L as NO_2)
N-A1 (NO inlet)	60.7
N-A2 (NO_2 inlet)	318.4

Fig. 3 presents a plot of the amounts of NO_X adsorbed on $Ag/Ti/Al_2O_3$ materials at 150 ˚C as a function of the amount of added TiO_2, as well as adsorption results for an NSR catalyst and for pure Ti/A, for reference purposes. In these trials, in which the material was exposed to NO mixed with other gases such as CO_2, CO, HC and O_2, the amount of NO_X adsorbed increased with increasing TiO_2 contents, reaching a maximum at 0.5 mol/L TiO_2 in the case of 0.24 mol/L Ag loading samples. The addition of TiO_2 was effective for NO adsorption in both cases of 0.24 mol/L and 0.4 mol/L Ag loading samples. This level of adsorption corresponds to approximately six times that of the NSR catalyst. These results show that the utilization of $Ag/Ti/Al_2O_3$ as an NO_X trapping material is an effective means of reducing NO_X at low temperatures. In addition, the Ag-free sample (Ti/A) did not show any activity, indicating that the Ag particles work as active sites. For each $Ag/Ti/Al_2O_3$ material, the desorbed NO_X amount is very nearly the same as the adsorbed amount, demonstrating selective NO_X reduction during the NO_X adsorption step and the reduction of adsorbed NO_X during both the adsorption step and the desorption stages over the

$Ag/Ti/Al_2O_3$ did not occur. As noted in the introduction, the decrease of NO_X in exhaust requires a hybrid system in which the reducing catalyst is located downstream of the NO_X trap incorporating $Ag/Ti/Al_2O_3$. In previous work [15, 16], the effect of a combined system incorporating a low temperature NO_X trap has been already confirmed, using Ag along with the reduction catalyst to improve the decrease of NO_X at temperatures under 150 ˚C.

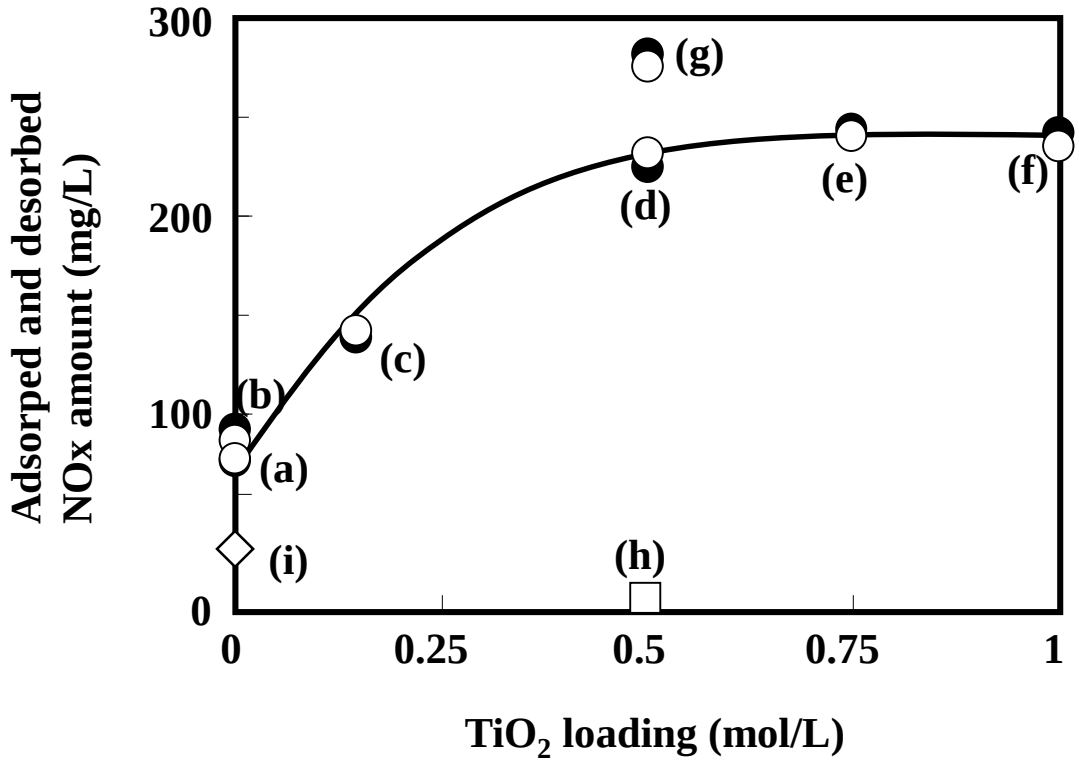

Fig. 3. Effects of TiO_2 addition on NO_X trapping performance at 150 ºC (following 750 ˚C aging) of (a) and (b) Ag/Al_2O_3 (Ag/A-1, 2), (c) - (g) $Ag/Ti/Al_2O_3$ (AgTi/A-3, 5, 6, 7, 9), (h) Ti/Al_2O_3 (Ti/A) and (i) NSR (BaKLi/Pt/A). ○, □ and ♢: quantity of NO_X adsorbed at 150 ˚C , ●: quantity of NO_X desorbed during TPD up to 400 ºC. Feed gas for NO_X adsorption: NO (100 ppm), O_2 (10%), CO_2 (10%), CO (800 ppm), C_3H_6 (400 ppm C) and H_2O (5%), SV=25,700 h^{-1}.

The influence of TiO_2 addition on the material's SO_X desorption properties was subsequently examined. Fig. 4 plots the SO_X desorption peak temperature during TPD following SO_2 (1.5 g/L) poisoning at 400 °C using simulated exhaust mixtures. Fig. 5 presents the concentrations of desorbed SO_X obtained from Ag/Al_2O_3, $Ag/Ti/Al_2O_3$ and NSR during SO_X TPD after sulfur poisoning.

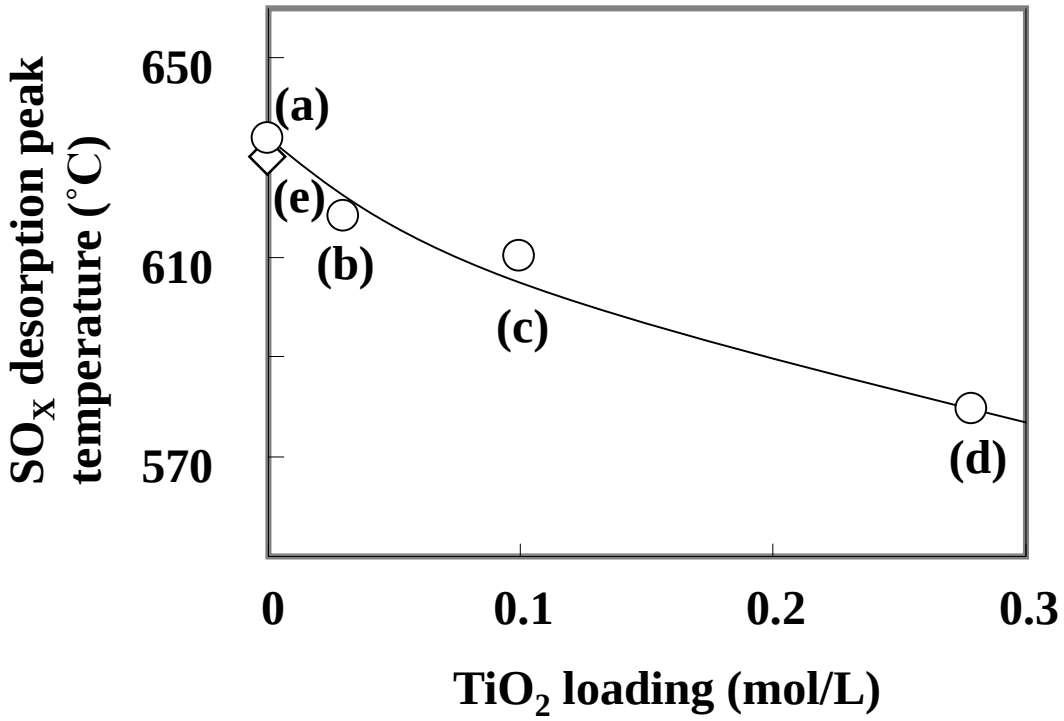

Fig. 4. SO_X desorption following SO_2 poisoning (1.5 g/L) of (a) Ag/Al_2O_3 (Ag/A-1), (b)-(d) $Ag/Ti/Al_2O_3$ (AgTi/A-1, 2, 4) and (e) NSR (BaKLi/Pt/A). Feed gas for sulfur desorption: O_2 (0.1%), CO_2 (10%), C_3H_6 (0.2% C), CO_2 (10%) and H_2O (5%), SV = 51,400 h^{-1}.

The SO_X desorption temperature is seen to decrease with increasing TiO_2 content, such that the use of $Ag/Ti/Al_2O_3$ lowers the SO_X desorption temperature by approximately 50 ˚C. It has already been reported that the addition of TiO_2 to NSR catalysts incorporating alkali or alkaline earth metals such as Ba and K is effective at improving low temperature sulfur desorption during the decomposition of sulfate and the release of the resulting

decomposition products, and similar effects were observed in our work with Ag-based materials. Fig. 6 shows the extent of NO_X adsorption by the Ag/Al_2O_3 and $Ag/Ti/Al_2O_3$ materials following thermal aging, sulfur poisoning and sulfur regeneration by TPD. Although the adsorption of NO_X decreased significantly following sulfur poisoning, it increased back to its original level following regeneration via TPD at 650 ˚C. From these results, it is evident that TiO_2 modification promotes sulfur desorption which in turn leads to the recovery of NO_X adsorption characteristics at low temperatures.

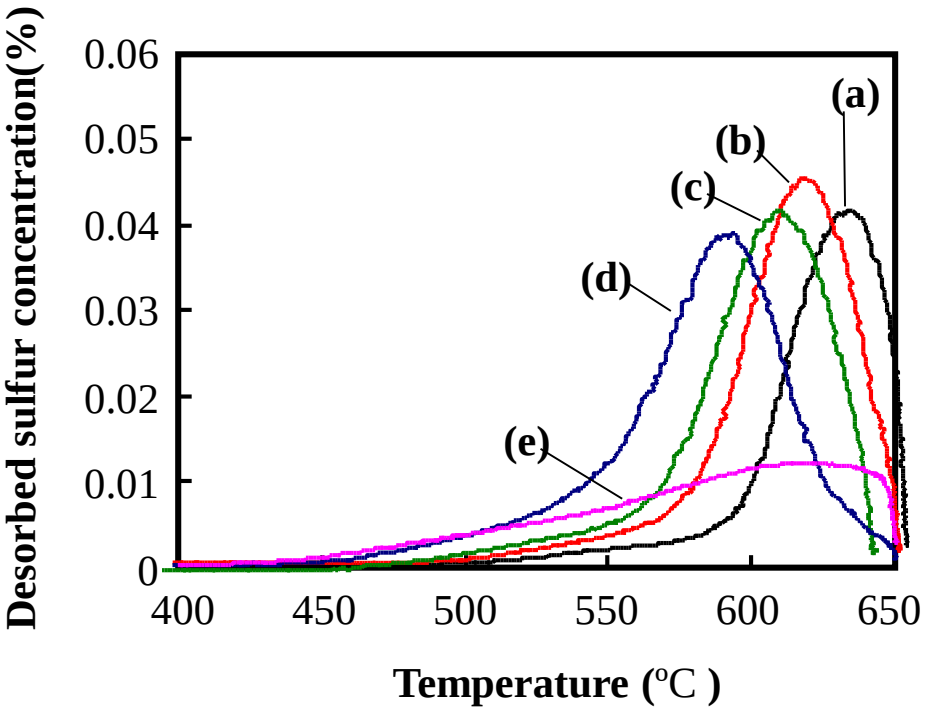

Fig. 5. SO_X desorption profiles following SO_2 poisoning (1.5 g/L) of (a) Ag/Al_2O_3 (Ag/A-1), (b)-(d) $Ag/Ti/Al_2O_3$ (AgTi/A-1, 2, 4) and (e) NSR (BaKLi/Pt/A). Feed gas for sulfur desorption: O_2 (0.1%), CO_2 (10%), C_3H_6 (0.2% C) and H_2O (5%), SV = 51,400 h^{-1}.

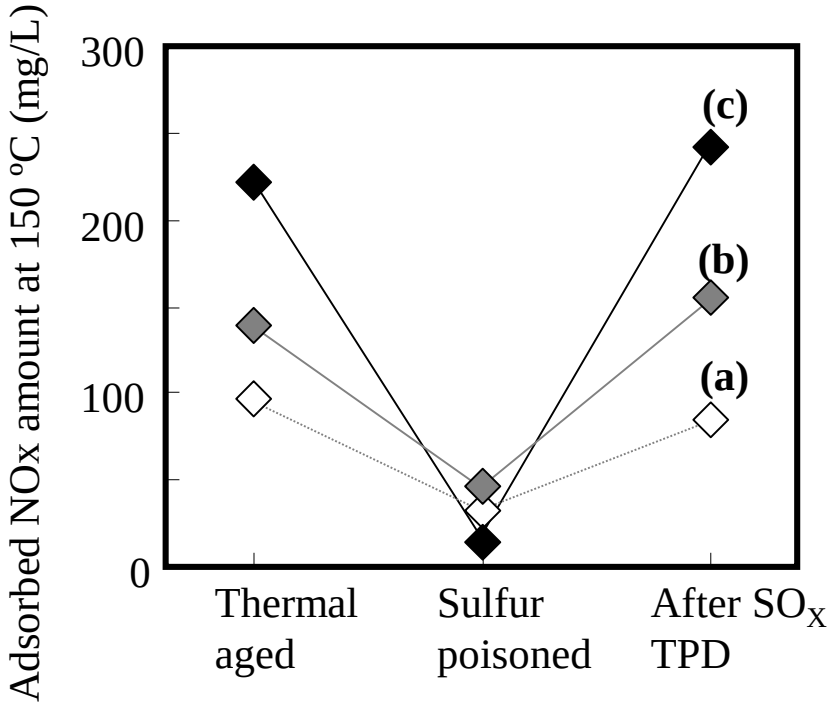

Fig. 6. The effects of sulfur poisoning and regeneration on NO_X adsorption of (a) Ag/Al_2O_3 (Ag/A-1), (b) and (c) $Ag/Ti/Al_2O_3$ (AgTi/A-3, 5). Feed gas for NO_X adsorption: NO (100 ppm), O_2 (10%), CO_2 (10%), CO (800 ppm), C_3H_6 (400 ppm C) and H_2O (5%), SV=25,700 h^{-1}.

3.2. States of adsorbed NO_X

Fig. 7 shows the IR spectra of adsorbed NO_X species on sulfur-aged $Ag/Ti/Al_2O_3$ and Ag/Al_2O_3, in which NO_2^- and NO_3^- bands are shown based on previous reports [21]. Characteristic peaks attributed to an oxidized NO species are seen in the region below 1650 cm^{-1}, and there are no peaks corresponding to adsorbed NO above 1800 cm^{-1}. These results indicate that all NO has reacted with oxygen and been converted to nitro ($-NO_2$), nitrite (-ONO) or nitrate ($-ONO_2$) species. In the case of the $Ag/Ti/Al_2O_3$, the region from

1300 to 1500 cm^{-1} assigned to nitro and nitrite species exhibits more prominent peaks as compared to the Ag/Al_2O_3. These bands were observed to rapidly decrease during stepwise temperature programmed desorption of the material, and therefore it is believed that the higher proportion of adsorbed nitro and nitrite species on $Ag/Ti/Al_2O_3$ as compared Ag/Al_2O_3 produces an advantage in terms of NO_X desorption.

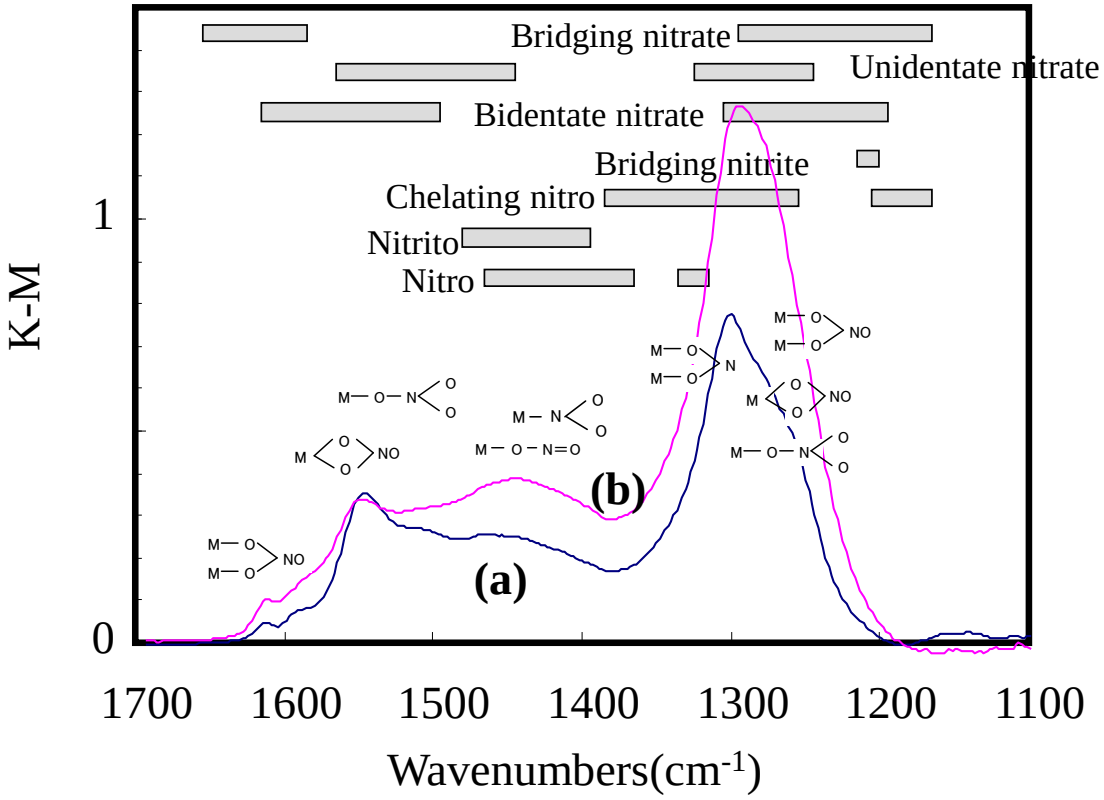

Fig. 7. IR spectra following NO_X adsorption at 150 ºC on (a) Ag/Al_2O_3 (Ag/A-1) and (b) $Ag/Ti/Al_2O_3$ (AgTi/A-3) following 750 ºC sulfur aging. Feed gas: NO (10%) and O_2 (10%) at 150 ˚C followed by N_2 purge.

3.3. Characterization of the NO_X trapping material

Fig. 8 shows the XRD patterns of Ag/Al_2O_3 and $Ag/Ti/Al_2O_3$ after sulfur aging, in which diffraction lines attributed to Ag, Al_2O_3 and cordierite (as an impurity) are denoted. There is no diffraction line associated with TiO_2 compounds in the $Ag/Ti/Al_2O_3$, which provides evidence that the Ti species were both highly dispersed and not in a crystalline state. The average sizes of the Ag particles in Ag/Al_2O_3 and $Ag/Ti/Al_2O_3$ were calculated using the half widths of several Ag diffraction lines, and are given in Table 4. From these results, it was determined that the Ag particles in $Ag/Ti/Al_2O_3$ are smaller than in Ag/Al_2O_3.

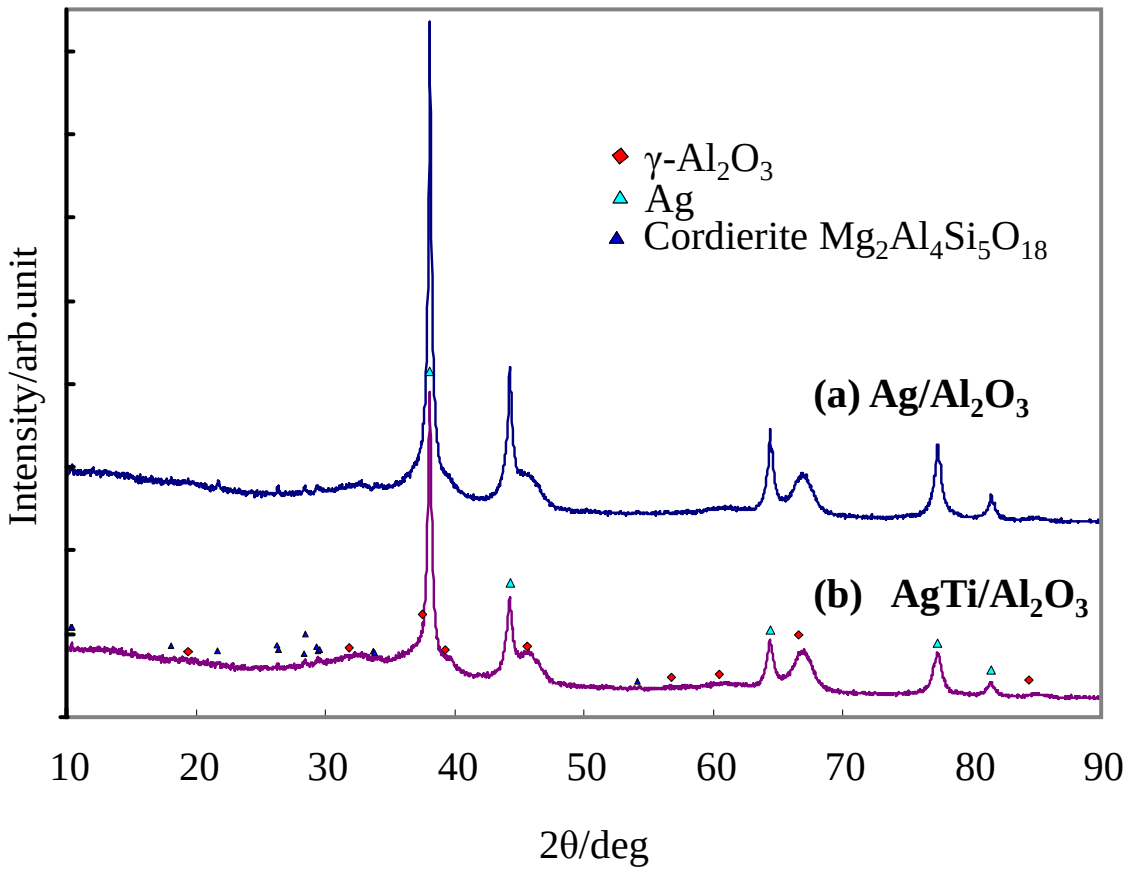

Fig. 8. XRD profiles of (a) Ag/Al_2O_3 (Ag/Al-2) and (b) $Ag/Ti/Al_2O_3$ (AgTi/A-8) after sulfur aging.

Table 4. Ag particle sizes as estimated by XRD and XPS.

catalyst	Ag particle size (nm)	
	by XRD	by XPS
Ag/Al_2O_3 [a]	27.5	4.2
$Ag/Ti/Al_2O_3$ [b]	18.7	0.8

[a] Ag/A-2.
[b] AgTi/A-8.

XPS measurements were performed for both Ag/Al_2O_3 and $Ag/Ti/Al_2O_3$. Generally, it is difficult to identify the oxidation state of Ag from its XPS peak position because the chemical bond energies of Ag metal and Ag_2O have very similar values (368.3 and 367.5 eV, respectively). However, we were able to estimate the size of the Ag particles dispersed in the material to a depth of 2 - 3 nm using the ratio of the XPS peak heights of Ag and Al in the support, applying the equation provided as Scheme 1. In this equation, d is the particle size of Ag, I is the XPS peak intensity, a is the atomic volume density, λ is the average depth of the photoelectrons analyzed, w is the weight ratio of Ag in the support, S_A is the specific surface area of the support, ρ is density and the subscripts m and s refer to Ag and the support respectively.

$$I_m / I_s = \frac{a_m \lambda_m}{a_s \lambda_s} \frac{w}{S_A \rho_m d} \left(1 - \exp\left(-d/\lambda_m\right)\right) \qquad \text{- Scheme 1}$$

The Ag particle sizes calculated using Scheme 1 are presented in Table 4 along with sizes determined via XRD analysis. It can be seen that the particle sizes estimated by XPS are substantially smaller than those obtained by XRD, especially in the case of $Ag/Ti/Al_2O_3$, suggesting the existence of highly dispersed Ag particles on the surface of

the TiO_2-modified Al_2O_3.

TEM images of Ag/Al_2O_3 and $Ag/Ti/Al_2O_3$ after sulfur aging are shown in Fig. 9. In both samples, black particles 5-20 nm in diameter are observed, which are identified as Ag. It is also evident that the Ag particles in $Ag/Ti/Al_2O_3$ are generally smaller than those in Ag/Al_2O_3. In order to clarify the distribution of Ag and Ti on the Al_2O_3, random locations on the primary Al_2O_3 particles (at which there were no black Ag particles present) were examined using EDX at the nm scale. The Ag and Ti compositions determined in this manner are summarized in Table 5. Both Ag and Ti were detected on the $Ag/Ti/Al_2O_3$, and its Ag content was higher than that of Ag/Al_2O_3 at the locations measured. These results indicate that, in the case of $Ag/Ti/Al_2O_3$, both Ag and Ti are homogeneously dispersed over the Al_2O_3.

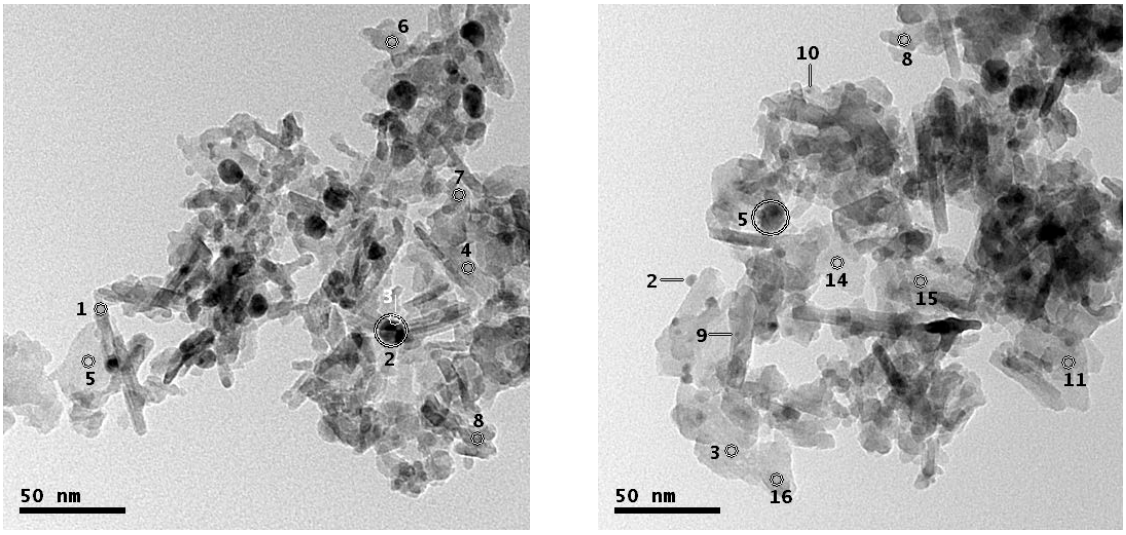

(a)Ag/Al_2O_3 (b)$Ag/Ti/Al_2O_3$

Fig. 9. FE-TEM images of (a) Ag/Al_2O_3 (Ag/A-2) and (b) $Ag/Ti/Al_2O_3$ (AgTi/A-8) after 750 ˚C aging. Numbers indicate areas where the composition was determined by EDX.

Table 5. Ag and Ti contents as determined by TEM-EDX.

Material	Ag (mol%)		Ti (mol%)	
	EDX analysis at the nm-scale area where Ag particle not observed	Average value as prepared	EDX analysis at the nm-scale area where Ag particle not observed	Average value as prepared
Ag/Al_2O_3 [a]	0.5	9.3	-	-
$Ag/Ti/Al_2O_3$ [b]	1.5	8.7	3.3	5.9

[a] Ag/A-2.
[b] AgTi/A-8.

The structure of the surface Ti species was analyzed by NEXAFS, which can provide more information about the local structure of a species on a support than either XPS or XRD. The local surface structure of TiO_2 on $Ag/Ti/Al_2O_3$ was compared with that of standard oxides such as a rutile TiO_2, an anatase TiO_2 and a $BaTiO_3$, all of which have differing structures. Fig. 10 shows $L_{3,2}$-NEXAFS data for aged $Ag/Ti/Al_2O_3$ as well as the reference oxides.

Previously reported theoretically simulated NEXAFS results for TiO_2 in an octahedral environment, as well as experimental results obtained from bulk samples of rutile and anatase, were used to interpret our NEXAFS spectra [36 - 39]. In an octahedral environment such as $BaTiO_3$, there will be two series of sharp resonance bands, denoted in the figure as a1, a2 and b1, b2, for the apparent L_3 and L_2 edges, respectively. However, in rutile and anatase, two common TiO_2 crystal structures result from a tetragonal distortion of Oh symmetry. This tetragonal distortion produces differences in local symmetry at the Ti site for these structures and further splits the second peak of the L_3 resonance (a2) into a2' and a2''. These two structures can therefore be distinguished by the relative intensities of the doublet a2' and a2'' peaks, such that a2' > a2'' in anatase and a2' < a2'' in rutile. In Fig. 10, it can be seen that the spectrum of $Ag/Ti/Al_2O_3$ most closely resembles that of $BaTiO_3$, which has no peak splitting peak at the a2' and a2'' positions. Accordingly, Ti species located on the surface of $Ag/Ti/Al_2O_3$ exist in local structures corresponding to

octahedral TiO_2, which is different from the structure of both anatase and rutile. In this octahedral structure, the Ti-O bond length is longer than in the other possible structures.

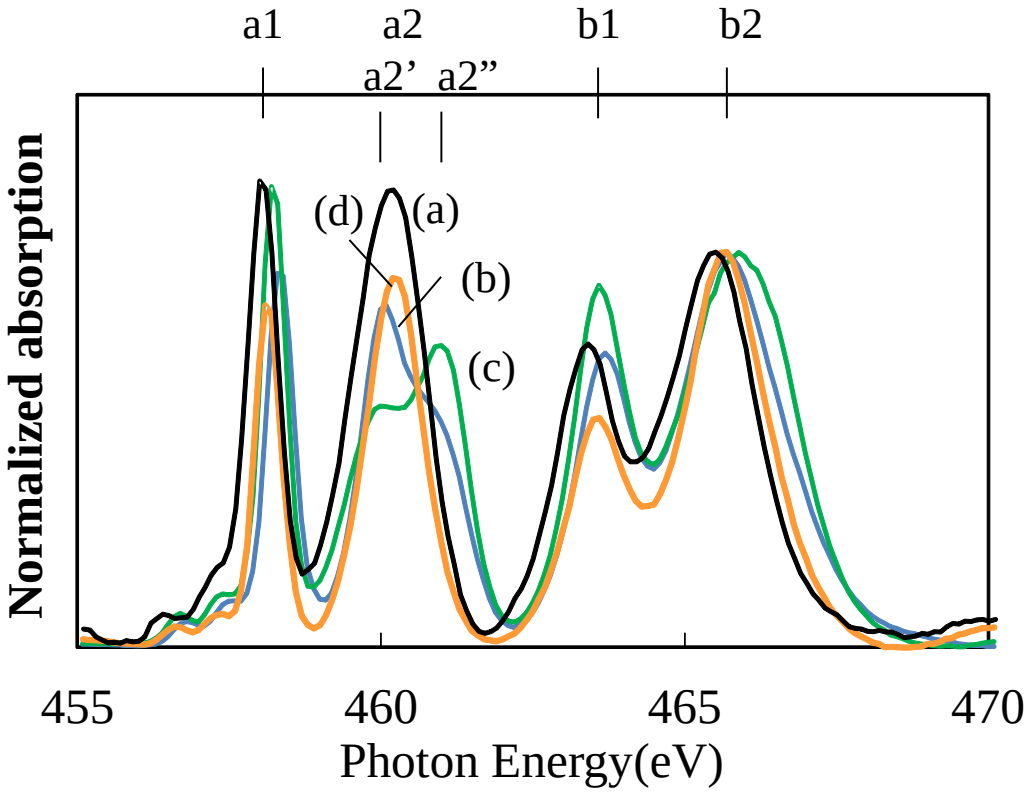

Fig. 10. $L_{3,2}$-NEXAFS of (a) sulfur-aged $Ag/Ti/Al_2O_3$ (AgTi/A-5) and reference oxides (b) anatase, (c) rutile and (d) $BaTiO_3$.

We believe that the unique interaction between Ag and TiO_2 in the material results from this structure, which can be considered the cause of the significant dispersion of Ag throughout the $Ag/Ti/Al_2O_3$. Further information about the TiO_2 was obtained from the calcination of aqueous solutions of Ti with citric acid, following which TiO_2 was found to exist in an anatase-type structure. It is therefore considered that TiO_2 prepared via impregnation with a mixture of Ti and citric acid forms highly dispersed octahedral structures on the Al_2O_3 and that this TiO_2/Al_2O_3 works as a favorable support for Ag. Based on our data for Ti loading and the specific surface area of the Al_2O_3 supports, the

quantity of Ti particles on the surface of $Ag/Ti/Al_2O_3$ (AgTi/A-5) was estimated to be 8.9 per nm^2, which corresponds to 93 % of the theoretical TiO_2 dispersion over an Al_2O_3 monolayer. Therefore, TiO_2 appears to be dispersed in a form similar to that of a monolayer on the $Ag/Ti/Al_2O_3$ material surface, with no crystalline regions.

The stability of silver on TiO_2 was examined by modeling simulations based on DFT calculations. The (*hkl*) surface was simulated using a slab model; the slabs in the (*hkl*) crystallographic direction were generated with a vacuum thickness of at least 12 Å. To examine the stability of silver on anatase (001), rutile (110), octahedral TiO_2 and γ-Al_2O_3 (001), various surface structures were cut off from crystal structures [40, 41]. A potentially suitable support structure of octahedral TiO_2 was modeled as a monolayer surface structure on γ-Al_2O_3 (001) [41]. The clean surface showed relaxation and reconstruction in the surface layer, which was analogous to anatase TiO_2 (001) surface structure. We investigated a single Ag adatom on the several surface using DFT method with full-geometry optimization to locate the most stable configuration, changing initial position of a single Ag adatom. The relative stability of silver on octahedral TiO_2-modified alumina was compared with that on other surfaces, with the results shown in Table 6, which demonstrates that Ag on octahedral TiO_2/Al_2O_3 is better stabilized than on the other surfaces. Diagrams of the structure for octahedral TiO_2-modified γ-Al_2O_3 as well as Ag supported on this structure are provided in Fig. 11. It was determined that Ag is most stable at the location corresponding to the A site in the ABO_3 perovskite structure. We believe that this is the primary factor leading to improved Ag dispersion on TiO_2-modified alumina.

Table 6. Relative stability of Ag atoms on various surfaces (eV) .

Oct-TiO_2 / γ-Al_2O_3	anatase	rutile	γ-Al_2O_3
1.39	1.30	0.22	0.00

Quantum Espresso 5.0, cutoff: 30Ry, k-grids: 2 × 2 × 1

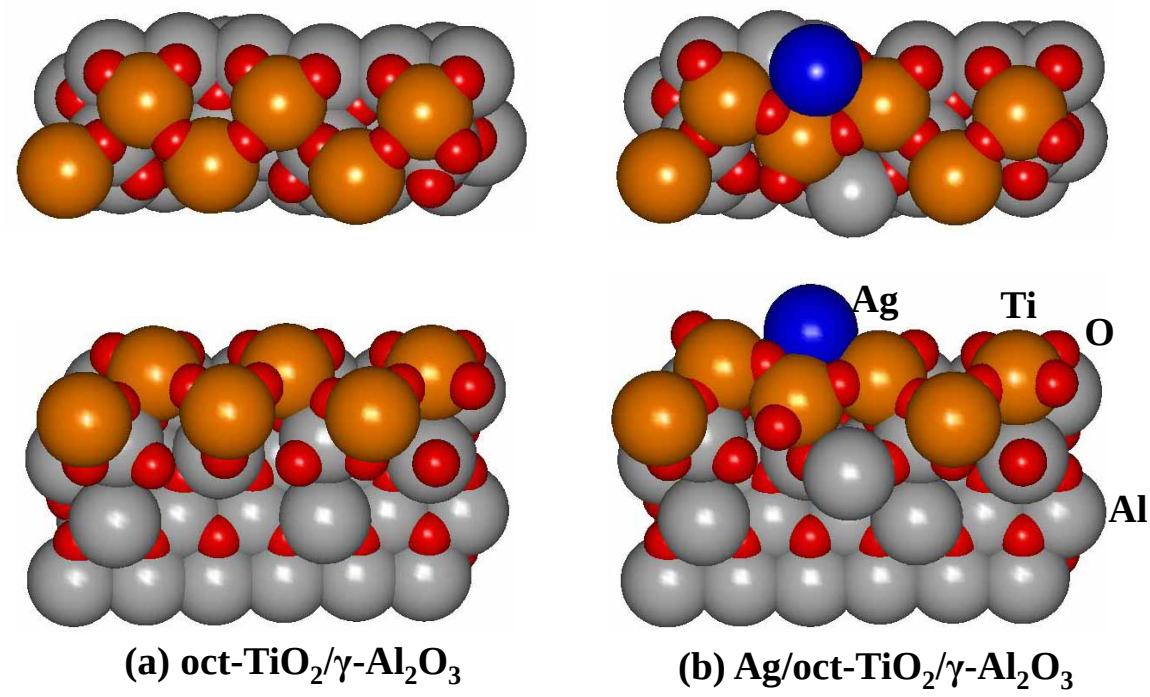

Fig. 11. Modeled simulations of Ag supported on octahedral TiO_2-modified γ-Al_2O_3.

Table 7. Chemical properties of NO_X trapping materials.

catalyst	Active oxygen amount mmol/L	Desorbed CO_2 amount mmol/L
$Ag/Ti/Al_2O_3$ [a]	13.1	3.2
Ag/Al_2O_3 [b]	6.9	9.1
Al_2O_3	0.7	7.6

[a] Tested catalyst: AgTi/A-5.
[b] Tested catalyst: Ag/A-1.

The modification of the material's chemical properties by the incorporation of TiO_2 was subsequently examined.

The quantities of active oxygen species on $Ag/Ti/Al_2O_3$, Ag/Al_2O_3 and Al_2O_3

were measured at 150 ˚C with the results indicated in Table 7. In the CO-O_2 pulsed reaction technique, CO_2 is primarily desorbed immediately after CO dosing and reaction with active oxygen species in the material. The amount of desorbed CO_2 was therefore used to calculate the quantity of active oxygen species (leftmost column in Table 7). The data show that, in the case of Al_2O_3, the amount of desorbed CO_2 was considerably lower than that observed for the Ag-containing samples. This shows that the active oxygen species which result in the formation of CO_2 come either from the Ag surface or the interface around the Ag. It was also determined that CO_2 desorption from Ag/Ti/Al_2O_3 was approximately twice that of Ag/Al_2O_3 and that, based on the number of Ag atoms on Ag/Ti/Al_2O_3, the concentration of active oxygen species in this material corresponded to 5.4 %. Therefore, it appears that active oxygen species capable of reacting at temperatures as low as 150 °C are present on the surface of Ag/Ti/Al_2O_3, in the vicinity of Ag particles, and serve to promote the production of NO_2^- and NO_3^- by NO oxidation, as well as the elimination of CO by oxidation. This property is assumed to be the cause of the high NO_X adsorption capacity exhibited by this material at low temperatures. Furthermore, it is assumed that TiO_2 modification of the material enhances this effect by promoting dispersion of the Ag throughout the material. Increased quantities of active Ag-O sites resulting from improved Ag dispersion are considered to be the reason for this material's superior low temperature NO_X adsorption characteristics.

UV-vis spectra of Ag/Ti/Al_2O_3 after various pretreatments are presented in Fig. 12 along with that of Ag/Al_2O_3. Many research studies [37, 42 - 44] have reported the UV-vis spectra of Al_2O_3-supported Ag materials, and the band at approximately 215 nm has been attributed to the transition from $4d^{10}$ to $4d^95s^1$ of highly dispersed Ag^+, while the band around 275 nm is attributed to $Ag^{\delta+}$ clusters and the broad band around 450 nm to metallic Ag clusters and aggregates. In this figure, the absorption band assigned to Ag^0 is seen in the region between 400 and 600 nm in the case of both Ag/Al_2O_3 and Ag/Ti/Al_2O_3. The redox pretreatment is seen to strongly affect the absorbance in this region in both cases.

The relative change in the absorbance of $Ag/Ti/Al_2O_3$ is greater than that of Ag/Al_2O_3, likely because TiO_2 modification makes is easier for the reaction between Ag-O and Ag^0 to proceed.

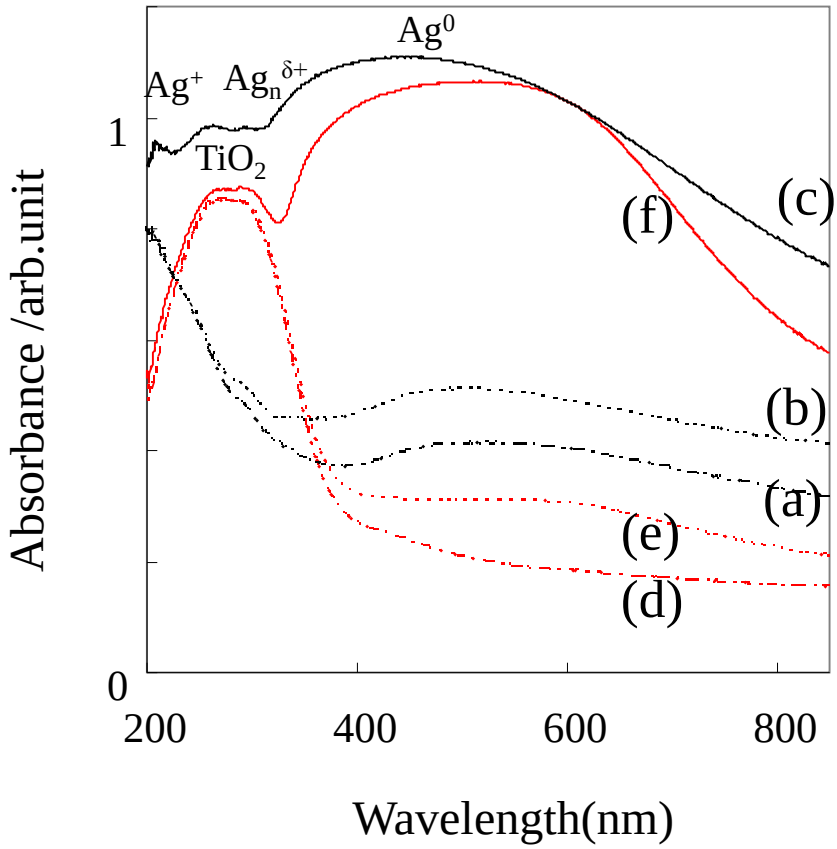

Fig. 12. UV-vis spectra of (a)-(c) Ag/Al_2O_3 (Ag/A-1), (d)-(f) $Ag/Ti/Al_2O_3$ (AgTi/A-5) following redox treatment. Conditions: (a) and (d): oxidizing gas (10% O_2/N_2), (b) and (e): inert gas (N_2), (c) and (f): reducing gas (5% H_2/N_2).

The amounts of desorbed CO_2 as measured by CO_2-TPD are indicated in Table 7, from which it is evident that the CO_2 desorbed from $Ag/Ti/Al_2O_3$ was lower than that desorbed from either Ag/Al_2O_3 or Al_2O_3. These data indicate that Ag works as an adsorption site for CO_2 but that, on $Ag/Ti/Al_2O_3$, the amount of adsorbed CO_2 was lessened

compared to Ag/Al_2O_3. It is deduced that TiO_2 modification has the effect of blocking the basic sites on Al_2O_3, leading to decreased CO_2 poisoning and promoting redox reactions involving the Ag.

3.4. The reaction mechanism associated with NO_X trapping

Fig. 13 presents a proposed reaction mechanism for the low temperature NO_X trapping, based on the above analyses.

On an Al_2O_3 support, finely dispersed Ag particles combined with octahedral TiO_2 are present on the nm scale, in addition to larger Ag particles over 10 nm in size. Ag works not only as an oxidation catalyst, but also as an adsorption site for NO_X. The specific advantages of this system are that the redox reactions of Ag are able to proceed readily, and that poisoning by co-gases, such as CO_2 or SO_2, is reduced. We propose that the material surface is subsequently able to oxidize NO to NO_2 at low temperatures and effectively adsorb it in the form of nitrite and nitrate.

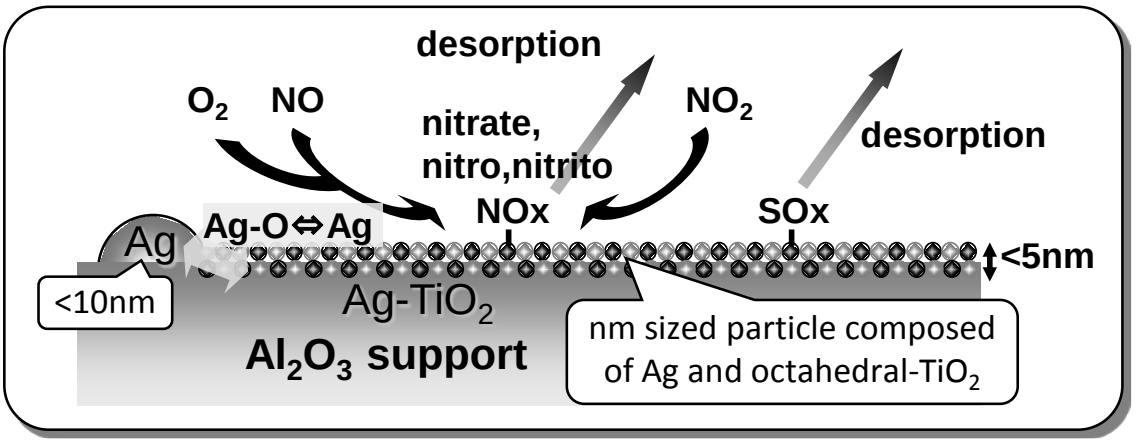

Fig. 13. Proposed mechanism for low temperature NO_X trapping over $Ag/Ti/Al_2O_3$.

The results of FT-IR spectroscopy concerning the NO_X adsorption state revealed that nitro and nitrite species produced by NO oxidation existed predominantly on $Ag/Ti/Al_2O_3$, which we believe is the reason for the high NO_X desorption exhibited by $Ag/Ti/Al_2O_3$. In addition, the $CO\text{-}O_2$ pulsed reaction data and UV-vis data revealed that the redox reactions of Ag proceed more readily on $Ag/Ti/Al_2O_3$ as compared to Ag/Al_2O_3. This property originates from the highly dispersed Ag particles on the TiO_2-modified Al_2O_3 surface, such that NO_X adsorption advantageously proceeds even at temperatures as low as 150 ˚C as a result of the improved oxidation performance. Further, CO_2-TPD clarified that TiO_2 modification can reduce the quantity of basic surface sites at which CO_2 poisoning occurs. These properties have the effect of reducing the influence of co-existing gases on NO_X adsorption. The main factor which confers these beneficial properties on $Ag/Ti/Al_2O_3$ is considered to be the presence of highly dispersed Ag particles combined with surface-dispersed TiO_2 in an octahedral-type local structure, as confirmed by NEXAFS. XRD and TEM have also confirmed the combination of dispersed Ag and TiO_2, while DFT calculations have shown that Ag can exist in a more stabilized form on octahedral TiO_2 on the Al_2O_3 surface. The highly dispersed TiO_2 present in the material may result from our method of preparing the material, based on using an aqueous solution of Ti and citric acid [30]. The resulting stable surface structure maintains a high degree of Ag dispersion by inhibiting the mobility of Ag atoms and also promotes the redox transition between Ag^0 and Ag^+. Finally, the ready access to both Ag and TiO_2 on the material surface promotes the decomposition of sulfate, which in turn increases the material's sulfur desorption ability. It is concluded that these structural modifications are the primary factors leading to improved low temperature NO_X adsorption under conditions where co-existing exhaust gases are present.

4. Conclusions

In this work, we examined the utilization of an NO_X trapping material as a means to improving the low temperature removal of NO_X from lean-burn automobile exhaust. We found that TiO_2-modified Ag-alumina ($Ag/Ti/Al_2O_3$), in which the Ag and TiO_2 are finely dispersed at the nm scale on an Al_2O_3 support, is effective as an NO_X trap. The use of $Ag/Ti/Al_2O_3$ increases the activity of the NO_X trapping sites and decreases poisoning by co-existing gases such as CO, CO_2, HC, SO_X and H_2O. Various analyses were applied to understand the mechanism of NO_X trapping on $Ag/Ti/Al_2O_3$. Ag was shown to exist in a stabilized form on a highly dispersed octahedral TiO_2 network on the Al_2O_3 support, based on the results of XPS, XRD, TEM and NEXAFS analyses as well as DFT calculations. The Ag in the material works as an active site at which the redox reaction between Ag^0 and Ag^+ occurs, as confirmed by UV-vis and $CO\text{-}O_2$ pulsed reaction studies. NO is oxidized on this active surface and subsequently adsorbed as nitro and nitrite species on the $Ag/Ti/Al_2O_3$. In addition, the combination of Ag on TiO_2 on the surface was effective at reducing poisoning and at the elimination of co-existing gases such as CO. It was concluded that the high performance of this material with regard to low temperature NO_X adsorption was brought about by a combination of the above mechanisms.

Acknowledgements

This work was supported by Toyota Motor Corporation. The authors acknowledge Hitachi High-Tech Manufacturing & Service Corp. for TEM analysis and Kyushu Synchrotron Light Research Center for NEXAFS spectroscopy. Authors would like to thank Y. Tsukamoto, N. Takagi and Y. Sobue at TMC, and K. Dohmae, N. Takahashi and Y. Kishida at Toyota Central Research and Development Labs., Inc. for technical

assistance and helpful discussions.

References

[1] F. Nakajima, I. Hamada, *Catal. Today* 29 (1996) 109-115.

[2] R. M. Heck, *Catal. Today* 53 (1999) 519-523.

[3] N. Miyoshi, S. Matsumoto, K. Katoh, T. Tanaka, J. Harada, N. Takahashi, K. Yokota, M. Sugiura, K. Kasahara, *SAE Tech. Paper*, 950809 (1995).

[4] N. Takahashi, H. Shinjoh, T. Iijima, T. Suzuki, K. Yamazaki, K. Yokota, H. Suzuki, N. Miyoshi, S. Matsumoto, T. Tanizawa, T. Tanaka, S. Tateishi, K. Kasahara, *Catal. Today* 27 (1996) 63-69.

[5] M. Iwamoto, H. Yahiro, Y. Yu-u, S. Shundo, N. Mizuno, *Shokubai (Catalyst)* 32 (1990) 430-433.

[6] T. Tanaka, T. Okuhara, M. Misono, *Appl. Catal. B* 4 (1994) L1-L9.

[7] T. Tanaka, K. Yokota, N. Isomura, H. Doi, M. Sugiura, *Appl. Catal. B* 16 (1998) 199-208.

[8] T. Tanaka, K. Yokota, H. Doi, M. Sugiura, *Chem. Lett.* 5 (1997) 409-410.

[9] K. Yokota, M. Fukui T. Tanaka, *Appl. Surf. Sci.* 121 (1997) 273-277.

[10] Japanese Patent No.3382361.

[11] Japanese Unexamined Patent Application Publication No. Hei 8-10575.

[12] Y. Reneme, F. Dhainaut, P. Granger, *Appl. Catal. B* 111 (2012) 424-434.

[13] M. Al-Harbi, W. S. Epling, *Catal. Lett.* 130 (2009) 121-129.

[14] Japanese Patent No. 3311370.

[15] Y. Tsukamoto, H. Nishioka, D. Imai, Y. Sobue, N. Takagi, T. Tanaka, T. Hamaguchi, *SAE paper* 2012-01-0370 (2012).

[16] T. Tanaka, T. Hamaguchi, C. Andoh, Y. Tsukamoto, N. Takagi, Y. Sobue, 7*th*

International Conference on Environmental Catalysis (2012Lyon), S06-T1-O-04.

[17] S. Hodjati, K. Vaezzadeh, C. Petit, V. Pitchon, A. Kiennemann, *Appl. Catal. B* 26 (2000) 5-16.

[18] G. Qi, W. Li, *Catal. Today* 184 (2012) 72-77.

[19] M. Machida, M. Uto, D. Kurogi, T. Kijima, *Chem. Mater.* 12 (2000) 3158-3164.

[20] J-Y. Luo, W. S. Epling, G. Qi, W. Li, *Catal. Lett.* 142 (2012) 946-958.

[21] J. Müslehiddinoğlu, M. Albert Vannice, *J. Catal.* 217 (2003) 442-456.

[22] K. A. Bethke, H. H. Kung, *J. Catal.* 172 (1997) 93-102.

[23] S. Satokawa, J. Shibata, K. Shimizu, A. Satsuma, T. Hattori, *Appl. Catal. B* 42 (2003) 179-186

[24] A. Keshavaraja, X. She, M. Flytzani-Stephanopoulos, *Appl. Catal. B* 27 (2000) L1-L9.

[25] K. Shimizu, J. Shibata, H. Yoshida, A. Satsuma, T. Hattori, *Appl. Catal. B* 30 (2001) 151-16.

[26] A. Sultana, M. Haneda, T. Fujitani, H. Hamada, *Catal. Lett.* 114 (2007) 96-102.

[27] S. Kameoka, T.Chafik, Y. Ukisu, T. Miyadera, *Catal. Lett.* 51 (1998) 11-14.

[28] U. Bentrup, M. Richter, R. Fricke, *Appl. Catal. B* 55 (2005) 213-220.

[29] A. Hellman, H. Grönbeck, *J. Phys. Chem. C* 113 (2009) 3674-3682.

[30] T. Tanaka, I. Tajima, Y. Kato, Y. Nishihara, H. Shinjoh, *Appl. Catal. B* 102 (2011) 620-626.

[31] H. Imagawa, T. Tanaka, N. Takahashi, S. Matsunaga, A. Suda, H. Shinjoh, *J. Catal.* 251 (2007) 315-320.

[32] I. S. Pieta, W. S. Epling, M. García-Diéguez, J. Y. Luo, M. A. Larrubia, M. C. Herrera, L. J. Alemany, *Catal. Today* 175 (2011) 55-64.

[33] T. Tanaka, K. Amano, K. Dohmae, N. Takahashi, H. Shinjoh, *Appl. Catal. A* 455 (2013) 16-24

[34] S. Baroni, A. D. Corso, S. de Gironcoil, P. Giannozzi, C. Cavazzoni, G. Ballabio, S.

Scandolo, G. Chiarotti, P. Focher, A. Pasquarello, K. Laasonen, A. Trave, R. Car, N. Marzari, A. Kokalj, Quntum-ESPRESSO; http://www/quantum-espresso.org.

[35] J. P. Perdew, K. Burke, M. Ernzerhof, *Phys. Rev. Lett.* 77 (1996) 3865-3868.

[36] J. G. Zhou, H. T. Fang, J. M. Maley, M. W. Murphy, J. Y. Peter Ko, J. N. Cutler, J. *Mater. Chem.* 19 (200) 6804-6809.

[37] M. Sánchez-Agudo, L. Soriano, C. Quiros, J. Avila, J. M. Sanz, *Surf. Sci.*, 482-485 (2001) 470-475.

[38] F. M. F. de Groot, J. C. Fuggle, B. T. Thole, G. A. Sawatzky, *Phys. Rev. B* 41 (1990) 928-937.

[39] G. S. Henderson, X. Liu, M. E. Fleet, *Phys. Chem. Miner.* 29 (2002) 32-42.

[40] WWW-MINCRYST; http://database.iem.ac.ru/mincryst/index/php.

[41] M. Digne, P. Raybaud, P. Euzen, H. Toulhoat, *J. Catal.* 226 (2004) 54-68.

[42] J. Lu, J. J. Bravo-Sua´rez, M. Haruta, S. T. Oyama, *Appl. Catal. A* 302 (2006) 283.

[43] N. Bogdanchikova, F. C. Meunier, M. Avalos-Borja, J. P. Breen, A. Pestryakov, *Appl. Catal. B* 36 (2002) 287-297.

[44] K. Sato, T. Yoshinari, Y. Kintaichi, *Appl. Catal. B* 44 (2003) 67-78.

[45] T. Tanaka, H. Hamaguchi, T. Murasaki, M. Watanabe, D. Imai, Japanese Patent No.05290062.

Chapter 8

General Conclusions

This work examined various NO_X purification catalysts, primarily SCR and NSR catalysts, operating under excess oxygen conditions. The reaction and deterioration mechanisms of these materials were analyzed and improvements related to the active catalytic centers were obtained, based on the results described below.

Investigations of the SCR reaction mechanism using C_3H_6 as a reducing gas on a Pt catalyst presented in Chapter 2 suggested that the reaction produces a nitrogen-containing intermediate which undergoes oxidative decomposition as indicated in Scheme 1.

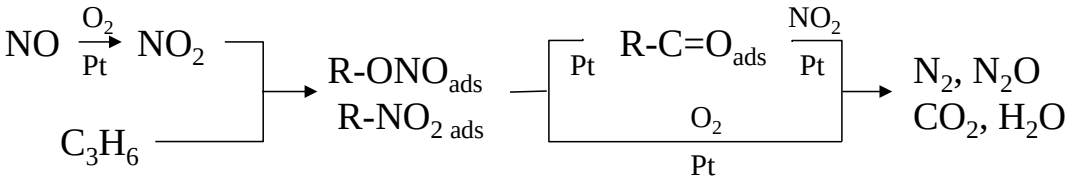

Scheme 1. A proposed reaction scheme for the selective reduction of NO in the presence of excess oxygen over Pt/SiO_2

It was determined that the reaction between NO_2 and this intermediate was a key step in the SCR system and the selectivity of this system for N_2 and N_2O was strongly affected by

the particular active centers formed by the Pt. Based on these results, modification of the Pt-based active centers is believed to be crucial to improving NO oxidation activity and controlling N_2 selectivity.

Modifications of the electronic state and the surface structure of the active sites have been shown to improve the catalytic performance and influence the specific catalytic reactions. In Chapters 3 and 4, the successful modification of Pt is reported. This metal forms active centers in the SCR reaction and was found to maintain its metallic state under excess oxygen condition as the result of interactions with Mo and Na additives. The resulting $PtMoNa/SiO_2$ catalyst improved the reaction selectivity for NO as presented in Fig. 1, so that NO reduction was significantly improved under lean conditions, in contrast to the decreased performance seen with conventional Pt catalyst.

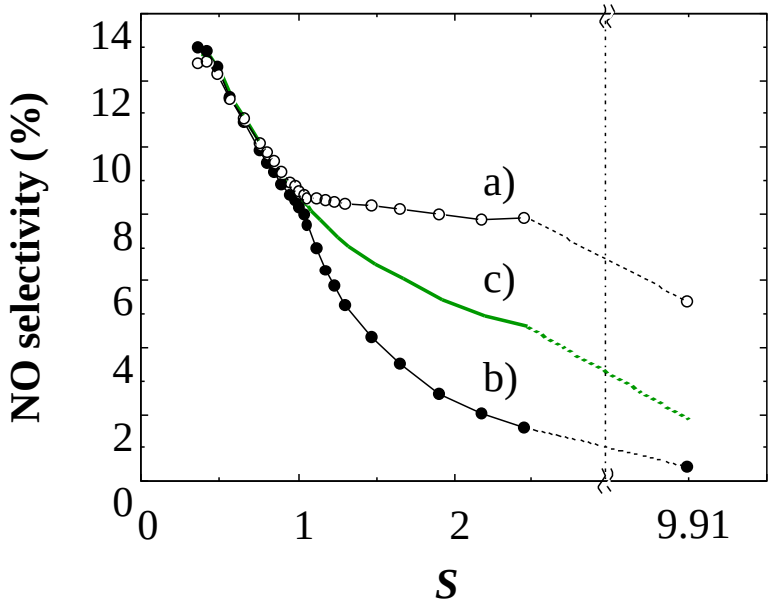

Fig. 1. NO selectivity for NO reduction as a function of redox ratio in simulated exhaust for S-scan at 600 ˚C. The following catalysts are indicated: (a) $PtMoNa/SiO_2$ and (b) Pt/SiO_2. (c) indicates NO fraction of inlet the NO + O_2 gases. S = ([NO] + 2 [O_2]) / ([H_2] + [CO] + 9 [C_3H_6]).

The modification of the catalyst by Mo and Na also expanded the active temperature region of SCR activity and enabled the use not only of HC gases but also CO and H_2 as reducing agents for the SCR reaction under lean conditions. The promotion effect of the addition of Mo and Na was clarified by the characterization using such as XPS and CO_{ads}-IR.

In Chapters 5 and 6, the modification of Ba as an active site for NO_X storage in an NSR catalyst through the surface formation of a fine composite oxide with TiO_2 was found to improve sulfur tolerance, which is a very important characteristic for an NSR catalyst. A highly dispersed Ba-Ti composite oxide was prepared using a stable Ba-Ti complex precursor in order to realize the nm-scale distribution of Ba and Ti. This improvement was derived from the analysis on the adsorption and desorption properties of sulfur on NSR catalysts, which revealed that the principal factor contributing to the high performance of the catalyst in terms of its sulfur desorption rate is concerned with an ability to inhibit repetitive adsorption during rich treatment for sulfur desorption, and the usage of TiO_2 is effective for the inhibition of the repetitive adsorption.

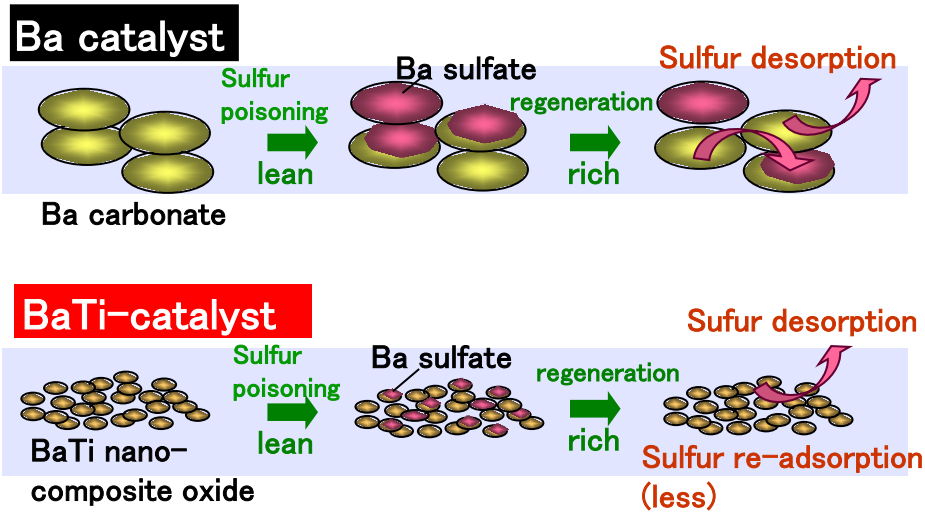

Fig. 2. The promoting effect of the BaTi composite oxide for NSR catalyst on the sulfur desorption.

The modification of Ba by TiO_2 contributed to the improvement of the sulfur regeneration abilities of the NSR catalyst by inhibiting repetitive adsorption during rich treatment for sulfur desorption, as indicated in Fig. 2. Therefore, the NSR catalyst using the Ba-Ti composite oxide enhanced sulfur desorption efficiency and led to high-performance NO_X conversion as a NO_X storage and reduction activity catalyst after desulfation treatment.

In Chapter 7, modification with TiO_2 was also found to be effective in catalysts using Ag as an active site for NO_X trapping at low temperatures. Dispersed octahedral-type TiO_2 on an alumina surface was found to stabilize Ag particles, resulting in high levels of dispersion. The dispersion of Ag on the TiO_2 modified Al_2O_3 produced a material able to adsorb NO_X at low temperatures (150 °C) even in the presence of other gases, as shown in Fig. 3.

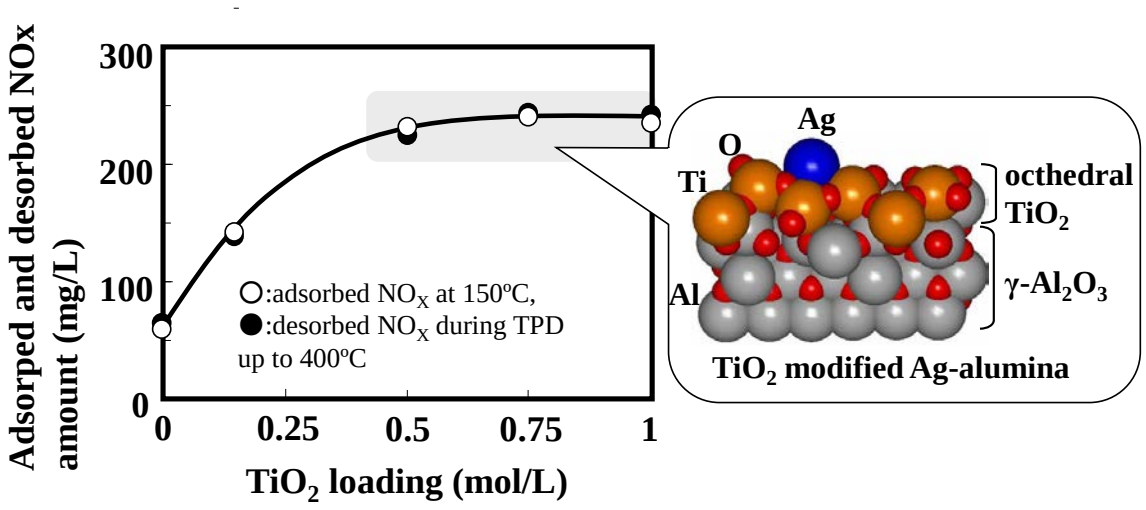

Fig. 3. Effects of TiO_2 addition on NO_X trapping performance at 150 ºC (following 750 ºC aging) of TiO_2 modified Ag/Al_2O_3.

In this NO_X trapping catalyst, Ag combined with TiO_2 works to create both oxidation sites for NO and adsorption sites for NO_X. These characteristics were thus

identified as important factors in the improvement of low temperature NO_X adsorption. The reaction mechanism of low temperature NO_X adsorption on the TiO_2 modified Ag/Al_2O_3 was proposed based on the characterization using such as XPS, XRD, TEM, NEXAFS, UV-vis and FT-IR as well as DFT calculations.

As noted earlier, this paper focused on NO_X purification catalysts operating under excess oxygen conditions, and investigated reaction and deterioration mechanisms during SCR and NSR processes. This work resulted in improvement of the catalytic materials, especially in the performance of active species such as the Pt in SCR catalysts, Ba in NSR catalysts and Ag in NO_X trapping catalysts. The results indicate that modification of the active sites affects both the catalyst's local structure and electronic structure (such as the coordination structure and the oxidation state) and can produce significant improvements in NO_X removal under excess oxygen conditions. However, some problems remain to be solved with regard to the performance of NO_X catalysts. Goal for future work include further expansion of their active temperature region, acceleration of reaction rates, improvements in thermal durability and poisoning resistance, reductions in fuel consumption and hence cost, reduced usage of precious metals and improved reducing agent dosing systems. Future environmental improvement on a worldwide scale will hinge on the progress which is made in these areas, and further development of NO_X removal systems is certainly anticipated, based on advances in both materials science and engine system controls.

List of Publications

Publications Related to Work Described in This Thesis

Part 1 Improvement of NO_X selective reduction catalyst

Chapter 2

1. T. Tanaka, T. Okuhara, M. Misono, *Applied Catalysis B: Environmental* 4 (1994) L1-L9.

"Intermediacy of organic nitro and nitrite surface species in selective reduction of nitrogen monoxide by propene in the presence of excess oxygen over silica-supported platinum."

Chapter 3

2. T. Tanaka, K. Yokota, H. Doi, M. Sugiura, *Chemistry Letters* 5 (1997) 409-410.

"Selective Catalytic Reduction of NO over PtMo Catalysts with Alkaline or Alkaline Earth Metal under Lean Static Conditions."

Chapter 4

3. T. Tanaka, K. Yokota, N. Isomura, H. Doi, M. Sugiura, *Applied Catalysis B: Environmental* 16 (1998) 199-208.

"Effect of the addition of Mo and Na to Pt catalysts on the selective reduction of NO."

Part 2 Improvement of NO_X storage and reduction catalyst

Chapter 5

4. T. Tanaka, I. Tajima, Y. Kato, Y. Nishihara, H. Shinjoh, *Applied Catalysis B: Environmental* 102 (2011) 620-626.

"Improvement in sulfur desorption of NO_X storage and reduction catalysts using a Ba-Ti composite oxide."

Chapter 6

5. T. Tanaka, K. Amano, K. Dohmae, N. Takahashi, H. Shinjoh, *Applied Catalysis A General* 455 (2013) 16-24.

"Studies on the regeneration of sulfur-poisoned NO_X storage and reduction catalysts, including a Ba composite oxide."

Part 3 New method to improve low temperature NO_X removal using NO_X trapping catalyst

Chapter 7

6. T. Tanaka, C. Ando, T. Hamaguchi, Y. Ikuta, *Applied Catalysis A General* 464-465 (2013) 296-304.

"Improved low temperature removal of NO_X from lean-burn exhaust via adsorption on TiO_2-modified Ag-alumina."

Publications Not Included in This Thesis

[Original Papers]

1. K. Yokota, M. Fukui T. Tanaka, *Applied Surface Science* 121-122, 2 (1997) 273-277.
"Catalytic removal of nitric oxide with hydrogen and carbon monoxide in the presence of excess oxygen."

2. T. Tanaka, N. Takahashi, H. Sobukawa, M. Sugiura, *2000 Int. Chem. Congr. Pacific Basin Soc.* INOR-0536, Honolulu, HI (Spons. by Am. Chem. Soc., et al.)
"Effect of Al_2O_3, TiO_2, and SiO_2 Support on NO_X Storage-reduction Catalyst."

3. T. Tanaka, K. Dohmae, N. Takahashi, S. Matsunaga, H. Sobukawa, H. Shinjoh, *5th Int. Symp. on Acid-Base Catal.* P1-22, Puerto Vallarta, Mexico
"The Influence of Thermal Aging Conditions on NO_X Storage and Reduction over KPt/ZrO_2 Catalyst."

4. Y. Yazawa, M. Watanabe, M. Takeuchi, H. Imagawa, T. Tanaka, *SAE 2007 World Congress & Exhibition*, Detroit, MI 2007-01-1056.
"Improvement of NO_X Storage-Reduction Catalyst."

5. Y. Tsukamoto, H. Nishioka, D.i Imai, Y.i Sobue, N. Takagi, T. Tanaka, T. Hamaguchi, *SAE 2012 World Congress & Exhibition*, Detroit, MI 2012-01-0370.
"Development of New Concept Catalyst for Low CO_2 Emission Diesel Engine Using NO_X Adsorption at Low Temperatures."

6. T. Tanaka, T. Hamaguchi, C. Ando, Y. Tsukamoto, N. Takagi, Y. Sobue, *7th edition of the International Conference on Environmental Catalysis (ICEC)* S06-T1-O-04, Lyon, France, September 2-6, 2012.
"Low temperature NO_X purification using NO_X adsorption on TiO_2 modified Ag-alumina."

[Review]

1. T. Tanaka, K. Yokota, N. Isomura, H. Doi, M. Sugiura, *Toyota Central R&D Review of Toyota CRDL* 33 (1998) 41-51.
"Selective Reduction of NO over Pt-Mo Catalysts under Lean Static Conditions."

Acknowledgements

The present study was conducted in a catalyst laboratory at Toyota Central Research & Development Laboratories Inc. (TCRDL) from 1992 to 2011 and in a Laboratory at the University of Tokyo from 1992 to 1993.

The author offers his sincerest gratitude to his supervisor Professor Tsunehiro Tanaka at Kyoto University, Dr. Naoki Takahashi and Dr. Hirofumi Shinjoh at TCRDL for their valuable advice and suggestions, and for the opportunity to undertake the research. The author also would like to express the deepest appreciation to Professor Takeshi Abe and Professor Ryu Abe at Kyoto University for their helpful discussions and comments regarding this thesis. The author would like to special thanks to Professor Tanaka for his helpful guidance to complete this thesis.

The author wishes to express his sincere thanks to Professor Makoto Misono at the University of Tokyo, Professor Toshio Okuhara at the University of Tokyo and Professor Yasushi Nishihara at Okayama University for their important support throughout this work and providing him the opportunity to undertake the research.

The author would like to express his gratitude to Professor Satohiro Yoshida, Professor Takuzo Funabiki and Professor Hiroyoshi Kanai for providing the required basic knowledge and skills about catalyst research during his undergraduate graduate research at Kyoto University.

The author would like to express his appreciation to Dr. Masaharu Sugiura, Dr. Haruo Doi, Mr. Koji Yokota and Mr. Shinichi Matsunaga at TCRDL for their helpful guidance for this study.

Acknowledgements

The author is very much grateful to all co-workers those who gave him the possibility to complete this thesis, Mrs. Chika Andoh, Dr. Haruo Imagawa, Mr. Tsuyoshi Hamaguchi, Dr. Yasuhiro Ikuta, Dr. Kazuhiko Dohmae, Dr. Noritake Isomura, Mr. Ichiro Tajima, Mr. Yuichi Katoh, Mrs. Kumi Amano and Mrs Naoko Takahashi.

Finally, the author thanks his family, Atsuko, Shuntaro and Haruhi for their continuous supports and providing him a willingness.

Toshiyuki Tanaka

Aichi,

May 2013